

Engineered Nano-Architectures as Advanced Anode Materials for Next Generation Lithium Ion Batteries

by

Fathy Mohamed Hassan

A thesis
presented to the University of Waterloo
in fulfillment of the
thesis requirement for the degree of
Doctor of Philosophy
in
Chemical Engineering (Nanotechnology)

Waterloo, Ontario, Canada, 2014

©Fathy Mohamed Hassan 2014

AUTHOR'S DECLARATION

I hereby declare that I am the sole author of this thesis. This is a true copy of the thesis, including any required final revisions, as accepted by my examiners.

I understand that my thesis may be made electronically available to the public.

Abstract

Li-ion batteries have a predominant market share as mobile energy storage devices, especially in consumer electronics. New concepts for electrode material designs are, however, necessary to boost their energy and power densities, and most importantly, the long term cycle stability. This will allow for these devices to gain widespread acceptance in electric vehicles, an area with immense market potential and environmental benefits. From a practical perspective, new electrode materials must be developed by simplistic, environmentally friendly and low cost processes.

As a new class of electrode materials, mesoporous Sn/SnO₂/Carbon composites with uniformly distributed Sn/SnO₂ embedded within the carbon pore walls have been rationally designed and synthesized. These nanocomposites have been characterized by x-ray diffraction (XRD), scanning electron microscopy (SEM), transmission electron microscopy (TEM), x-ray photoelectron spectroscopy (XPS), and tested as negative electrodes in a cell using lithium foil as the counter electrode. The inclusion of metallic Sn in SnO₂/CMK3 resulted in a unique, ordered structure and provided a synergistic effect which resulted in an impressive initial reversible capacity of 799 mAh g⁻¹. In addition, at a high current of 800 mA g⁻¹, the heterogeneous structure was able to provide a stable capacity of 350 mAh g⁻¹ and a retention capacity of ~ 670 mAh g⁻¹ after 60 cycles.

While Sn/SnO₂ composites have been deemed very promising, Si materials boast improved energy storage capacities, inspiring us to investigate these materials as new anode structure. A novel one-pot synthesis for the sub-eutectic growth of (111) oriented Si nanowires on an *in-situ* formed nickel nanoparticle catalyst prepared from an inexpensive nickel nitrate precursor is developed. Anchoring the nickel nanoparticles to a simultaneously reduced graphene oxide support created synergy between the individual components of the c-SiNW-G composite, which greatly improved the reversible charge

capacity and its retention at high current density when applied as an anode for a lithium-ion battery. The c-SiNW-G electrodes in a Li-ion battery achieved excellent high-rate performance, producing a stable reversible capacity of 550 mAh g⁻¹ after 100 cycles at 6.8 A g⁻¹ (78% of that at 0.1 A g⁻¹). Thus, this process creates an important building block for a new wave of low cost silicon nanowire materials and a promising avenue for high rate Li-ion batteries.

While excellent rate capability was obtained by using SiNW/graphene based material, simplifying the process may drive Si based materials to commercialization. A novel, economical flash heat treatment to fabricate silicon based electrodes is introduced to boost the performance and cycle capability of Li-ion batteries. The treatment results in a high mass fraction of Si, improved interfacial contact, synergistic SiO₂/C coating and a conductive cellular network for improved electronic conductivity, as well as flexibility for stress compensation. The developed electrodes achieve first cycle efficiency of ~84% and a maximum charge capacity of 3525 mA h g⁻¹, which is almost 84% of silicon's theoretical maximum. Furthermore, a stable reversible charge capacity of 1150 mA h g⁻¹ at 1.2 A g⁻¹ can be achieved over 500 cycles. Thus, the flash heat treatment method introduces a promising avenue for the production of industrially viable, next-generation Li-ion batteries.

Even though we obtained a dramatic improvement to a treated electrode based on commercial silicon, we still need to boost the cycle stability and high areal capacity achieved by higher electrode loading. Thus, we report a scalable approach that relies on covalent binding commercially available Si nanoparticles (SiNP) to sulfur-doped graphene (SG) followed by shielding them with cyclized polyacrylonitrile. The covalent synergy led to improved material property that can deliver stable reversible capacity of 1033 mAh g⁻¹ for more than 2000 cycles at a rate of 1 A g⁻¹. The areal capacity was 3.5 mAh cm⁻² at 0.1 A g⁻¹, approaching the commercial demand. The spatial arrangement of Si after cycling reveals that it was confined in nanowires morphology. This reveals that the solid

electrolyte interphase remains stable leading to superior cyclability. Our DFT calculations revealed covalent hybrid interaction between Si, S, and C leading to stable material configuration. Furthermore, the structure synergy facilitated lithium diffusion, which strongly supports our results. This simple, low cost, feasible, and safe approach provide new avenues for engineering electrode structure for enhanced performance.

Acknowledgements

I would like to first sincerely thank my advisor Prof. Zhongwei Chen, who shows incredible passion, and energetic attitude in support of my research. I would also like to thank my PhD thesis examination committee members, including Prof. Aiping Yu, Prof. Michael Fowler, Prof. Bo Cui and Prof. Yang Tse Cheng, for their time and effort, and valuable discussions.

Special thanks to all of our group members, current and past, for their support and assistance. I will never forget their kindness and enthusiasm for their research.

I would like to express my great thanks to the research staff at General Motors Global Research and Development Center. Special cordial thanks are for Dr. Xingcheng Xiao for his time, effort and valuable discussions

I would like to acknowledge the financial support the Natural Sciences and Engineering Research Council of Canada (NSERC) for providing an *Alexander Graham Bell Doctoral Scholarship* for 3 years. Also I would like to acknowledge the support from University of Waterloo for providing, (1) *President Scholarships* for 3 years, (2) Three semesters of *Research Studentships*, and (3) *PhD thesis completion award*.

Table of Contents

AUTHOR'S DECLARATION	ii
Abstract	iii
Acknowledgements	vi
Table of Contents	vii
List of Figures	ix
List of Tables.....	xiv
Chapter 1 Introduction.....	1
1.1 Challenges and Motivation.....	1
1.2 Objective of this work	3
1.3 Thesis outline	4
Chapter 2 Background and literature review	6
2.1 Principles of Li-ion Batteries.....	6
2.2 Cathode materials	8
2.2.1 Layered structure	9
2.2.2 Spinel Structure	10
2.2.3 Olivine structure	11
2.3 Anode Materials	12
2.3.1 Graphite anodes.....	13
2.3.2 Lithium-metal alloys	14
2.4 Electrolytes for lithium ion batteries	16
2.5 Binders for lithium ion batteries.....	17
Chapter 3 Synthesis of Sn/SnO ₂ into Mesoporous Carbon	19
3.1 Introduction	19
3.2 Experimental	21
3.2.1 Synthesis of CMK-3	21
3.2.2 Synthesis of Sn-based materials/CMK-3.....	22
3.2.3 Characterization.....	22
3.3 Results and Discussions	23
Chapter 4 Growth of SiNW on graphene	39
4.1 Introduction	39
4.2 Experimental Methods.....	41

4.2.1 Synthesis of SiNW-G.....	41
4.2.2 Electrode fabrication.....	42
4.2.3 Electrochemical performance.....	42
4.2.4 Characterization.....	43
4.3 Results and Discussions.....	43
Chapter 5 Engineered Si electrode nano-architecture.....	57
5.1 Introduction.....	57
5.2 Experimental Methods.....	60
5.3 Results and Discussions.....	61
5.3.1 FHT treatment and electrode structure.....	61
5.3.2 Electrochemical Performance.....	69
Chapter 6 Covalent binding of Si to S-doped graphene.....	76
6.1 Introduction.....	76
6.2 Results and Discussions.....	78
6.2.1 Characterization of the electrode materials.....	78
6.2.2 Electrochemical performance.....	82
6.2.3 Quantum mechanics calculations.....	86
6.3 Materials and Methods.....	91
6.3.1 Preparation of S doped graphene (SG).....	91
6.3.2 Electrode fabrication and testing.....	91
6.3.3 Material Characterization.....	92
6.3.4 Computational Method.....	92
Chapter 7 Conclusions and suggestions for future work.....	94
7.1 Conclusions and Summary.....	94
7.2 Suggestions for Future Work.....	95
References.....	97
Appendix I Supporting Figures for Covalent Binding of Si to S-doped Graphene (Chapter 6).....	117
Appendix II Author's Contribution.....	128

List of Figures

Figure 1-1. Chart introducing different possibilities of anode material.	4
Figure 2-1. Comparison of gravimetric and volumetric energy densities of different battery technologies. ⁷	7
Figure 2-2. Schematic illustrations for the lithium-ion battery.	8
Figure 2-3. Layered structure, LiMO_2 , e.g. LiCoO_2	9
Figure 2-4. A representative structure of spinel, LiMn_2O_4 . ²¹	10
Figure 2-5. Olivine structure of LiFePO_4	11
Figure 2-6: Graphite crystal structure showing the stacking of graphene sheets and the unit cell. ²⁸ ...	13
Figure 2-7. Comparing the gravimetric and volumetric capacities of different anode materials ²⁹	15
Figure 2-8. Illustrating the lithium ion capacity and electrochemical reduction potentials with respect to lithium metal for conventional anodes and cathodes. ³³	16
Figure 3-1. Schematic view of the synthesis of Sn-based/CMK-3.....	21
Figure 3-2. TGA curve of $\text{SnO}_2/\text{CMK-3}$ as prepared.....	24
Figure 3-3. (a) Nitrogen adsorption-desorption isotherms, (b) pore size distribution curve of the CMK-3, $\text{SnO}_2/\text{CMK-3}$ composite and SnO_2 (only for the isotherm).....	25
Figure 3-4. TEM images of the (a) pure CMK-3 and (b) SnO_2 incorporated CMK-3, inset: low angle X-ray diffraction (XRD) patterns.	26
Figure 3-5. (a) High resolution TEM image (inset : SAED patterns), (b) EDS spectrum and (c) dark field TEM image of the $\text{Sn}/\text{SnO}_2/\text{CMK-3}$ composites and the corresponding C, O, and Sn EDX elemental mapping.	28
Figure 3-6. (a) and (b) TEM images of different area of $\text{Sn}/\text{CMK-3}$ and (c) dark field TEM image and the corresponding C, O and Sn EDX elemental mapping.	29
Figure 3-7. SEM images of (a) CMK-3 and (b) $\text{SnO}_2/\text{CMK-3}$ composite.....	30

Figure 3-8. SEM images of (a) low resolution and (b) high resolution of SnO ₂ extracted for SnO ₂ /CMK-3.	30
Figure 3-9. X-ray diffraction patterns of SnO ₂ , SnO ₂ /CMK-3, SnO ₂ /Sn/CMK-3, and Sn/CMK-3 composites.	32
Figure 3-10. (a) low resolution XPS spectrum of SnO ₂ /Sn/CMK-3; high resolution XPS of (b) Sn3d, (c) O1s and (d) C1s in SnO ₂ /Sn/CMK-3.	33
Figure 3-11. Galvanostatic (a) discharge and charge curves of SnO ₂ /Sn/CMK-3 composite, (b) charge capacity of SnO ₂ , SnO ₂ /CMK-3, Sn/SnO ₂ /CMK-3 and Sn/CMK-3 composites, and the Columbic efficiency of Sn/SnO ₂ /CMK3, at current rate of 100 mA g ⁻¹ with respect to the cycle number.	34
Figure 3-12. (a) Capacity of SnO ₂ /Sn/CMK3 at various current rates from 100 to 800 mA g ⁻¹ with respect to the cycle number, (b) galvanostatic discharge and charge curves of pure CMK3 and the Coulombic efficiency at current rate of 100 mA g ⁻¹	38
Figure 4-1. SEM images of a) Ni nanoparticles formed on graphene after thermal shock reduction of the nickel nitrate and GO mixture and b) the resulting SiNWs grown on the intermediate in (a). c) TEM image of the c-SiNW-G composite, d) increased magnification TEM image representing the SiNWs within the c-SiNW-G composite, e) HRTEM and a corresponding FFT diffraction pattern shown in the inset for the SiNW, and f) the TEM image for SiNWs grown without graphene support.	45
Figure 4-2. a) HAADF-STEM (High-Angle Annular Dark-Field) of c-SiNW-G, b) EDX mapping of Si for the area marked in (a), c) EDX mapping of carbon, d) overlapping projection for the Si, C and Ni spectrums measured in c-SiNW-G, e) HAADF-STEM of SiNWs grown without graphene, and f) the EDX mapping for Si in (e).	46
Figure 4-3. a) XRD diffraction patterns for the as-synthesized c-SiNW-G (top) and the reference XRD spectrum measured for SiNP (bottom). b) Raman spectroscopy for c-SiNW-G. c) TGA analysis for c-SiNW-G.	48
Figure 4-4. a) Voltage profile for a coin cell containing c-SiNW-G cycled at 0.1 A g ⁻¹ , b) comparison of the cycle capability of SiNW-G with and without carbon coating using PAN, and c-SiNW-G using NaCMC, to that of pure graphene at 0.1 A g ⁻¹ , c) is the rate capability of SiNW-G compared to the non-supported SiNWs, and graphene, d) is a comparison of the voltage profile of SiNW-G at various	

currents, and e) is the cycle capability of SiNW-G at 6.8 A/g. (N.B. All capacities are based on the mass of silicon and graphene).	51
Figure 4-5. Cycle performance of c-SiNW-G in comparison with graphene, the inset is the corresponding voltage profile.....	52
Figure 4-6. a) Cyclic voltammogram for a coin cell fabricated using c-SiNW-G, b) EIS for coin cells fabricated using c-SiNW-G, SiNWs, and graphene.	54
Figure 4-7. a) TEM image for SiNW-G electrode material after 100 cycles. b) HAADF-STEM, c) HRTEM, and d-f) EDX mapping for the elements silicon, carbon and oxygen, respectively, in SiNW-G after cycling.....	56
Figure 5-1. a) Schematic of the flash heat treatment process (FHT) showing optical micrographs for the electrode surface before and after FHT and the Raman spectrum for the electrode surface both, b) before FHT and c) after FHT. The insets in (b) and (c) correspond to Raman mapping of the FWHM of the Si peak.	63
Figure 5-2. TGA for PVDF under nitrogen atmosphere.	64
Figure 5-3. Optical micrograph showing the electrode after flash heat treatment (FHT), the electrode material sticks tightly to the copper surface such that bending does not cause exfoliation. This reveals sufficient mechanical stability to sustain handling during cell fabrication.	64
Figure 5-4. (a) XRD pattern for the electrode surface after FHT and (b) shows the reference peaks of silicon (JCPDS 5-0565), copper (JCPDS 4-0836), and copper silicide (JCPDS 23-0223).	66
Figure 5-5. (a-b), Schematic of the electrode surface before and after FHT. (c-d), SEM micrographs for the electrode surface before and after FHT treatment, the insets of both figures show the EDS elemental analysis indicating carbonization by disappearance of fluoride peak, (e) is a SEM cross section of the electrode in (d).....	67
Figure 5-6. a) Low magnification TEM image of the electrode surface after FHT. b) Higher magnification TEM image zooming to a small area of (a), c) HRTEM image across the edge of one Si particle, d) Selected electron diffraction (SAED) taken from a large area of the electrode surface, e) a HAADF-STEM image of a few silicon particles on the electrode surface with carbon coating and f) Electron energy loss spectroscopy (EELS) profile analysis across the particle labeled in (e), the inset in (f) is a schematic depicting the core silicon and the shells of SiO ₂ and carbon layer.	68

Figure 5-7. (a) HAADF-STEM across a Si-NP from the FHT-treated electrode and its associated EDS elemental line scan across the particle as marked in (a). 69

Figure 5-8. (a) Galvanostatic voltage profile at 0.1 A/g with cut off voltage of 1.5 to 0.005 V for a coin cell fabricated using an electrode subjected to FHT , (b) the corresponding cycle capability at 0.1 A/g. (the first cycle efficiency is ~84%). 71

Figure 5-9. (a) Galvanostatic voltage profile showing cycle 1-3 at 0.12 A g⁻¹ and cycles 30, 100 and 500 at 1.2 A g⁻¹, (b) Cycle capability for the cell shown in (a), (c) Cyclic voltamogram for a coin cell measured at scan rate of 0.05 mV s⁻¹ between 1.0 and 0.05 V (vs Li⁺/Li), (d) Galvanostatic voltage profile at different rates, (e) Cycle performance showing the rate capability, and (f) EIS for the coin cell after discharge of the cycles 15, 30 and 100. 72

Figure 5-10. (a) Galvanostatic voltage profile at 0.1 A/g with cut off voltage of 1.5 to 0.005 V for a coin cell fabricated using electrode with 6:2:2 ratio of SiNP: Carbon : PVDF without subjecting the electrode to FHT, (b) the corresponding cycle capability of the non-treated electrode cycled at 0.1 A/g. (the first cycle efficiency is ~70%). 72

Figure 5-11. a) High-Angle Annular Dark field Scanning Transmission Electron micrograph (HAADF-STEM) of the electrode surface after being cycled for 500 cycles of charge/discharge, b) TEM image showing a few Si particles included in their carbon cage and interconnecting even after 500 cycles, c and d) EDS elemental mapping of Si, and C for the area selected in image a. e) HAADF-STEM zoomed in to a silicon particle as labeled in (a). (f) TEM micrograph for part of the electrode surface after cycling..... 74

Figure 5-12. (a-b) TEM images for different areas for graphene nanosheets prepared by spreading a thin film of PVDF on copper foil followed by FHT treatment, (d) HRTEM for an edge of the graphene sheet. 75

Figure 6-1. Schematic of sluggish heat treatment. a) an optical image of the as-fabricated electrode made of SiNP, SG and PAN, b) the electrode after SHT, c) HAADF-STEM image and d) TEM image of the SG-Si electrode, e, f) HRTEM images zooming in on a SiNP in the SG-Si electrode, and (f, inset) FFT pattern of the SiNP. 79

Figure 6-2. Electrode material characterization for SG-Si. a), XPS survey spectra confirming the elements Si, S, C, N and O, b) High-resolution XPS spectra of S in pure SG, and in SG-Si, c) High resolution XPS of Si 2p in SG-Si, d) High-resolution XPS spectra of C in SG-Si, e) HAADF-STEM

image of SG-Si, and f) EELS mapping of the elements Si(yellow) and S (red), with each pixel in Figs d-f representing 3.4 x 3.4 nm, g) Raman spectra for PAN film on copper before and after SHT, h) Raman spectra for SG-Si-PAN electrode surface before and after SHT..... 81

Figure 6-3. Electrochemical performance of SG-Si. a) Voltage profile of SG-Si anode at 0.1 A g⁻¹, b) the corresponding cycle stability, c) cyclic voltammogram curves of the SG-Si coin cell, d) rate capability of SG-Si anode followed by cycle stability at 2Ag⁻¹, e) rate capability of G-Si anode followed by cycle stability, f) rate capability of Si-PAN anode followed by cycle stability..... 84

Figure 6-4. Characterization of SG-Si electrode material after cycling for 2400 cycles. a) HAADF-STEM image of the SG-Si electrode after cycling, c-e) the elements mapping by EELS for the area marked in image. N.B. Each pixel in Figs d-f represents 3.4 x 3.4 nm. 86

Figure 6-5. DFT quantum calculations for G-Si and SG-Si systems. a) Geometries and binding energy (*BE*) of the stable Si adsorption configurations on i): graphene, referred as G-Si; ii) and iii): on sulfur doped graphene, referred as S-G-Si(A) and S-G-Si(B), respectively, C atoms are colored grey, H atoms white, S atom yellow, Si atom brown. Some of the important atoms were labeled, and they correspond to the atoms in Table S1, and b) The DFT calculated band gap together with the highest occupied molecular orbital (HOMO) and lowest unoccupied molecular orbital (LUMO) for different graphene substrates. 90

Figure 6-6. Projected density of states (PDOS) for Si atom and the individual C atoms involved in (a) Si adsorption on graphene, G-Si, and (b-d) sulfur doped graphene, SG-Si(B). 90

List of Tables

Table 1: Lists of different commercial cathode materials with their properties. ^{26, 27}	12
Table 2: List of different anode materials for lithium ion batteries. ²⁷	15
Table 3. List of different solvents commonly used in the electrolyte of lithium ion batteries with their physical properties ^{34, 35}	18
Table 4. List of the equivalent circuit parameters of the modelled EIS data for the lithium ion cells.	54

Chapter 1 Introduction

1.1 Challenges and Motivation

With limited global supplies and concerns of climate change public attention has been drawn toward the development of eco-friendly technologies such as hybrid electric vehicles (HEVs) and electric vehicles (EVs), grid scale energy storage, power electronics, control systems as well as the high-end mobile devices. Currently, Li ion batteries (LIB) are the most commonly used technologies in these systems due to their attractive high gravimetric and volumetric energy densities compared to other energy storage technologies such as lead acid, Ni-Cd and Ni-MH batteries¹ Lithium ion batteries are becoming more common in portable electronic devices due to their high energy density, lack of memory effect, and high charge and discharge rate capabilities. However, with the ever increasing demands, the current technology cannot meet the stringent requirements for application in electric vehicles or hybrid electric vehicles that require higher power, in addition to high energy density. Intensive research efforts have been focused on developments that push conventional capabilities of LIB technology. These efforts include research to improve all aspects of LIBs, including developing novel active materials for the anode and cathode, separators, electrolytes and overall cell and stack designs. The active materials in the electrodes play an important role in determining the LIB energy density, power density and cycle stability. The current technology utilizes micro-sized particles based on carbon (graphite) as the anode materials in which lithium intercalates during battery charging. Because of the small capacity and the limitation of lithium diffusion, the current technology need to be upgraded to be able to provide higher energy and power densities.

Alternate anode material need to be developed in order for LIBs to meet the demands of next generation devices and applications. Anodes based on tin (Sn) or silicon (Si) provide higher energy density than

graphite. In terms of specific capacity, Si has the highest theoretical value of 4200 mAh g⁻¹. Sn is not far behind with 65-75% of the Si capacity. In addition, these elements are abundant, non-toxic, and inexpensive. However, due to the nature of the reactions during lithiation and delithiation, these materials have 3 major challenges:

- i) Large volume change during lithiation/delithiation results in material degradation and capacity loss.
- ii) Low current efficiency and unstable solid electrolyte interphase (SEI).
- iii) Loss of electrode integrity including electronic isolation between particles.

Several solutions to overcome these issues have been proposed. One common approach is to incorporate the active material into a matrix conductive material. This matrix plays a bifunctional role, serving both as a conducting skeleton, and to improve the mechanical integrity of the electrode by accommodating the volume changes occurring during battery cycling. Even though these electrodes have a lower initial capacity because of the additives, they show relatively stable cycling. Another approach focuses on minimizing stresses caused by volume changes by rationally controlling the morphology and nanostructures of the electrode materials. For example, Silicon nanoparticles were embedded in a carbon matrix through a multistep process creating void spaces that accommodate volume changes during lithiation/delithiation.² Mesoporous silicon sponges were used to minimize the pulverization during lithiation/delithiation. The silicon sponge delivered a capacity of 750 mAh g⁻¹ and 80% capacity retention.³ Self-healing chemistry by forming hydrogen bonds was used to stabilize silicon microparticles anodes, providing longer cycle life.⁴ Another method concerning the polymeric structure of the electrode was introduced by Cui et al.⁵ They used in-situ polymerization of conducting hydrogel to coat the silicon nanoparticles, providing porous space for volume expansion of Si particles.⁵ The sophisticated and tedious synthesis of nanostructured silicon however leads to excessive costs that

render silicon anodes more expensive than the current graphite ones. New concepts are required to develop these advanced non-graphite electrode structures that are inexpensive, and allowing researchers to capitalize on the immense theoretical energy storage density of the materials.

1.2 Objective of this work

In this thesis, a focus is placed on the development of a new generation anode materials for LIBs. The main objectives are:

- 1- Develop controlled nanostructure of Sn based materials;
- 2- Controlled synthesis of silicon nanowires grown directly on graphene;
- 3- Introducing a new method to treat the Si-based anodes leading to changes in the electrode nano-architectures and providing impressive performance; and,
- 4- Introducing sulfur-doped graphene as a support for Si in the electrode structure.

The next generation anode materials is shown schematically in **Figure 1-1**.

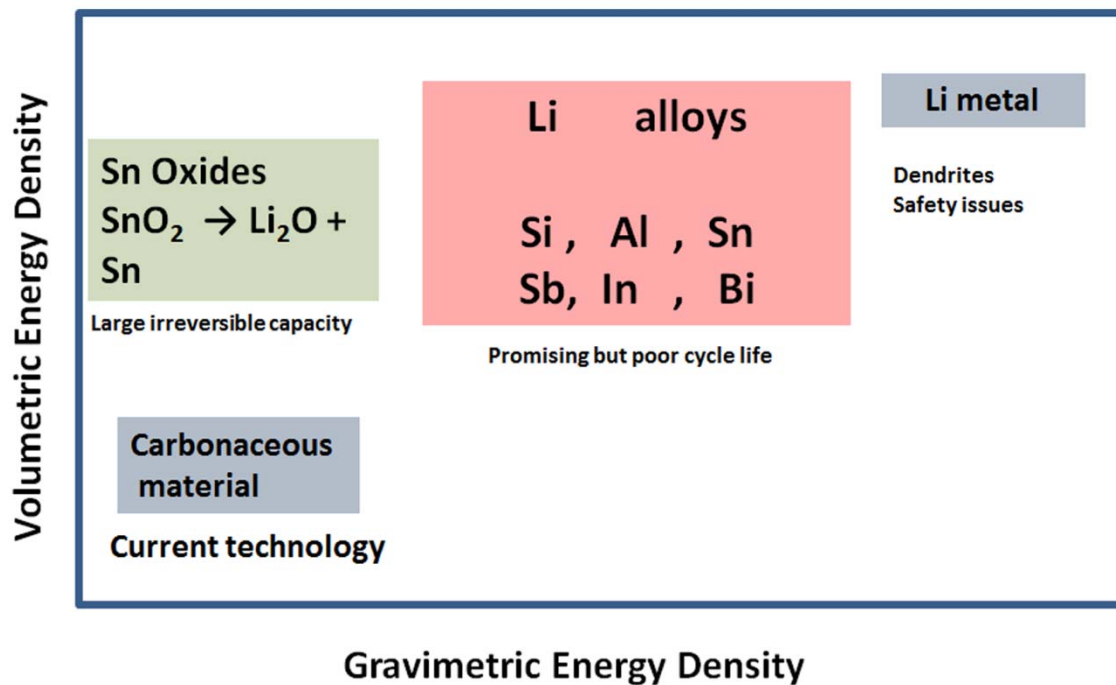


Figure 1-1. Chart introducing different possibilities of anode material.

1.3 Thesis outline

This thesis consists of several chapters. An introduction, which includes the motivation and objective of the work is provided in Chapter 1. In Chapter 2, the background and a literature review is included, in which the working principals of lithium ion batteries are introduced and discussed. In addition, a brief introduction to each component of the lithium-ion battery is shown. The results and discussions from the research activities are introduced in Chapters 3-6, broken down into sub-tasks for the overall project. The synthesis and electrochemical performance of Sn-based material was introduced in Chapter 3. A hybrid nanostructure of Sn/SnO₂ was incorporated into the nanochannels of ordered mesoporous carbon (CMK3). The results reveals better performance than the conventional graphite based lithium

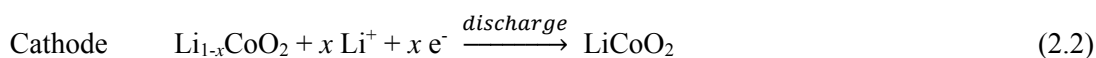
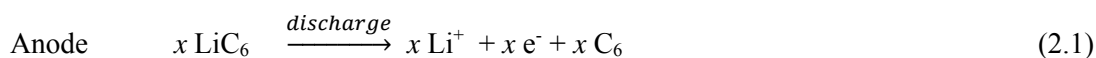
ion battery. In the subsequent Chapters (4-6) several successful approaches for using silicon based material are developed. In Chapter 4, a one-pot synthesis of Si nanowires on *in-situ* formed nickel nanoparticle on graphene are reported. The nanostructure created synergy between the individual components of the c-SiNW-G composite, which greatly improved the reversible charge capacity and its retention at high current density when applied as an anode for a lithium-ion battery. In Chapter 5, a novel, economical flash heat treatment of the fabricated silicon based electrodes (starting with commercially available silicon nanoparticles) is introduced. The treatment reveals a high mass fraction of Si (90%) binder free matrix, improved interfacial contact, synergistic SiO₂/C coating and a conductive cellular network for improved conductivity, as well as flexibility for stress compensation. The enhanced electrodes achieve first cycle efficiency of ~84% and a maximum charge capacity of 3525 mA h g⁻¹, almost 84% of silicon's theoretical maximum. In Chapter 6, a scalable approach that relies on covalent binding commercially available Si nanoparticles (SiNP) to sulfur-doped graphene (SG) followed by shielding them with cyclized polyacrylonitrile. The covalent synergy led to improved material property that can deliver stable reversible capacity of 1033 mAh g⁻¹ for more than 2000 cycles at a rate of 1 A g⁻¹. The areal capacity was 3.5 mAh cm⁻² at 0.1 A g⁻¹, approaching the commercial targets. Chapter 7 summarizes the conclusions of the results and introduces proposed future research directions.

Chapter 2 Background and literature review

2.1 Principles of Li-ion Batteries

Electrochemical energy storage systems are extremely important for efficient utilization of renewable energy, for the advancement of portable electronics, and for directing the future of electric vehicles. Batteries are on the forefront of the devices that can perform this task. They efficiently convert chemical energy into electric energy through coupled redox reactions. Various batteries have been developed (**Figure 2.1**), among which Li-ion batteries have the highest gravimetric and volumetric energy densities. This is due to the fact that lithium is the most electropositive metal with a standard potential of 3.04 V vs SHE. It is also the lightest as well (6.94 g/mole).⁶ The general composition of a battery (**see Figure 2.2**) is a cathode (+ve), an anode (-ve) which are separated using a separator, and an electrolyte. The traditional Li-ion battery is composed of graphite as the anode and a lithiated transition metal oxide as the cathode (source of lithium). They are separated using a porous polymer membrane e.g. polypropylene. The electrolyte is usually a lithium salt such as LiPF₆ dissolved in a mixture of organic solvents e.g. ethylene carbonate (EC), dimethyl carbonate (DMC) etc. The following is the chemistry of a typical lithium ion battery during discharge:

Lithium travels from the lithiated graphite (Li_xC₆) to intercalate to Li_{1-x}CoO₂ (lithium cobalt oxide, a typical cathode material):



This type of cell operates at 3.7 V with a capacity of 150 mAh g⁻¹.

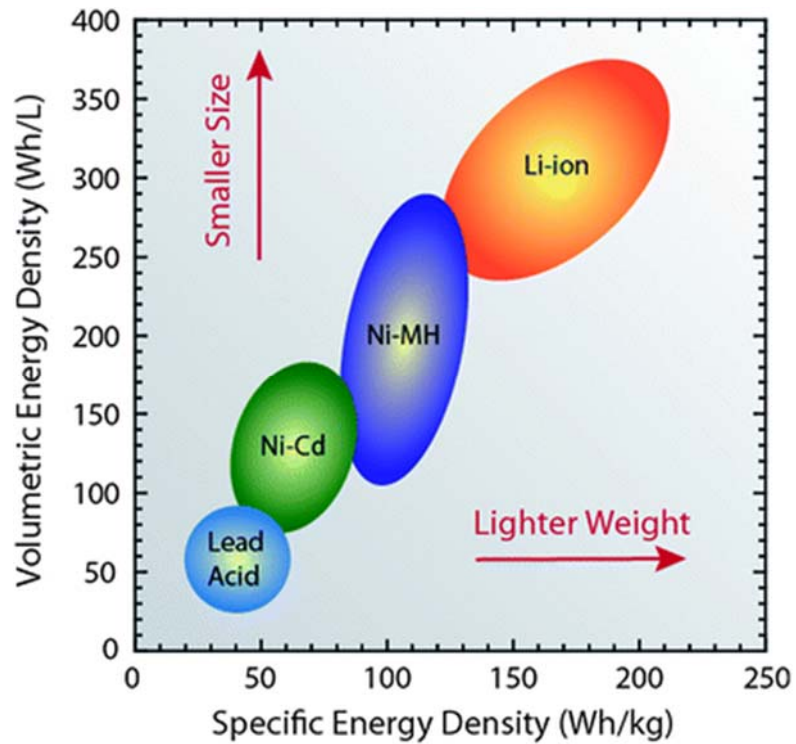


Figure 2-1. Comparison of gravimetric and volumetric energy densities of different battery technologies.⁷

In order to consider reliability of lithium ion batteries, the following conditions need to be met:⁸

1. The electrode materials have to maintain chemical and mechanical stability during cycling.
2. Low cost of the materials and reduced environmental impact. Cheaper elements like Fe, Ni, Mn are preferred than Co based material.
3. Safety: the design should avoid leaks or fires.
4. Long cycle life: the battery should provide enough deep discharge cycles that satisfy the consumer. This means that the electrode materials should be very stable providing reversible electrode reactions with minimal losses.
5. The battery components should be stable at the temperature range of operating conditions.
6. High energy and power density to satisfy the market need.

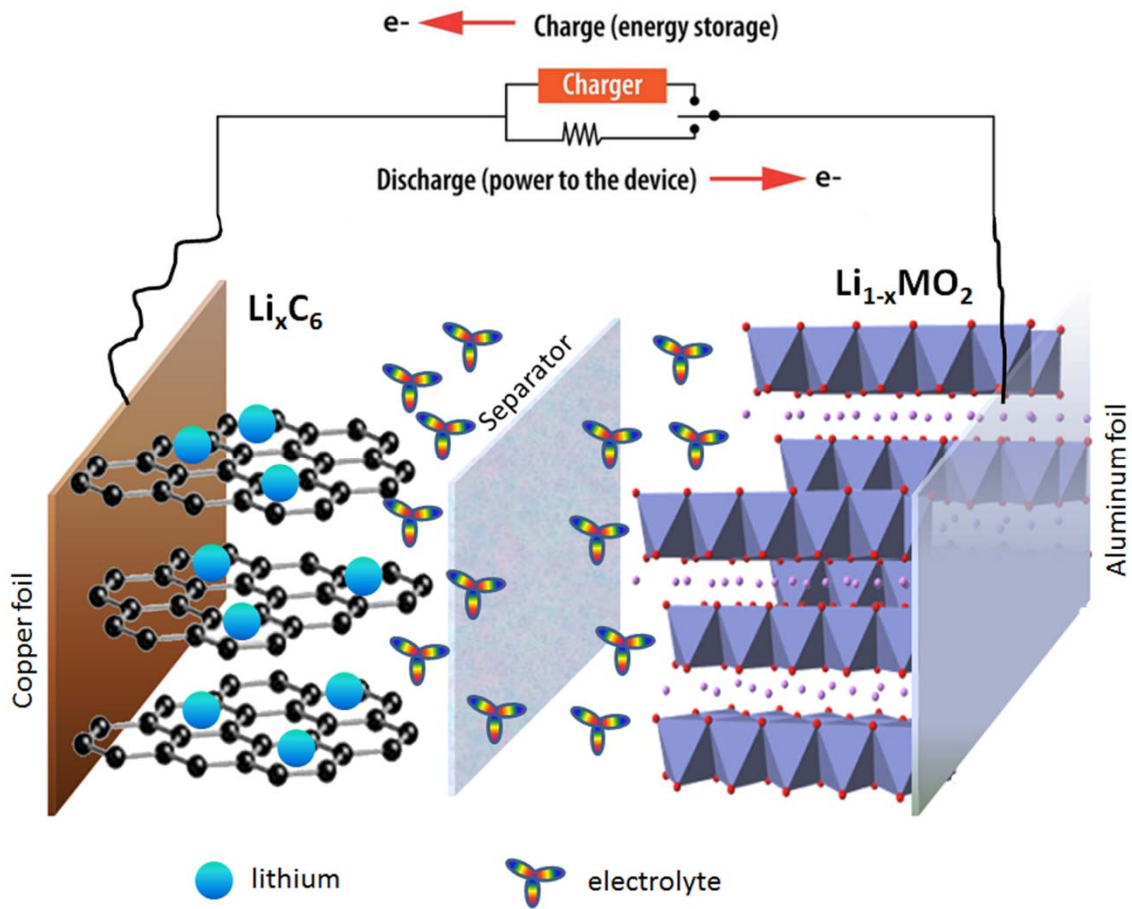


Figure 2-2. Schematic illustrations for the lithium-ion battery.

2.2 Cathode materials

First of all, any cathode material should have a higher potential with respect to lithium. Intercalation compounds that can accommodate lithium with high capacity are ideal candidates. These materials should also have some properties in common; e.g., high electronic conductivity, facilitated lithium

diffusion, and structure stability. Lithiated transition metal oxides are commonly used as cathode materials for lithium ion battery.^{7,9} They can be classified based on their structure as follows:

2.2.1 Layered structure

This class of the inorganic materials has the general formula as (LiMO_2) , where M is Co, Ni, Mn, etc.). They are cubic closed packed arrangement, in which lithium and cobalt ions occupy octahedral sites in alternating layer (**Figure 2.3**). If the lithium is completely removed, the oxygen layers rearrange themselves to give CoO_2 .¹⁰ Lithium cobalt oxide materials have a theoretical capacity of 272 mAh g^{-1} . However, the practical capacity is only 140 mAh g^{-1} if charged up to 4.2 V. The reason for that, if this material is over-charged, there are several phase transition and structure changes that may result in the collapse of the crystal structure of the material.¹⁰ This can infer that we can only extract 0.5 moles of lithium per mole of LiCoO_2 while maintaining the structure integrity of the material. The toxicity of cobalt and the high price in comparison to other transition metals, along with safety issue are making the continuing success of this material a challenge.

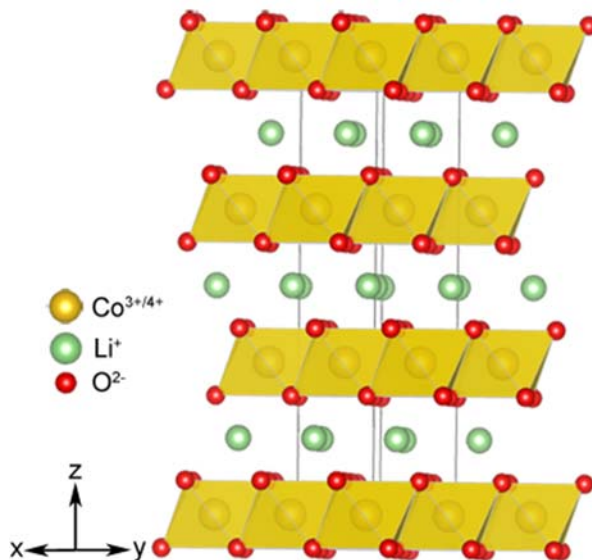


Figure 2-3. Layered structure, LiMO_2 , e.g. LiCoO_2 .

2.2.2 Spinel Structure

A typical spinel cathode material is LiMn_2O_4 . In this structure, the anion lattice is cubic closed packed oxide and the cations are distributed among the available octahedral and tetrahedral sites.¹¹⁻¹⁵ There are two steps during the discharge of LiMn_2O_4 . The first step is at ca. 4.0 V, whereas the second one follows at 3.0 V. It is recommended to avoid discharging up to 3.0 V to avoid distortion of the spinel caused by Jahn-Teller Effect. In this case the capacity would be limited to about 120 mAh g^{-1} , corresponding to a plateau at 4.0 V. The capacity fading for this material is attributed to several factors. Manganese ions may dissolve into the electrolyte and generate strain on the crystal during cycling.¹⁶ It is possible to improve cycle stability, and possibly the capacity, by doping this structure with other transition metals. The formula would be $\text{LiM}_x\text{Mn}_{2-x}\text{O}_4$, where M could be Ni, Fe, Ti, Cu, Zn, etc.¹⁸⁻²⁰

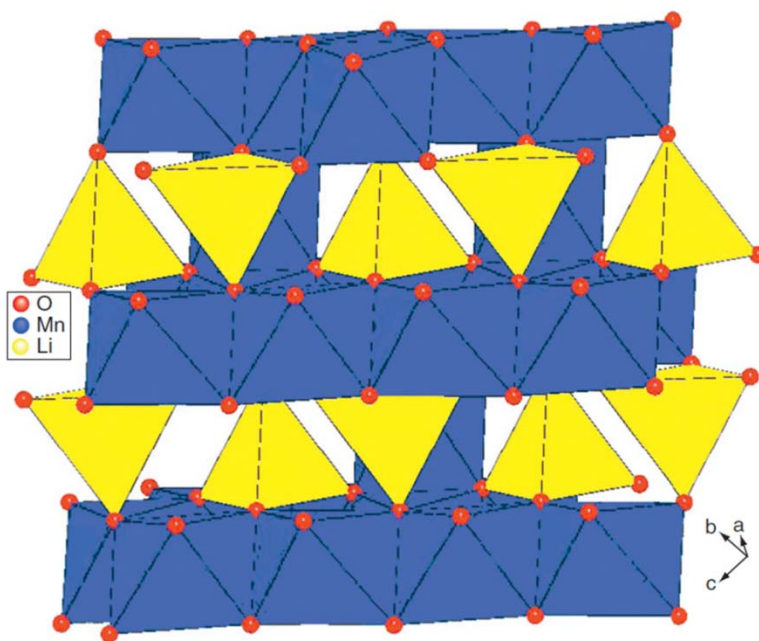


Figure 2-4. A representative structure of spinel, LiMn_2O_4 .²¹

2.2.3 Olivine structure

The most common cathode material having the olivine structure is LiFePO_4 (**Figure 2.4**).²² The structure is orthorhombic, where each Li and Fe is surrounded by six oxide ions in an octahedral structure and the phosphate group, PO_4 , has a tetrahedral structure. The LiFePO_4 discharge with a characteristic plateau at 3.4V leading to a capacity of 170 mAh g^{-1} , which is even better than LiCoO_2 . LiFePO_4 has excellent cycling performance, when considered along with its being abundant and environmentally benign, as a very promising cathode material. The drawback is the low electrical conductivity. To improve its electrochemical properties it is required to be carbon coated.²³ Conductivity also can be improved by doping with another element such as niobium.²⁴ Another trend in improving the material is achieved by controlling the particle size and lowering the defects, thereby facilitating lithium diffusion.²⁵

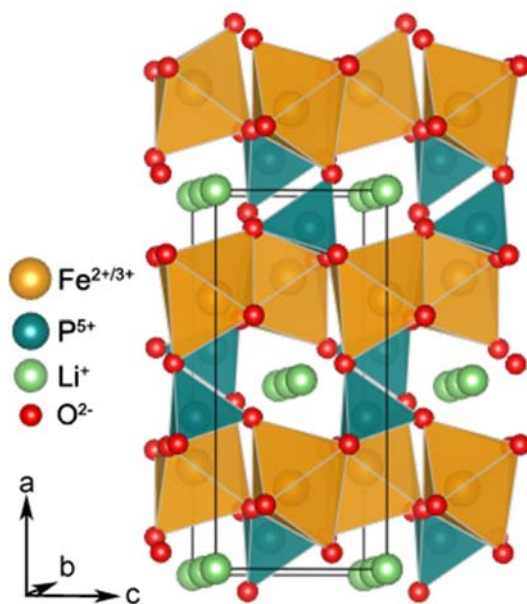


Figure 2-5. Olivine structure of LiFePO_4 .

Table 1. Lists of different commercial cathode materials with their properties.^{26, 27}

Material	structure	Shape of the discharge curve	Average potential vs. Li ⁺ /Li (V)	Practical capacity mAh g ⁻¹	Safety	Cost
LiCoO ₂	Layered	Flat	3.9	160	Fair	High
LiNi _{0.8} Co _{0.15} Al _{0.05} O ₂	Layered	Sloping	3.8	200	Fair	Fair
LiNi _{1/3} Mn _{1/3} Co _{1/3} O ₂ (NMC)	Layered	Sloping	3.8	200	Good	Low
LiMn ₂ O ₄ (LMO)	Spinel	Flat	4.1	110	Good	Low
LiFePO ₄ (LFP)	Olivine	Flat	3.45	160	Good	Low

2.3 Anode Materials

One of the major components for a lithium-ion battery is the anode. Metallic lithium was the first choice as an anode material for lithium ion batteries, especially during the 1970s and 1980s, because it has a low density and high capacity. Nevertheless, the lithium-based lithium ion batteries were not successful because of safety issues. Lithium forms dendrites during repeated cycles, eventually to the point that it penetrates the separator and short circuits the battery. Research has therefore been focused on finding alternative anode materials. The ideal anode materials ideally meets the following criteria:

1. High gravimetric and/or volumetric capacity.
2. High Coulombic efficiency, especially for the first cycle.
3. Abundant, safe, environmentally benign and cheap.
4. Stable for cycling
5. Compatible with the electrolyte.

2.3.1 Graphite anodes

In commercial lithium ion batteries, the active anode materials are comprised of graphite (**Figure 2-6**). It is a cheap material and can accept lithiation through intercalation reaction at low operation voltages ($\sim 0.1\text{V}$ vs Li/Li^+). It can be charged up to LiC_6 which is translated into a maximum theoretical capacity of 372 mAh g^{-1} .

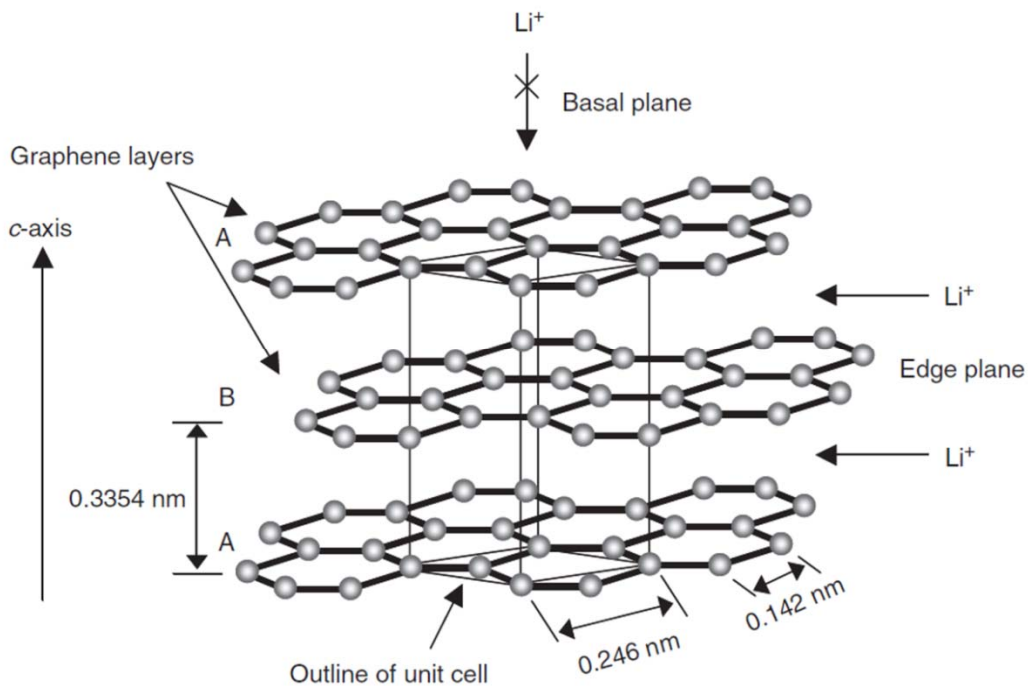


Figure 2-6: Graphite crystal structure showing the stacking of graphene sheets and the unit cell.²⁸

However, the existing anode materials cannot meet all of the requirements. This creates challenges for research and development to find a new anode material that can fit the requirements.

2.3.2 Lithium-metal alloys

It has been discovered that lithium can react with other elements forming a family of intermetallic compounds, **Figure 2-5**.²⁹⁻³² For example, lithium can be stored by reacting with silicon, forming $\text{Li}_{4.4}\text{Si}$ that corresponds to a gravimetric capacity of 4200 mAh g^{-1} (similar with Sn and Ge). The electrochemical reaction during alloying is simple. However, during the reaction, there is a dramatic volume change, whereby in the case of silicon, the volume change is up to 300%. These expansions and contractions during charging and discharging results in accumulated stresses and eventually fracturing of the electrode materials. The mechanical degradation leads to loss of electronic contact, and instability of the solid electrolyte interphase (SEI). This results in decreased Coulombic efficiencies and an eventual dramatic loss in capacity. **Table 2** list different anode materials with their capacities and the average potential at which they react with lithium. Comparing the gravimetric and volumetric capacities of different elements as in **Figure 2-7**, and also considering the abundance, cost, safety of the element, it can be concluded that Sn and Si are the choice as a promising anode material for lithium-ion batteries.

Figure 2-8 compares the different anode and cathode materials in terms of the capacity and the voltage. As can be seen the anode materials have lower potential while the cathode materials have higher potential. The difference between them, in a cell, constitutes the cell voltage. The great advantage for lithium-ion batteries system is the high cell voltage, which can reach up to 4.5 V. This is the highest among all type of batteries.

Table 2: List of different anode materials for lithium ion batteries.²⁷

	Anode material	Theoretical specific capacity mAh g ⁻¹	Potential, V vs Li/Li ⁺
	Li metal	3862	0
Carbon	Graphite	372	0.1
Alloy	Al (LiAl)	993	0.35
	Sn(Li ₂₁ Sn ₅)	948	0.42-0.66
	Sb (Li ₃ Sb)	660	0.9
	Si(Li _{4.4} Si)	4200	0.5
	Cu ₆ Sn ₅ (Li ₂₂ Sn ₅ + 6Cu)	605	0.1
Spinel	Li ₄ Ti ₅ O ₁₂ (Li ₇ Ti ₅ O ₁₂)	175	1.56

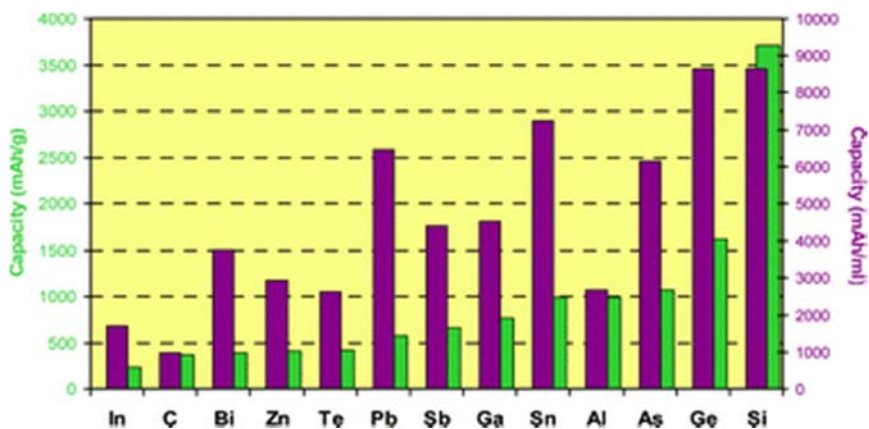


Figure 2-7. Comparing the gravimetric and volumetric capacities of different anode materials²⁹.

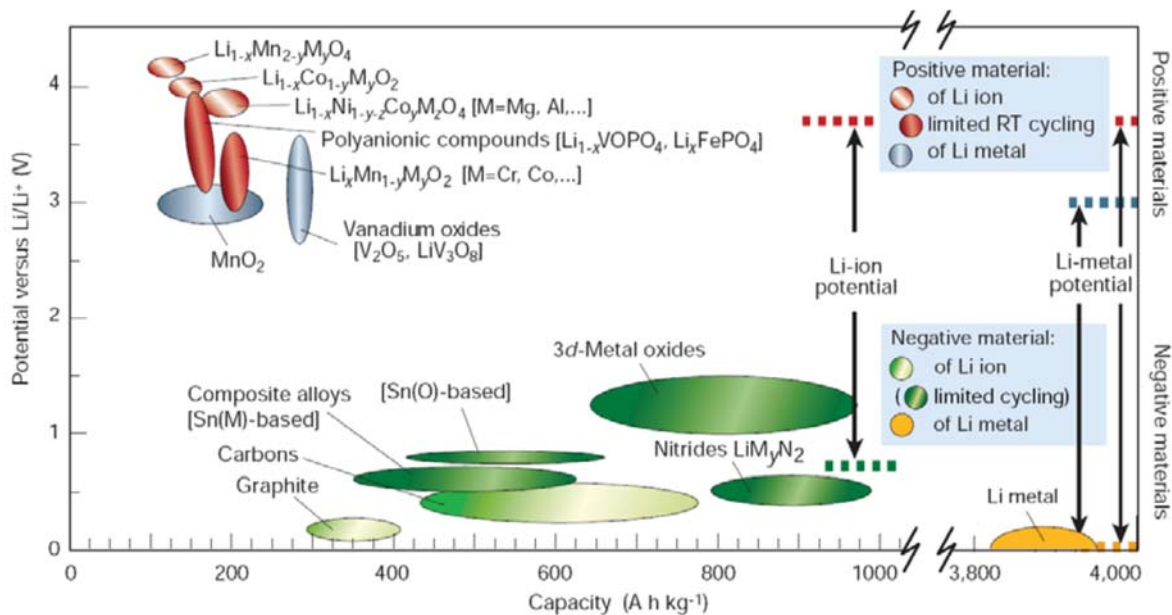


Figure 2-8. Illustrating the lithium ion capacity and electrochemical reduction potentials with respect to lithium metal for conventional anodes and cathodes.³³

2.4 Electrolytes for lithium ion batteries

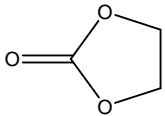
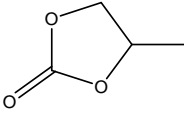
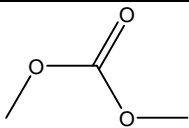
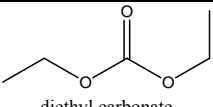
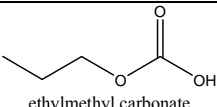
The electrolyte shuttles lithium ions between the anode and the cathode. Thus, the electrolyte should be good ionic conductor and stable at high voltages (up to 4.5 V). Nonaqueous electrolytes are commonly used for this purpose. The electrolyte is basically composed of a salt and a solvent. The salt is an inorganic materials that have lithium, e.g. lithium hexafluoro phosphate (LiPF_6), lithium tetra fluoroborate (LiBF_4), and lithium perchlorate (LiClO_4). The solvent is a mixture of organic compounds, most commonly linear or cyclic carbonates. The carbonate solvents currently in use are; ethylene carbonate (EC), dimethyl carbonate (DMC), ethyl methyl carbonate (EMC), and diethyl carbonate (DEC). The organic solvents may suffer partial decomposition on the surface of the electrode. This is commonly called solid electrolyte interphase. The products are favorably electrically insulating but highly lithium ion conducting. Thus preventing subsequent decomposition process, and passivate the

electrode surface without sacrificing the performance. A list of some solvents that are commonly used for lithium ion batteries, with their physical properties, is provided in **Table 3**. One important property for the electrolyte is potential window, which can allow for utilization of high voltage cathode materials.³⁴

2.5 Binders for lithium ion batteries

Binders are polymeric materials that bind the electrode component together to maintain good electrode integrity. Battery efficiency depends on electrode engineering, so the role of the binder is just as important as the active material itself. All components harmoniously generate a synergy that controls the battery performance. The binder has to withstand the spatial changes inside the electrode during charge/discharge cycles. One common binder is poly(vinylidene) fluoride (PVDF). It can be used for both anode and cathode materials. PVDF has good electrochemical stability and strong adhesion holding the electrode material tight to the current collectors. PVDF requires N-Methyl-2-pyrrolidone (NMP) as a solvent, and it can persist at high cell voltages. Moreover, PVDF has a good resistance versus changes in temperatures, excellent mechanical strength, and good processing performance.

Table 3. List of different solvents commonly used in the electrolyte of lithium ion batteries with their physical properties^{34, 35}

Structure	Melting point (°C)	Boiling point (°C)	Viscosity (cP at 25 °C)	Dielectric constant (at 25 °C)
 ethylene carbonate	36.4	248	1.9 (40 °C)	89.78
 propylene carbonate	-48.8	242	2.53	64.92
 dimethyl carbonate	4.6	91	0.59 (20 °C)	3.11
 diethyl carbonate	-74.3	126	0.75	2.81
 ethylmethyl carbonate	-53	110	0.65	2.96

Chapter 3 Synthesis of Sn/SnO₂ into Mesoporous Carbon

The following section is based on previously published work³⁶ by Hassan, F. M. et al, *Electrochimica Acta*, 87, (2013) 844-852.

“Sn/SnO₂ Embedded in Mesoporous Carbon Nanocomposites as Negative Electrode for Lithium Ion Batteries”

Reproduced with permission.

3.1 Introduction

Fossil fuel supply limitations and concerns of climate change due to steadily increasing greenhouse gas emissions has drawn public attention toward the development of eco-friendly technologies such as hybrid electric vehicles (HEVs) and electric vehicles (EVs). Among various energy storage systems, lithium (Li) ion batteries currently present the best performances to meet the applications' demands because of its high gravimetric and volumetric energy density, long cycle life and low self-discharge rate. However, it remains a significant technical challenge to increase the capacity, rate capabilities and durability of Li ion batteries in order to meet the steadily increasing energy density demands for large-size applications.

Metallic tin (Sn) is one of the best candidates as a negative electrode material for next generation Li ion batteries because it's capacity is more than two times higher than that of conventional graphite electrodes. According to the mechanism of the reaction between Sn and Li, up to 4.4 Li atoms can

associate with each Sn atom, leading to a theoretical capacity of 994 mAhg^{-1} ³⁷⁻³⁹. Nevertheless, large volume changes during alloying/de-alloying of Sn with Li causes mechanical degradation in the form of pulverization and cleavage of the electrode materials, inevitably resulting in poor cycle stability. An alternative candidate to Sn-based materials is SnO_2 , which has a two-step energy storage mechanism occurring during battery operation. First, the irreversible formation of Li_2O will occur, followed by the reversible formation of a Li_xSn alloy. The first reaction provides a buffer matrix of the materials to improve the cycle stability and contributes to the irreversible capacity. Conversely, the second reaction contributes to the reversible capacity which is maintained due to mitigated mechanical degradation owing to the buffer matrix remaining from the first reaction. Because of the initial formation of Li_2O , SnO_2 gives a lower theoretical capacity (782 mAhg^{-1}) than that of metallic Sn (994 mAhg^{-1}).³⁹

Although SnO_2 provides improved long-term cycle stability compared to metallic Sn, after only a few cycles of alloying/de-alloying reactions with Li, aggregation of Sn may occur which can break down the Li_2O buffer matrix and eventually show the same mechanical degradation problems as that of metallic Sn. Various research efforts to improve the capabilities of SnO_2 materials have been reported, including the incorporation of SnO_2 into carbon-based material composites such as carbon nanotubes (CNTs)⁴⁰⁻⁴⁴, graphene⁴⁵⁻⁴⁹ and porous carbon⁵⁰, which have been demonstrated to provide remarkable improvements. The carbon-based materials provide high surface areas and a rigid structure to maintain mechanical integrity of the SnO_2 based composites, and conductive pathways to facilitate electron transport during the alloying/de-alloying cycles.

Ordered mesoporous carbon⁵¹ provides host sites for nano-sized metal oxide to be formed, and its 3-dimensional conductive structure enhances conductivity of the metal oxide based electrode. In addition, it can be suggested that confining the metal oxide particles in the rigid skeleton can suppress large volume change during alloying/de-alloying cycles. Herein, we report the synthesis of Sn-based mesoporous carbon composites as a negative electrode material for Li ion batteries. We initially

prepared SnO₂ embedded in CMK-3, then after controlled heat treatment we were able to partially reduce SnO₂ to form Sn/SnO₂/CMK3 or completely reduce it to Sn/CMK-3. Sequence of the synthesis is schematically illustrated in **Figure 3-1**. These materials were investigated as electrode material for Li ion battery. Based on the results from the study, Sn/SnO₂/CMK-3 composite introduced the best performances regarding capacity and cycle stability.

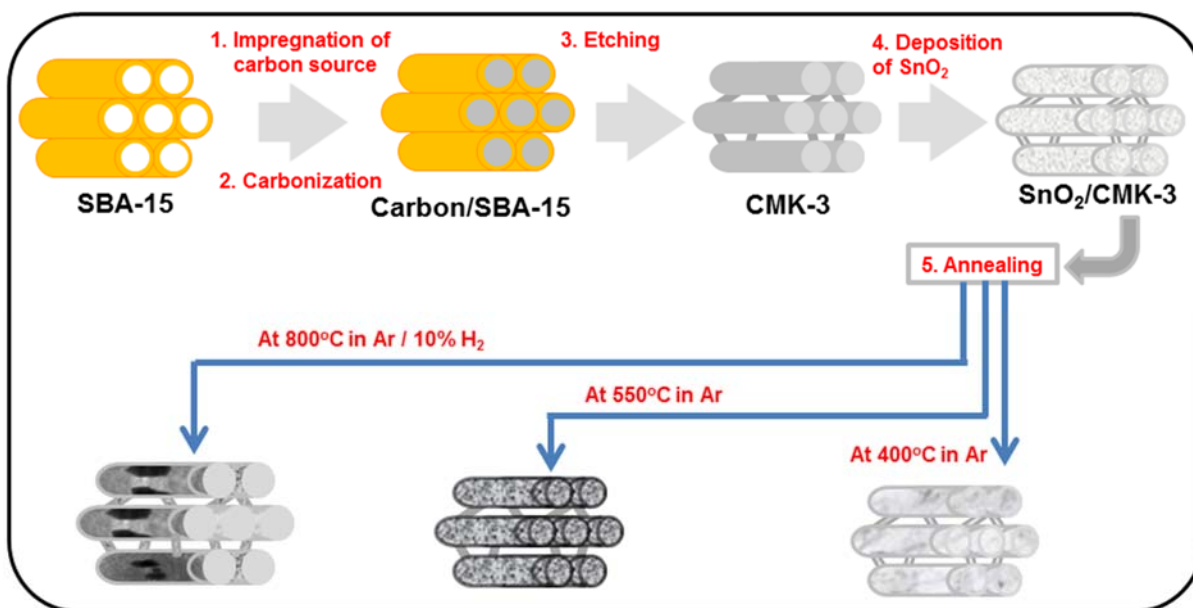


Figure 3-1. Schematic view of the synthesis of Sn-based/CMK-3

3.2 Experimental

3.2.1 Synthesis of CMK-3

First of all, mesoporous SBA-15 as a silica template was prepared using the triblock copolymer, EO₂₀PO₇₀EO₂₀ (Pluronic P123), as the surfactant and tetraethylorthosilicate (TEOS) as the silica source based on the procedure described by Zhao et al.⁵². Then 1 g of SBA-15 was mixed with a solution

containing 1.25 g of sucrose and 0.14 g of H₂SO₄ in 5 g of H₂O, following the method reported by Jun et al.⁵³. The mixture was put in a drying oven for 6 h at 373 K, and subsequently the oven temperature was increased to 433 K and maintained there for 6 h. After collecting the sample, the sample was treated again with 0.8 g of sucrose, 0.09 g of H₂SO₄ and 5 g of H₂O followed by another heat treatment at 373 and 433 K as previously stated. The sample was carbonized at 1173 K under a nitrogen gas. The product was washed with 5 wt% HF aqueous solutions at room temperature to remove the silica template. Lastly, CMK-3 was filtered, washed with distilled water and dried at 393 K.

3.2.2 Synthesis of Sn-based materials/CMK-3

Initially, 100 mg of CMK-3 were dispersed in 250 ml of 0.13 M HCl (prepared using deionized water and concentrated HCl). Then 800 mg of SnCl₂.2H₂O were dissolved in 150 ml DI H₂O and this solution was added to the dispersed CMK-3 solution drop wise while magnetic stirring. After that, the solution was kept stirring for 4 h at room temperature (298 K). Finally the composite SnO₂/CMK-3 was separated by filtration and subsequent washing with DI several times. The residue was dried in an oven at 373 K for 1 day. The composite powder was separated into 3 parts. The first and the second parts were subjected to annealing at 673 and 823 K for 5 h under flowing Ar atmosphere (100 sccm). The third part was annealed at 1073 K for 5 h in a mixture of Ar and 10% H₂ gas.

3.2.3 Characterization

XRD was conducted to confirm the CMK-3 structure and Sn-based materials' phases in the CMK-3. The structural properties and morphology of Sn-based/CMK-3 were characterized by TEM and SEM. N₂ adsorption–desorption isotherms were used to analyze pore sizes and surface areas by the Brunauer–Emmett–Teller (BET) method. Thermal gravimetric analysis (TGA) was carried out to investigate the

ratio of Sn-based materials and CMK-3. X-Ray photoelectron spectroscopy (XPS) was also conducted to support the composition of Sn-based/CMK-3 products. The electrochemical performances were conducted with coin type cells. For the working electrode, a slurry consisting of 70 % of active material, 10 % super-p as a conductive material and 20 % polyvinylidene fluoride (PVdF) as a binder was prepared in N-methyl-2-pyrrolidone (NMP) and was coated on Cu foil. The electrode was dried in the drying oven at 373 K for 1 hr, followed by being placed in the vacuum oven at 373 K for overnight. The coin cells were fabricated in an argon-filled glove box with the working electrode and the Li metal as the reference and counter electrode. A polypropylene separator was employed to separate the two electrodes and 1M LiPF₆ in 1:1 ethylene carbonate (EC) and dimethyl carbonate (DMC) (Novolyte, USA) was used as the electrolyte. Galvanostatic charge/discharge test was carried out at the voltage range of 0.01 to 3.00 V (except SnO₂ powder, 0.01 to 1.50 V) with current density of 100 mA g⁻¹ based on Sn-based materials/CMK-3 mass. For rate capability test the current densities were varied from 100 to 800 mA g⁻¹.

3.3 Results and Discussions

In this study, SnO₂/CMK-3 was first prepared as a reference of the study and then treated by alteration of annealing temperature and atmosphere to transform into metallic Sn. It was confirmed that the amount of SnO₂ in CMK-3 is 58.2 % by Thermogravimetric analysis (TGA) (**Figure 3-2**). **Figure 3-3** shows nitrogen adsorption-desorption isotherms and pore size distributions of pure CMK-3, SnO₂ / CMK-3 which was annealed at 673 K and SnO₂ which was obtained from SnO₂ / CMK-3 after burning CMK-3 away in air atmosphere at 773 K. Distinct step for pure CMK-3 Between 0.4 and 0.5 of relative pressure (P/P₀) was observed indicating typical mesoporous material characteristics. After incorporation of SnO₂ into CMK-3, the distinct step in the relative pressure curve disappeared because synthesized SnO₂ into CMK-3 blocks the pore of CMK-3 (**Figure 3-3a**). Another evidence is

introduced by pore size distribution curves. SnO₂/CMK-3 composite shows lower intensity and smaller pore size in the materials (**Figure 3-3b**). The Brunauer-Emmett-Teller (BET) specific surface areas of pure CMK-3, SnO₂/CMK-3 composite and SnO₂ from SnO₂/CMK-3 were calculated based on **Figure 3-3a**. The BET surface areas decreased from 1556 m²g⁻¹ for pure CMK-3 to 536 m²g⁻¹ for SnO₂/CMK-3 composite suggesting that SnO₂ is successfully formed into the pore of CMK-3 and reduced the surface area. On the other hand, the surface area of the SnO₂ nanoparticles is 136.6 m²g⁻¹, which is reasonable value for nano-sized SnO₂ particles.

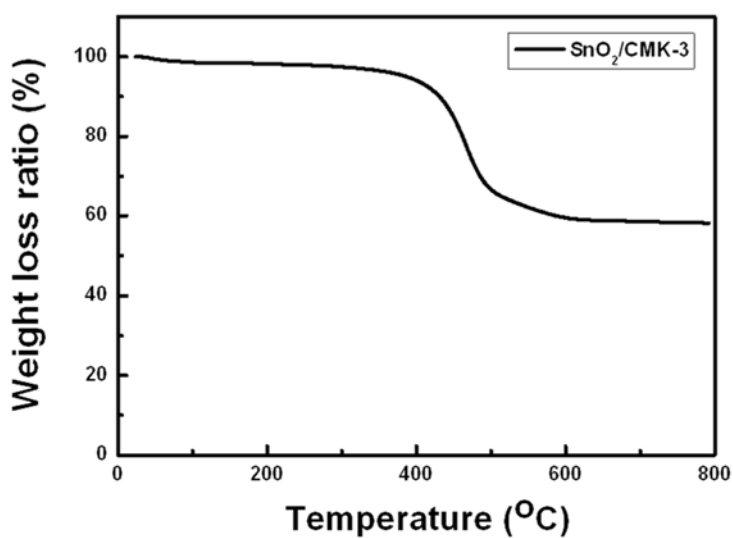


Figure 3-2. TGA curve of SnO₂/CMK-3 as prepared.

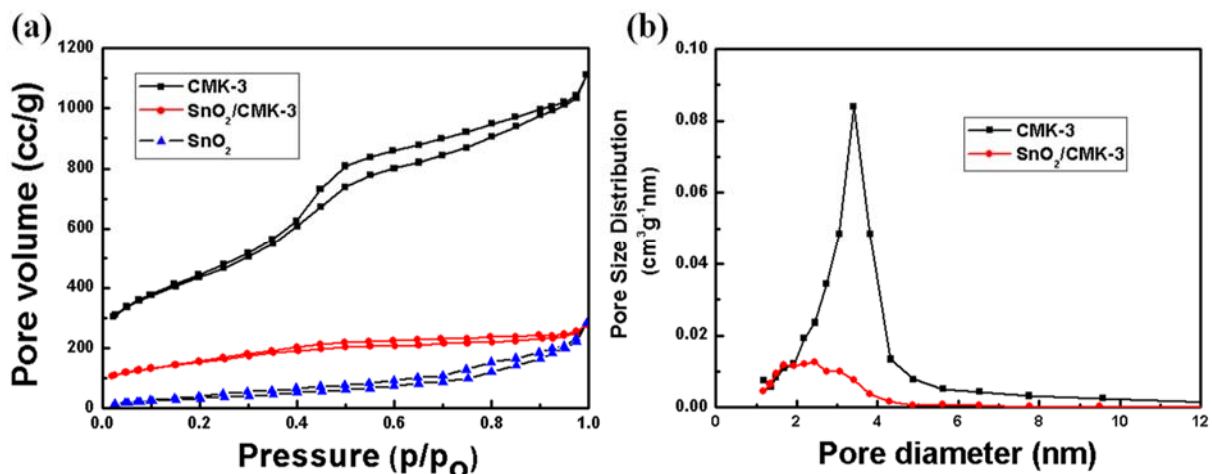


Figure 3-3. (a) Nitrogen adsorption-desorption isotherms, (b) pore size distribution curve of the CMK-3, SnO₂/CMK-3 composite and SnO₂ (only for the isotherm).

In addition, TEM images in **Figure 3-4** exhibit direct evidence of SnO₂ particles formed inside CMK-3. The SnO₂ particles can be found at the channels of CMK-3 in the SnO₂/CMK-3 composite (**Figure 3-4b**) while pure CMK-3 shows ordered spotless channels in **Figure 3-4a** even though the image is not clear because of the weak resolution between the CMK-3 skeletons. The ordered structure was confirmed by a low angle XRD pattern (inset in **Figure 3-4a**), introducing three peaks of (100), (110) and (200) which agree with two dimensional hexagonal structure (P6mm)⁵³. Furthermore, a low angle XRD pattern for SnO₂/CMK-3 (inset in **Figure 3-4b**) suggest that the ordered structure is maintained after incorporation of SnO₂ which is also supported by the TEM image of SnO₂/CMK-3 in **Figure 3-4b**. The particle size can be estimated to ~ 2.5 nm which is less than the channel size of CMK-3 without aggregation of the particles.

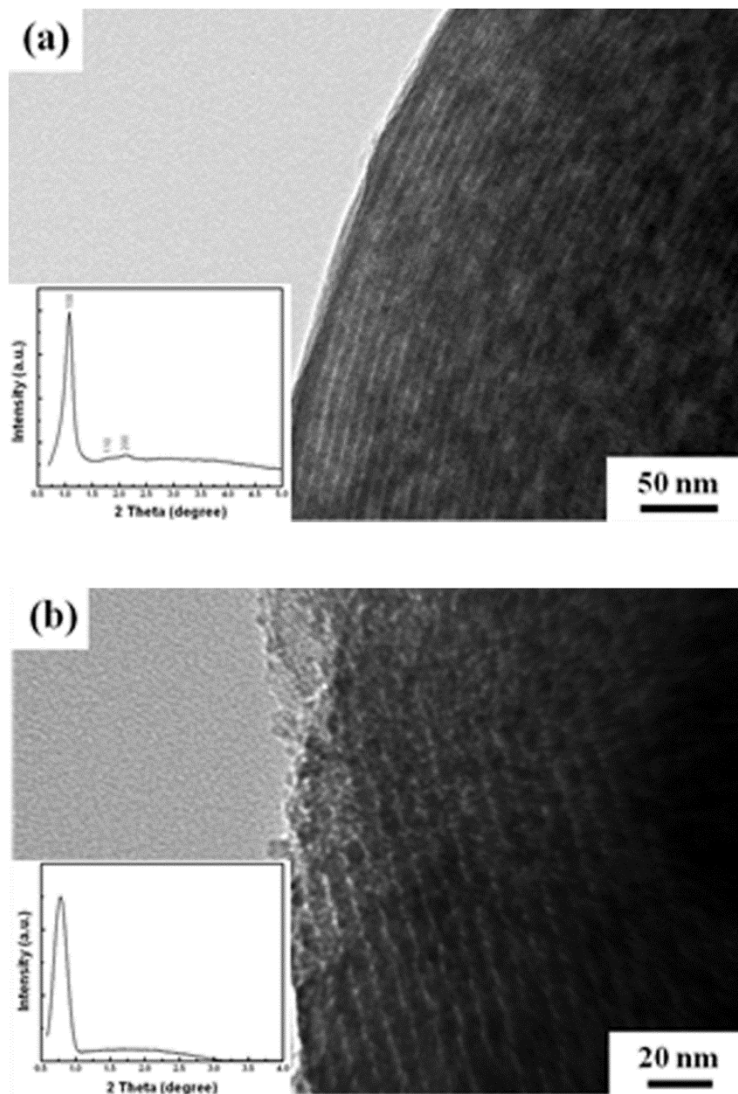


Figure 3-4. TEM images of the (a) pure CMK-3 and (b) SnO₂ incorporated CMK-3, inset: low angle X-ray diffraction (XRD) patterns.

Figure 3-5 introduces a HRTEM image for the Sn/SnO₂/CMK-3 composite material. The image (**Figure 3-5a**) reveals the detailed intrinsic nanostructure of these mixed Sn-based materials. The nanoparticles were evenly distributed inside the mesoporous carbon matrix. Several lattice spacing measurements correspond to SnO₂ nanoparticles, e.g., 0.33 nm for the 110 plane, 0.26 nm for (101),

and 0.24 nm for (200), were successfully elucidated by the selected area electron diffraction (SAED) pattern. It was difficult to detect any lattice spacing correspond to metallic Sn, even though it was confirmed by XRD (cf **Figure 3-9**). This suggests that metallic tin is formed by reduction of carbon in a small fraction in the deep pores of the CMK-3. These buried nanoparticles of Sn, which are over-laid by several carbon and SnO₂, were difficult to be detected by HRTEM. Furthermore, the elemental Energy-dispersive X-ray spectroscopy (EDX) mapping of the Sn/SnO₂/CMK-3 sample was displayed in **Figure 3-5c**. It shows that the Sn/SnO₂ nanoparticles were homogeneously distributed and clearly confirm that there is no agglomeration inside the material. The EDX elemental analysis (**Figure 3-5b**) showed that the molar ratio of Sn to O is slightly less than 1:2, which suggest that there is a small portion of metallic Sn is embedded in the material.

Figure 3-6 shows the TEM for SnO₂/CMK-3 after being subjected to annealing at 1073 K in a mixture of Ar and 10% H₂ gases. This environment was suitable to reduce all SnO₂ to metallic Sn. Because of the low melting point of tin and large surface energy, so the particles tend to diffuse on the surface of carbon forming larger particles, or tiny droplets, which eventually coalesce forming large islands of metallic Sn. The islands of metallic Sn are clearly shown by TEM images (**Figure 3-6a**), and TEM dark field, **Figure 3-6c**. Elemental mapping of the elements C, O and Sn, which was detected based on **Figure 3-6c** is also a strong evidence for Sn agglomeration. The process of agglomeration didn't lead to collapse of the mesoporous carbon skeleton (**Figure 3-6b**). However, it may have caused some local break for parts of the nano carbon rods.

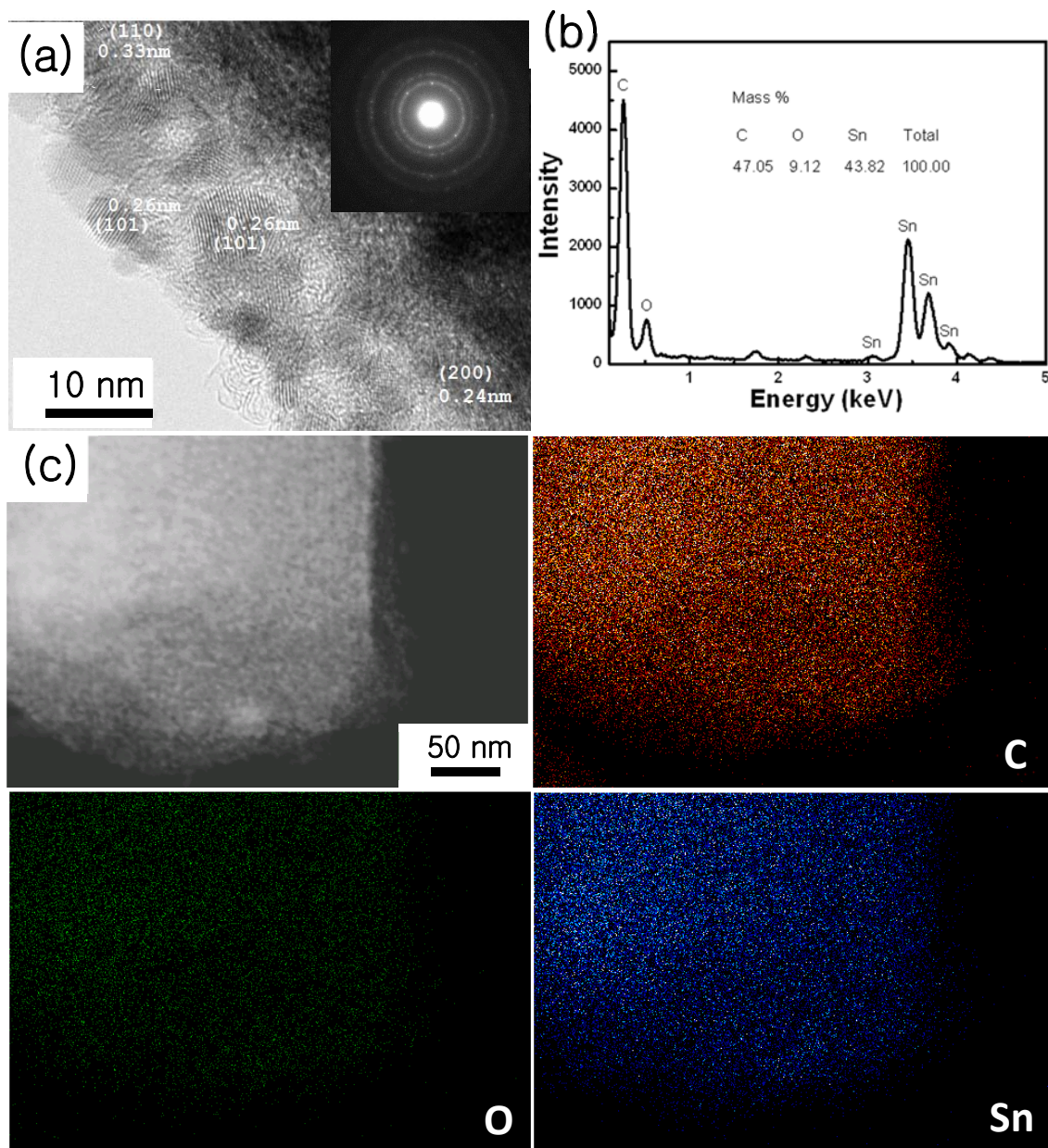


Figure 3-5. (a) High resolution TEM image (inset : SAED patterns), (b) EDS spectrum and (c) dark field TEM image of the Sn/SnO₂/CMK-3 composites and the corresponding C, O, and Sn EDX elemental mapping.

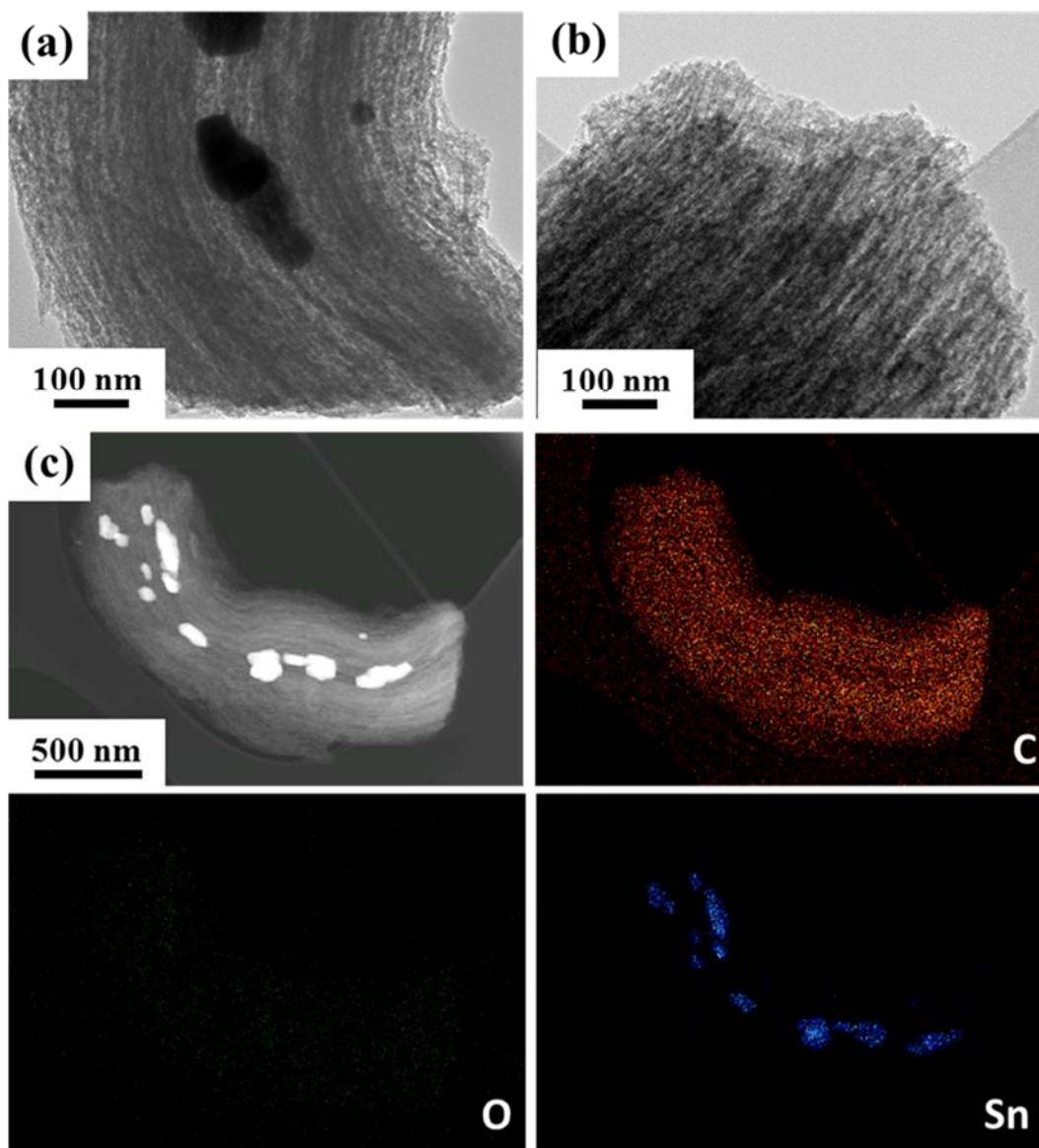


Figure 3-6. (a) and (b) TEM images of different area of Sn/CMK-3 and (c) dark field TEM image and the corresponding C, O and Sn EDX elemental mapping.

Figure 3-7 Compares the SEM images of pure CMK-3 (**Figure 3-7a**), and SnO₂/CMK-3 composite (**Figure 3-7b**). It can be noted that there is no distinct change between pure CMK-3 and SnO₂/CMK-3 composite. It is indicating that most SnO₂ is formed interior of CMK-3 and the SnO₂ do not destroy the

framework of the CMK-3. **Figure 3-8** introduces SEM images of the SnO₂ particles after burning CMK-3 from SnO₂/CMK-3 composite. The aggregated particles are found in **Figure 3-8a** because high surface energy of nano-sized SnO₂ cannot be kept without the CMK-3's frameworks. However, on the surface of the SnO₂ particles the trace of nano-sized SnO₂ particles can be found and that morphology is attributed to the high surface area (**Figure 3-8b**).

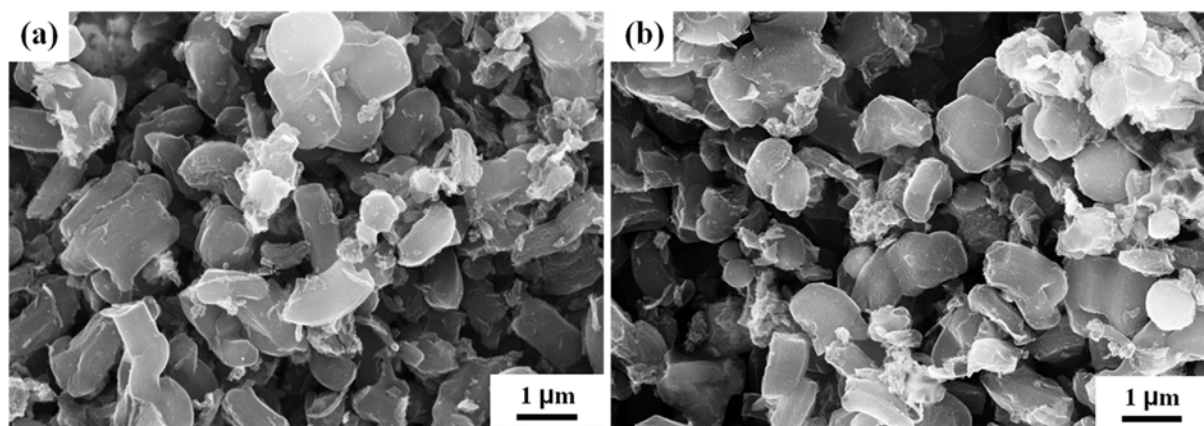


Figure 3-7. SEM images of (a) CMK-3 and (b) SnO₂/CMK-3 composite.

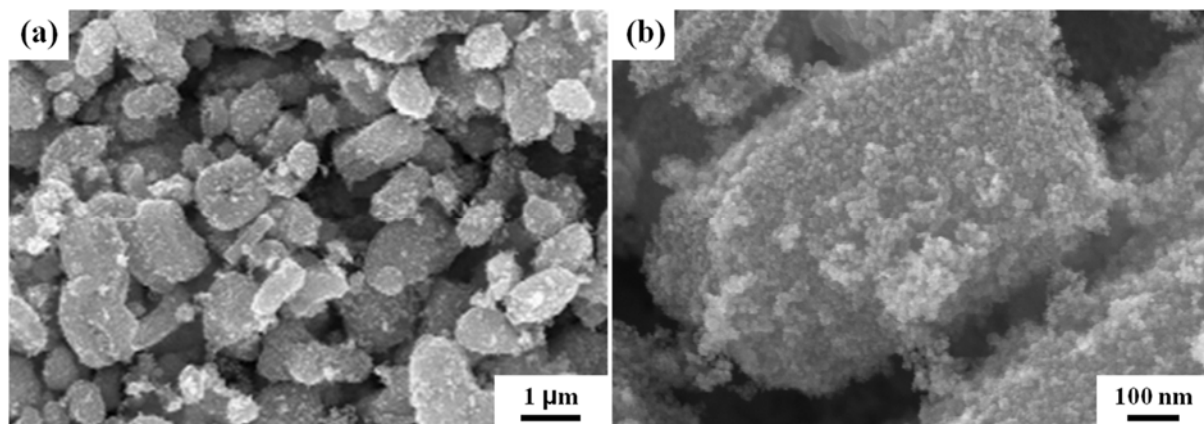


Figure 3-8. SEM images of (a) low resolution and (b) high resolution of SnO₂ extracted for SnO₂/CMK-3.

To confirm the phases of Sn-based materials, an XRD analysis was carried. **Figure 3-9** shows the XRD patterns for the materials with different annealing conditions. The XRD patterns of the SnO₂ / CMK-3 treated by 673 K in Ar atmosphere and pure SnO₂ obtained from the SnO₂ / CMK-3 correspond to the tetragonal SnO₂ with cassiterite structure (JCPDS No. 41-1445)⁵⁴. Based on the peak broadness, it is assumed that the SnO₂ particles are made up nanocrystalline size. The particle size can be estimated to ~2.5 nm by using the Scherrer equation⁵⁴, which is comparable with the channel size of CMK-3. With the increase in temperature up to 823 K in Ar, the XRD pattern suggests some SnO₂ was reduced to metallic Sn (JCPDS No. 86-2265)⁵⁴ in the carbon matrix resulting in coexistence of SnO₂ and Sn in the CMK-3. By further reduction of SnO₂ at higher temperature and hydrogen gas, it is confirmed by XRD pattern that all of SnO₂ were reduced to metallic Sn and the XRD pattern also suggests that Sn is agglomerated to become larger particles. X-ray photoelectron spectroscopy (XPS) was conducted to examine the chemical composition of the surface of SnO₂/Sn/CMK-3 composite. XPS spectrum proved that the material is composed of tin, oxygen and carbon elements (**Figure 3-10a**). High resolution spectrum for Sn element presents around 487 (Sn 3d_{5/2}) and 496 eV (Sn 3d_{3/2}) peaks for Sn⁴⁺ (**Figure 3-10b**). Another high resolution spectra shows peaks at around 531 and 285 eV, attributed to the O1s from SnO₂ and C1s from CMK-3, respectively (**Figure 3-10c,d**)⁴⁹. Based on those series characterization techniques, SnO₂ and (or) Sn materials were successfully incorporated into CMK-3, and that the composition of the Sn-based materials can be controlled by the annealing conditions. In addition, EDX and XPS proposed strong evidences of chemical composition of CMK-3.

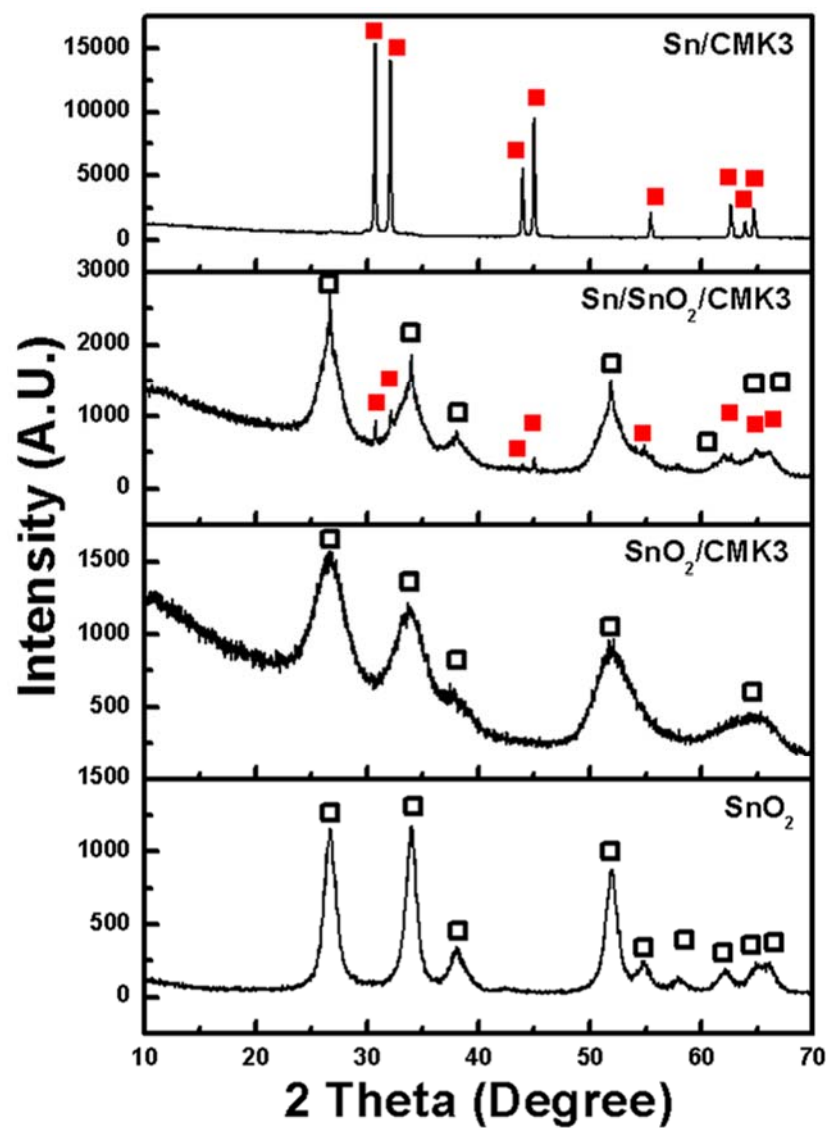


Figure 3-9. X-ray diffraction patterns of SnO₂, SnO₂/CMK-3, SnO₂/Sn/CMK-3, and Sn/CMK-3 composites.

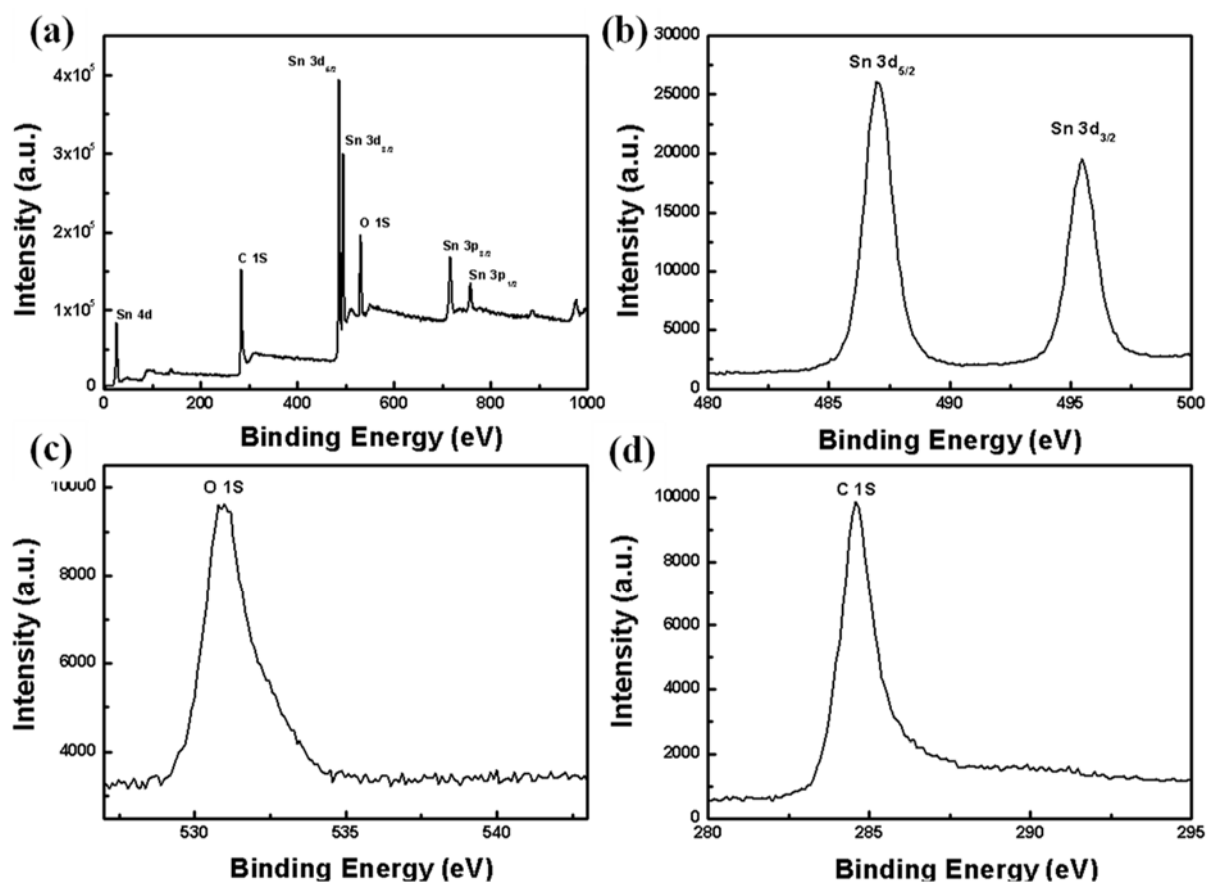


Figure 3-10. (a) low resolution XPS spectrum of SnO₂/Sn/CMK-3; high resolution XPS of (b) Sn3d, (c) O1s and (d) C1s in SnO₂/Sn/CMK-3.

Electrochemical performances were carried out by galvanostatic discharge and charge processes (**Figure 3-11**). **Figure 3-11b** demonstrates number of cycle with retention capacity of the series products that were synthesized in this work. **Figure 3-11a** exhibits voltage and capacity curves of initial, 2nd and 3rd cycles of SnO₂/Sn/CMK-3 electrode which shows superior cycle stability among the products. The electrode, consisting of SnO₂/Sn/CMK-3 with carbon black and polyvinylidene fluoride (PVdF) in a weight ratio of 70:10:20, is casted on a Cu current collector.

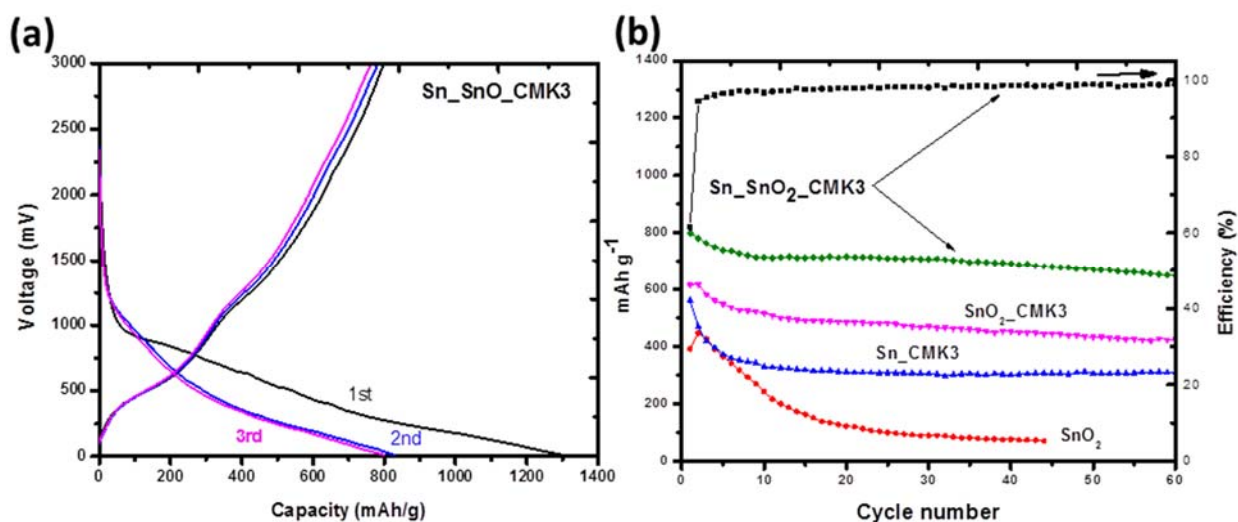
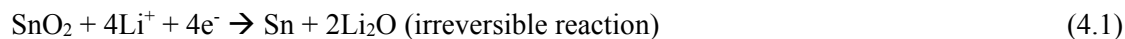


Figure 3-11. Galvanostatic (a) discharge and charge curves of SnO₂/Sn/CMK-3 composite, (b) charge capacity of SnO₂, SnO₂/CMK-3, Sn/SnO₂/CMK-3 and Sn/CMK-3 composites, and the Coulombic efficiency of Sn/SnO₂/CMK3, at current rate of 100 mA g⁻¹ with respect to the cycle number.

The initial cycle in **Figure 3-11a** shows large irreversible capacity which is caused by conversion reaction of SnO₂ with Li ion into Sn and Li₂O, a solid-electrolyte interphase (SEI) layer formation and some irreversible reaction of Sn and CMK-3 during Li insertion and extraction. The SnO₂ reaction mechanism has been proposed in other reports as below.^{39, 55, 56}



According to the curves of subsequent cycles, irreversible capacity sharply decreased, indicating that most of irreversible reactions occurred during 1st discharge. The Sn/SnO₂/CMK3 shows first cycle Coulombic efficiency of about 58%. This is attributed to the irreversible decomposition of SnO₂ into

active metallic tin surrounded by an inactive Li_2O matrix, in addition to SEI formation. Subsequently, the cycle efficiency is maintained at almost 100% as the cycle number increases up to 100 cycles (see **Figure 3-11 b**, and **Figure 3-12**). The initial charge capacities are 799, 616, 636, and 392 mAhg^{-1} for the $\text{SnO}_2/\text{Sn}/\text{CMK-3}$, $\text{SnO}_2/\text{CMK-3}$, $\text{Sn}/\text{CMK-3}$ and SnO_2 , respectively. As expected, metallic Sn contained materials give higher capacity based on their theoretical capacity^{54,57}. However, the capacity of $\text{Sn}/\text{CMK-3}$ is lower than $\text{SnO}_2/\text{Sn}/\text{CMK-3}$. This is attributed to the fact that increasing the Sn content resulted in larger Sn particle sizes which provide less reactivity for Li alloying/de-alloying process⁵⁸. After 30 cycles, retention capacities are about 88.6, 76.4, 49.6, and 22.7 % for the $\text{SnO}_2/\text{Sn}/\text{CMK-3}$, $\text{SnO}_2/\text{CMK-3}$, $\text{Sn}/\text{CMK-3}$ and SnO_2 , respectively. In particular, $\text{SnO}_2/\text{Sn}/\text{CMK-3}$ exhibits the best performances in terms of initial capacity and cycle stability, indicative a synergistic effect existing in mixed phase Sn-based materials. This is consistent with a recent report by Wen et al.⁴⁹ who observed improved capacity and cycle performance for graphene based composites in the presence of both Sn and SnO_x . It is assumed that metallic Sn contributes increase capacity and Li_2O matrix from SnO_2 during 1st discharge suppresses Sn particles from agglomeration among the particles during Li alloying/de-alloying processes.^{57, 59} Moreover, CMK-3 plays critical role for the electrochemical performances. CMK-3 provides 3-dimensional electron pathway and large contact sites for the Sn-based materials⁶⁰. Additionally, its 3-dimensional frameworks maintain electrical contact with Sn materials which are likely agglomerated and then severely changed in their volume as Li alloying/de-alloying proceeds and not only provide buffer space for the large volume change of Sn-based materials but also suppress the volume change. It is also worth noting that CMK-3 work as active material in the composite, partially contributing the specific capacity. These roles of CMK-3 can be directly supported by measuring the performance of Pure CMK3 (see **Figure 3.12b**). The initial cycle for pure CMK3 shows a first charge capacity of 430 mAh g^{-1} , the subsequent cycles show stable reversible capacity at about 390 mAh g^{-1} for more than 60 cycles. Additionally, referring to **Figure 3-11b**, $\text{SnO}_2/\text{CMK-3}$

composite demonstrates high initial capacity and acceptable cycle stability which is attributed to the functions of CMK-3 in the composite. However, Sn/CMK-3 composite does not present good cycle stability. It is assumed during the reduction of SnO₂ to metallic Sn, the particles were agglomerated to become bigger size and then could destroy the frameworks of CMK-3 during cycles. The growth of the size after conversion of SnO₂ into Sn was confirmed by the TEM image (**Figure 3-6**) and XRD patterns (**Figure 3-9**). The rate performance along with cycle stability of SnO₂/Sn/CMK-3 composite was tested and shown in **Figure 3-12**. The test was conducted from 100 to 800 mA g⁻¹ of the current density with 5 cycles to investigate cycle stability. At the highest current density of 800 mA g⁻¹ the composite exhibits around 350 mA h g⁻¹ with good stability which is close to the theoretical capacity of conventional graphite (372 mA h g⁻¹) that can be achieved at the current density of 30 mA g⁻¹⁶¹. Furthermore, it has been reported that at the similar current density, lower than 50 mA h g⁻¹ was obtained for the conventional graphite⁶¹.

In order to clarify the hybrid effect on the electrochemical performance of SnO₂/CMK3, we calculated theoretically the capacity of physical mixture of SnO₂/CMK3. We considered the theoretical capacity of SnO₂ as 782 mA h g⁻¹ and for CMK3 as 430 mA h g⁻¹ (estimated from **Figure 3.12b** and the maximum charge capacity). Considering the mass ratio of 58.2% SnO₂ and 41.8% CMK3 (as computed from TGA result **Figure 3-2**), the theoretical capacity of the hypothetical mixture can be calculated as follow:

$$\begin{aligned}
 C_{\text{theoretical for SnO}_2/\text{CMK3}} &= (C_{\text{SnO}_2} \times \text{mass}\% \text{ of SnO}_2) + (C_{\text{CMK3}} \times \text{mass}\% \text{ of CMK3}) \\
 &= 782 \times 0.582 + 430 \times 0.418 = 634.86 \text{ mA h g}^{-1}.
 \end{aligned}
 \tag{4.3}$$

Interestingly the observed capacity for SnO₂/CMK3 is 616.23 mA h g⁻¹ (based on the maximum charge capacity observed in **Figure 3-11b**). This value is comparable to the estimated theoretical capacity of

the hybrid SnO₂/CMK3 material. On performing similar calculation for the hybrid Sn/SnO₂/CMK3 material, assuming after annealing there is minimal change in mass ratio of tin to carbon and assuming both Sn and SnO₂ contribute 1:1 of their theoretical capacity which mean C_{theoretical} of Sn/SnO₂ is 888 mAh g⁻¹, then:

$$\begin{aligned}
 C_{\text{theoretical for Sn/SnO}_2/\text{CMK3}} &= (C_{\text{SnO}_2/\text{Sn}} \times \text{mass\% of SnO}_2/\text{Sn}) + (C_{\text{CMK3}} \times \text{mass\% of CMK3}) \\
 &= 888 \times 0.582 + 430 \times 0.418 = 696.56 \text{ mAh g}^{-1}.
 \end{aligned}
 \tag{4.4}$$

This value is less than the observed, for this material, in **Figure 3-11b** which is 798.64 mAh g⁻¹. This result points to a synergistic effect caused by embedding Sn nanoparticles along with SnO₂ into the nanochannels of CMK3. For the above estimated value, we assumed a Sn to SnO₂ ratio of 1:1; however in reality, the actual value of Sn is less. This means that the theoretical value should be less than 696.56 mAh g⁻¹ calculated for Sn and SnO₂ present in unity, and greater than 634.86 mAh g⁻¹ corresponding to only SnO₂ with CMK3. This emphasizes the synergistic effect that exists between these components, with a capacity observed in excess of those predicted herein.

It is not unexpected that the CMK3 under unseen structure conditions could show high specific capacity. Reference ⁶² showed that CMK3 may have a reversible capacity level up to Li_xC₆, where x = 2.3 to 3. However, a satisfactory explanation for this high capacity has not been yet developed. In order to account for the high specific capacity for Sn/SnO₂/CMK3, we have to think about the synergistic effect of the inclusion of Sn nanoparticles into SnO₂ where both are embedded into the nanochannels of the CMK3. This unique structure is believed to enable less activation over-potential for the Li intercalation into CMK3 leading to more usable sites and consequently increasing the overall charge capacity of the composite material.

Based on the rate capability and cycle stability results, it is proposed that the SnO₂/Sn/CMK-3 composite is an excellent negative electrode material for Li ion battery over the conventional negative electrode material.

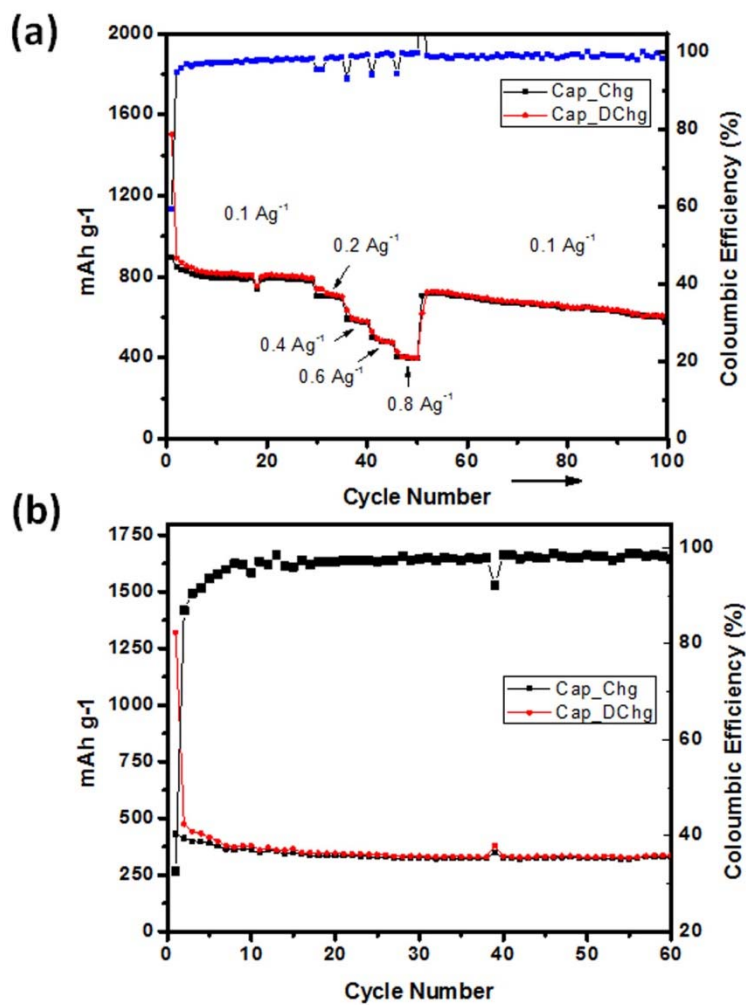


Figure 3-12. (a) Capacity of SnO₂/Sn/CMK3 at various current rates from 100 to 800 mA g⁻¹ with respect to the cycle number, (b) galvanostatic discharge and charge curves of pure CMK3 and the Coulombic efficiency at current rate of 100 mA g⁻¹.

Chapter 4 Growth of SiNW on graphene

The following section is based on previously published work by Hassan, F. M. et al⁶³

ACS Applied Materials & Interfaces 2014, **6**(16): 13757-13764

“Sub-eutectic growth of single crystal silicon nanowires grown on, and wrapped with, graphene nanosheets: A high performance anode material for lithium ion battery”

Reproduced with permission.

4.1 Introduction

The development of lithium-ion batteries (LIB) based on new high-performance materials is critical to meet the demands of an expanding array of mobile consumer and military electronics that incorporate this technology. Advances in the energy storage capabilities of LIBs is also integral to the future of electric transportation and grid scale energy storage, required to facilitate the integration of intermittent renewable energy sources into the grid. Specifically, alternative electrode technologies are needed to overcome the maximum theoretical capacity (372 mAh g^{-1}) of graphite anode materials and their poor capacity retention at high current density.⁶⁴⁻⁶⁹ Silicon (Si) has emerged as a strong candidate for the future of commercial LIB anode designs because of its high theoretical storage capacity in comparison to graphite (4200 mAh g^{-1}), natural abundance, low cost, and low discharge potential of 0-0.4 V vs Li/Li^+ .⁷⁰⁻⁷⁴

Unfortunately, the commercial application of silicon-based anodes faces several challenges that arise due to its low intrinsic electrical conductivity ($10^{-5} \text{ S cm}^{-1}$), along with extreme volume expansion (400%) that occur during the alloying process with lithium ($\text{Li}_{14.4}\text{Si}$). These volume expansions inevitably lead to pulverization of the electrolyte and/or rapidly degrading electrical connectivity of the

electrode, especially when using electrodes with high mass loadings.⁷⁵⁻⁸⁰ Furthermore, the intense lattice strain and surface stress can prevent stabilization of the solid electrolyte interphase layer (SEI), leading to low columbic efficiency. In efforts to overcome these challenges, various conductive-carbon composite materials have been utilized to encapsulate the silicon materials, thereby enhancing their performance retention after many cycles.⁸¹⁻⁹⁰ Additionally, tailored nanostructures, such as Si nanowires (SiNWs), nanotubes or nanoporous structures have been used to achieve better durability through a combination of increased strain tolerance, shorter diffusion distances and enhanced charge transport.⁹¹⁻¹⁰⁰

In this regard, there is an evolving array of methods used for both the bottom-up and top-down growth of SiNWs that have been successfully demonstrated on planar Si surfaces.^{101, 102} However, the commonly utilized bottom-up method for SiNWs growth is the vapor-liquid-solid (VLS) catalytic growth mechanism, using gold (Au) nanoparticles that are chosen for their relatively low eutectic point.¹⁰³⁻¹⁰⁵ In addition to the aligned vertical growth SiNWs being demonstrated on Si(111) wafers using the VLS approach, SiNWs have also been grown on other substrates, such as Al₂O₃.^{106, 107} Practical safety risks of the commonly used SiH₄ gas precursors and the high cost of Au are however a major drawback to these methods. Additionally, the production capabilities are also limited due to the requirement of using well-defined 2D-planar surfaces as the growth substrate. To address this, it is recognized that new methods, which employ inexpensive catalyst metals and are applicable to bulk production of SiNWs, must be developed in order to capitalize on the highly promising application potential of these materials.^{38, 45-47} Recent investigations towards this goal includes the growth of SiNWs on Au-coated Al₂O₃ particles,¹⁰⁶ and in work concurrent to our own, the VLS growth of SiNWs from Au nanoparticles on the surface of reduced graphene oxide (rGO).¹⁰⁸

Herein we present a scalable method for the bottom-up processing of carbon-coated SiNWs on graphene (c-SiNW-G) using an inexpensive nickel nanoparticle (NiNP) catalyst. This procedure

involves a sophisticated one-pot atmospheric pressure chemical vapor deposition (APCVD) synthesis, which incorporates several novel techniques. First, a uniform distribution of NiNPs on the surface of graphene was achieved by thermally shocking a mixture of nickel nitrate and graphene oxide, resulting in rapid decomposition of the nickel nitrate precursor and simultaneous *in situ* reduction of the graphene oxide. Second, the SiNWs were grown on the NiNP catalysts by applying a unique variation to the silicide-assisted Vapor-Solid-Solid (VSS) mechanism.^{101, 109-111} The seed particles remained in the solid phase because of the sub-eutectic temperature of 900°C,¹¹¹ well below the 993°C eutectic temperature required for the Ni-Si system to undergo a VLS growth mechanism.¹⁰¹ Furthermore, by exchanging the SiCl₄ precursor after SiNWs growth with toluene, we illustrate a core-shell SiNW/C structure can be obtained. In addition to the elimination of expensive Au catalysts using this method, the ability to grow SiNWs anchored on graphene using SiCl₄, along with the introduction of a controlled carbon coating by the injection of toluene represents a significant step toward the future development of practical high performance materials for LIBs. By growing SiNWs directly on graphene, a direct path is provided for electrical conductivity. Furthermore, by decorating the graphene sheets with well dispersed NiNPs, it provides a template for growing individual SiNWs that are not agglomerated together.

4.2 Experimental Methods

4.2.1 Synthesis of SiNW-G

Prior to growing SiNWs on graphene and the fabrication of well dispersed NiNPs, graphene oxide (GO) was synthesized by a modified Hummer's method.¹¹² In a typical experiment, 150 mg of GO was dispersed in deionized water followed by drop-wise addition of 300 μ L of 0.1M nickel nitrate hexahydrant (Ni(NO₃)₂·6H₂O). The mixture was sonicated for 30 minutes and then left to dry at 60 °C

under magnetic stirring. The GO-nickel nitrate mixture was then transferred to a quartz tube inside a furnace and rapidly pushed into the hot-zone at 700 °C and held under argon atmosphere for 1 hour. The temperature was then increased to 900 °C and H₂ gas was purged for 30 minutes at 500 sccm before injecting 300 μL of SiCl₄ into the quartz tube. After the SiCl₄ was completely depleted and the SiNW-G grown, toluene was injected (typically 50 μL) as a source of the carbon coating, before cooling the furnace down. The process generated approximately 30 mg of c-SiNW-G powder containing 48 wt% SiNW.

4.2.2 Electrode fabrication

Battery electrodes were fabricated by mixing the active c-SiNW-G material (70 wt.%) with polyacrylonitrile (PAN, 30 wt.%) and casting the slurry on a copper foil current collector. No further carbon additives were used. The electrodes were then heat treated at 550 °C for 2 hours in Argon atmosphere to enhance the three dimensional conductivity of the composite electrode by partially-pyrolyzing the polyacrylonitrile binder. The initial starting thickness of the electrodes were about 15 μm. The electrode remained intact and well attached to the current collector after heat treatment.

4.2.3 Electrochemical performance

Coin cells were assembled in an argon-filled glove box using the treated electrodes versus metallic lithium and using 1 M LiPF₆ in 30 wt % ethylene carbonate (EC), 60 wt % dimethyl carbonate (DMC), and 10 wt % fluorinated ethylene carbonate (FEC). Galvanostatic cycling was initially performed between 0.01 – 2 V at 100 mA g⁻¹ (C/20) for 5 cycles. After initial cycling the current rate was varied: one cell remained at 100 mA g⁻¹ current for 100 cycles, and another cell was cycled at incremental rates of 0.1 A g⁻¹, 0.5 A g⁻¹, 1 A g⁻¹, 2 A g⁻¹, 4 A g⁻¹ and 10 A g⁻¹ to determine the rate capability of the

materials. As a reference material, graphene was tested under the same conditions and electrode preparation. Cyclic voltammetry (CV) was also performed, utilizing a 0.01-2 V range. In all measurements, the total mass of the electrode, including the mass of the silicon and the mass of the graphene, was considered when carrying out capacity calculations.

4.2.4 Characterization

Morphology of the electrode surfaces before and after treatment were characterized by scanning electron microscopy (SEM) using a LEO FESEM 1530 and transmission electron microscopy (TEM) using a JEOL 2010F TEM/STEM field emission microscope equipped with a large solid angle for high x-ray throughput, scanning, scanning-transmission and a Gatan imaging filter (GIF) for energy filtered imaging. Raman scattering spectra were recorded on a Bruker Senterra system (532 nm laser). Thermal Gravimetric Analysis (TGA) (TA instrument Q500, USA) was used to determine the mass ratio of graphene to SiNW. TGA testing was performed in air with a temperature range of 25 °C to 900 °C and a ramp rate of 10 °C min⁻¹. XRD analysis was conducted using monochromatic Cu K x-rays (0.154 nm wavelength) and an Inel XRG 3000 diffractometer.

4.3 Results and Discussions

To verify the production of uniformly distributed NiNPs as a catalyst for SiNW growth, the samples were removed from the furnace after the initial thermal shock to decompose and reduce the NiN/GO mixture. The SEM image in **Figure 4-1a** illustrates that small, approximately 10-20 nm NiNPs uniformly distributed across the entire surface of graphene were formed from the decomposition of the crystallized salt clusters. In **Figure 4-1b and 4-1c**, after injecting the SiCl₄ and later toluene, worm-like nanowires coated with carbon could be clearly observed by both SEM and TEM, respectively,

lying flat along the basal plane of graphene. High angle annular dark field (HAADF-STEM) imaging of the materials, which is very sensitive to atomic number, is shown in **Figure 4-2a**. This imaging technique creates an obvious variation in contrast which was used to probe the elemental distribution of the materials and to verify that the NiNPs do indeed catalyze and anchor the nanowire growth. Further, to prove the Si nanowire composition was not mistaken for carbon nanostructures formed during toluene injection, we additionally performed EDX mapping. The result shown in **Figure 4-2a-d** clearly depicts the presence of SiNWs anchored to the NiNP catalyst. Furthermore, the blanketed carbon in **Figure 4-2c** and amorphous region at the SiNWs edge in **Figure 4-1d** indicate successful coating of a very thin carbon layer on the SiNWs, in addition to the underlying graphene support.

High resolution TEM imaging and the corresponding FFT spectrum for the SiNW-G composites (**Figure 4-1d and 4-1e**) reveal that the SiNWs exhibits a single crystalline structure with 0.31 nm lattice spacing. This indicates that growth is oriented along the (111) crystal plane. In agreement with a previous fundamental investigation, the rapid heat treatment of the Si source and the resulting (111) crystal orientation suggests the formation mechanism involves generation of an intermediate NiSi phase, which promotes (111) crystal growth.^{109, 110} Using an inexpensive Ni catalyst to control the axial orientation in the $\langle 111 \rangle$ direction also suggests an increased percentage of (110) facets, which offer increased lithium ion diffusion into the core of the SiNWs,¹¹³ which promotes high-rate capabilities. The formation of a thin 2nm layer of amorphous carbon on the surface of the SiNWs is also confirmed by high-resolution TEM (Figure 5.1d). The carbon coating is intended to provide additional electronic conductivity, protect against surface oxidation of the narrow SiNWs and partially restrict expansion due to lithiation.

To validate the proposed VSS growth mechanism on NiNPs, it is important to eliminate any concern that graphene may assist in the catalysis.^{114, 115} This would further help to verify the versatility of this inexpensive preparation method. To accomplish this, SiNWs were also produced without the addition

of graphene oxide, by growing SiNWs using SiCl_4 precursor directly on bulk NiNPs after thermal decomposition of the nickel nitrate. This is illustrated by the characteristic TEM image shown in **Figure 4-1f** and the EDX mapping shown in **Figure 4-2e and 4-2f**. Bulk preparation of pure SiNWs grown by this methodology could be applied in the future towards various applications, without the need to anchor the NiNPs on a specific support material.

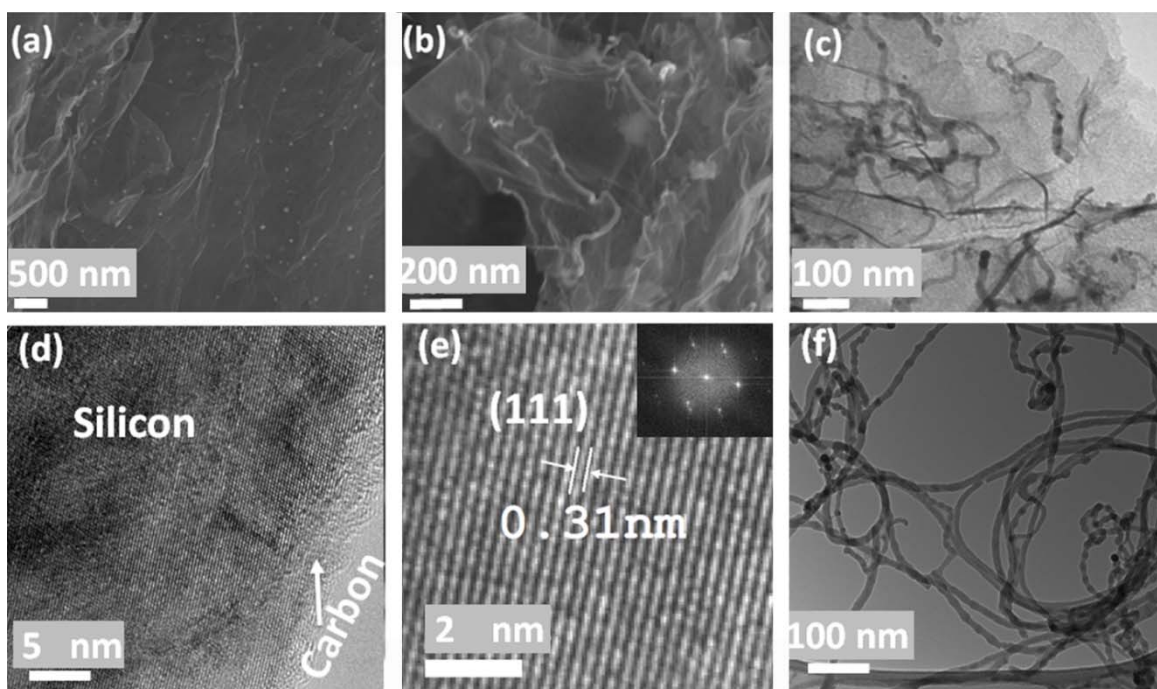


Figure 4-1. SEM images of a) Ni nanoparticles formed on graphene after thermal shock reduction of the nickel nitrate and GO mixture and b) the resulting SiNWs grown on the intermediate in (a). c) TEM image of the c-SiNW-G composite, d) increased magnification TEM image representing the SiNWs within the c-SiNW-G composite, e) HRTEM and a corresponding FFT diffraction pattern shown in the inset for the SiNW, and f) the TEM image for SiNWs grown without graphene support.

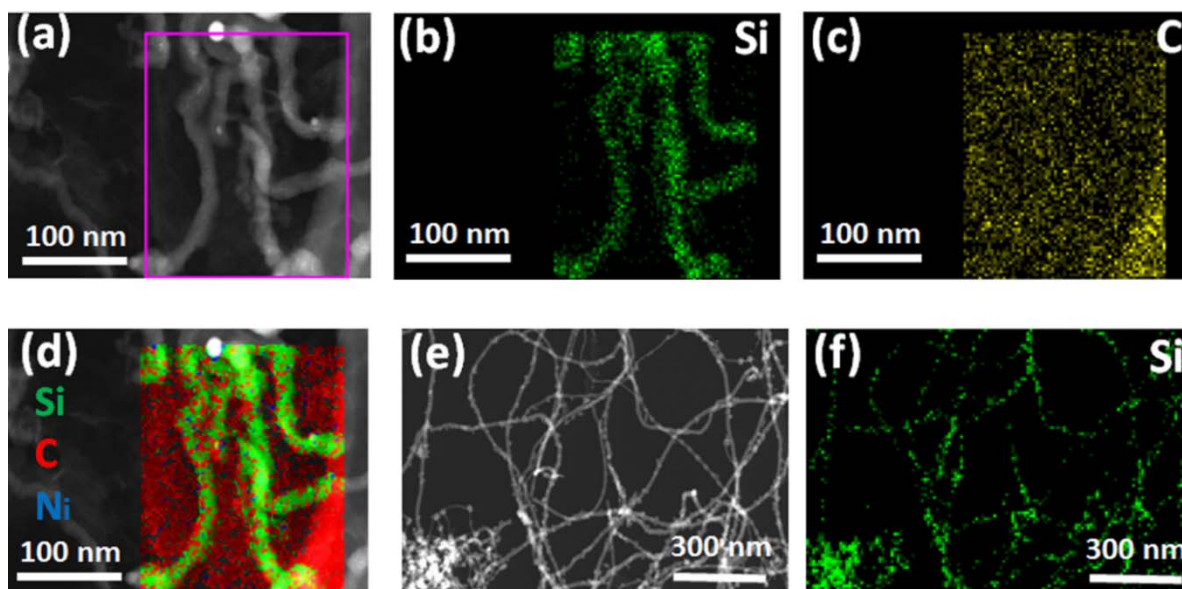


Figure 4-2. a) HAADF-STEM (High-Angle Annular Dark-Field) of c-SiNW-G , b) EDX mapping of Si for the area marked in (a), c) EDX mapping of carbon, d) overlapping projection for the Si, C and Ni spectrums measured in c-SiNW-G, e) HAADF-STEM of SiNWs grown without graphene , and f) the EDX mapping for Si in (e).

The structure of the c-SiNW-G composites was further investigated by XRD and Raman spectroscopy (**Figure 4-3**). As expected, the XRD (**Figure 4-3a**) patterns are consistent with a reference database pattern for the Si phase. No further residual peaks were observed in the c-SiNW-G composites that might correspond to residual nickel silicide or SiO_x . It was also expected that for rGO, a broad low intensity peak at $\sim 25^\circ$, which represents a shift to the inter-planar spacing interactions of graphite (002) might be observed. The absence of this peak suggests that the strong signal of the SiNWs and their presence in between the rGO sheets may suppress the weak graphitic interaction after GO reduction. However, three characteristic peaks observed in the Raman spectrum provided in **Figure 4-3b** confirms the presence of rGO after completing the one-pot synthesis. The first peak verifies the lattice vibration of crystalline Si (520 cm^{-1}), while the other two highlight the presence of reduced graphene oxide within

the composite. The absence of Si-O-Si vibration and stretching peaks below 1000 cm^{-1} suggests minimal oxidation to the surface of the carbon-coated SiNWs during or after growth.^{100, 116, 117} Furthermore, the strong D ($\sim 1350\text{ cm}^{-1}$) and G ($\sim 1580\text{ cm}^{-1}$) band peaks respectively signify a variety of planar defects and the restoration of sp^2 binding within the graphitic lattice, respectively^{118, 119}. **Figure 4-3c** demonstrates the TGA profile for the c-SiNW-G electrode material after annealing. As the temperature increases, a significant mass loss is observed from ca. 610 to 720 °C due to the carbon content being burned away. Following this, a mass increase is observed at higher temperature, which can be ascribed to the oxidation of silicon to silicon oxide. As a result, the Si wt.% in the c-SiNW-G is about 48%.

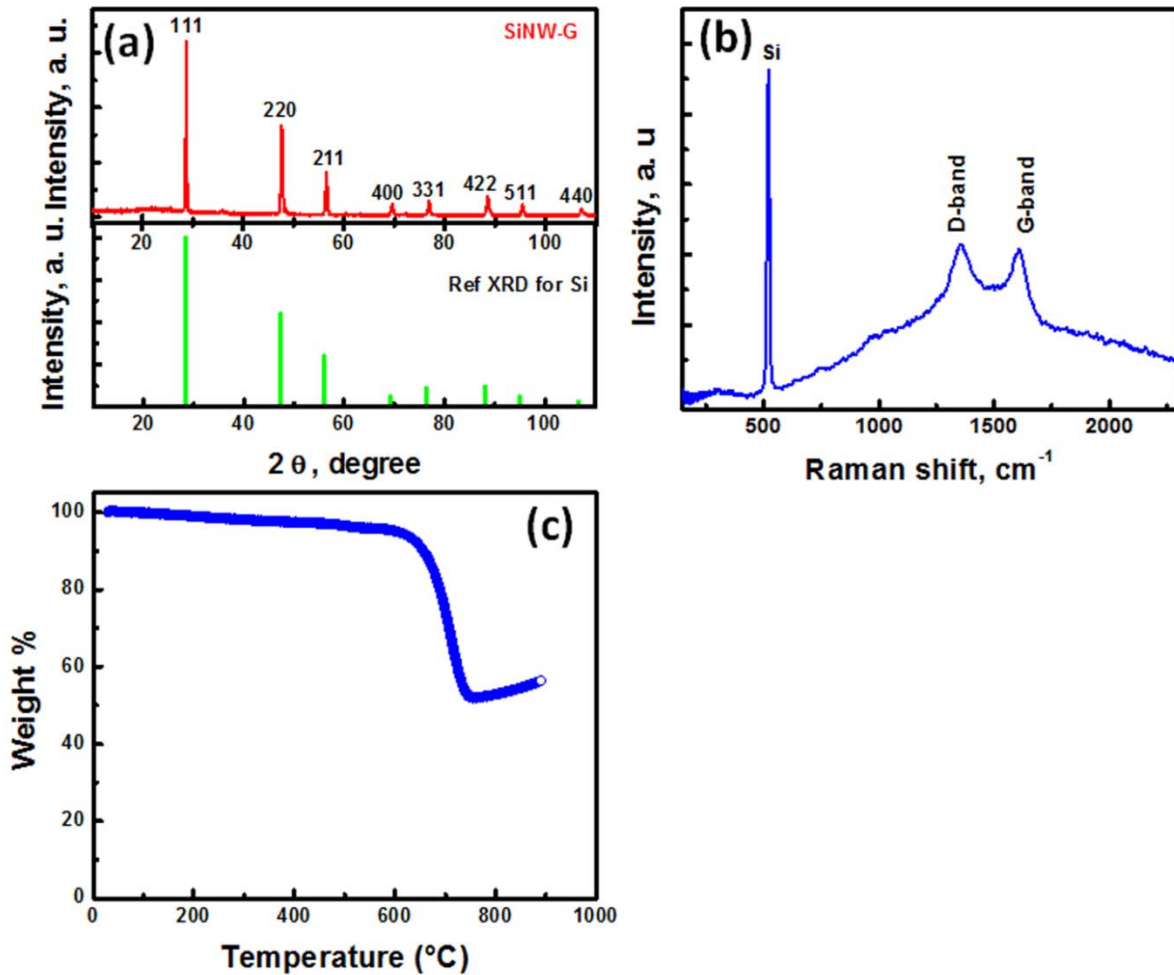


Figure 4-3. a) XRD diffraction patterns for the as-synthesized c-SiNW-G (top) and the reference XRD spectrum measured for SiNP (bottom). b) Raman spectroscopy for c-SiNW-G. c) TGA analysis for c-SiNW-G.

In order to demonstrate the potential application of the SiNWs prepared using the inexpensive nickel catalyst, a series of investigations was conducted to determine the electrochemical performance in LIBs. The c-SiNW-G was dispersed as the active material in a slurry and deposited on a copper current collector before partially carbonizing the PAN binder. The anodes were then assembled into coin cells

with a lithium counter electrode and underwent galvanostatic charge-discharge (CD) cycling, cyclic voltammetry (CV) and electrochemical impedance spectroscopy (EIS).

Figure 4-4a illustrates the CD voltage profile for the c-SiNW-G anodes cycled between 0.01-2 V @ 0.1 A g⁻¹. A large plateau in the first discharge cycle corresponds to the expected behavior of crystalline Si. Beyond the 1st cycle, the observed changes in the voltage profile are attributed to amorphization of the initially crystalline SiNW structure. This is supplemented by the added irreversible first cycle capacity loss of graphene (**Figure 4-5, inset**)¹²⁰⁻¹²². The 1st cycle discharge capacity is 2200 mAh g⁻¹ with a coulombic efficiency of 64%. The second cycle has a capacity of 1416 mAh g⁻¹, followed by a gradual decrease to only 931 mAh g⁻¹ at the 30th cycle. However, as depicted by the cycle rate test in **Figure 4-4c**, at higher current densities up to 10 A g⁻¹ the c-SiNW-G composite was remarkably still able to deliver reversible capacity of 400 mAh g⁻¹, providing sufficient electron and ion transport to support the partial lithiation reaction. Even after 70 additional cycles at 2 A g⁻¹ the c-SiNW-G composite remained highly stable (730 mAh g⁻¹). The charge-discharge profile in **Figure 4-4d**, taken from the last cycle of each rate investigated, reveals minimal variation in the shape or voltage of the plateau region below 2 A g⁻¹, although at higher current density the development of slightly increased slope and overpotential is observed. When further compared to pure graphene or pure SiNW active materials in the electrodes, there was a strong synergistic effect present for the c-SiNW-G. This synergy greatly improved capacity retention at high charge/discharge rates (~3.5x improvement at 2 A g⁻¹ and ~10x at 10 A g⁻¹). To fully illustrate the rapid transport capabilities of the c-SiNW-G composite, a newly assembled cell underwent three conditioning cycles at 100 mA g⁻¹ before directly cycling at a high current density of 6.8 A g⁻¹. As shown in **Figure 4-4e**, after 100 cycles, a stabilized capacity of 550 mAh g⁻¹ was achieved. **Figure 4-4b** compares the cycle performance, at 0.1 A g⁻¹, for c-SiNW-G, with the non-carbon coated SiNW-G, and graphene. The figure shows that introduction of a thin carbon layer to SiNW-G significantly improves the cycle stability. Through heat-treatment of polyacrylonitrile

(PAN), its structural changes that include reconstruction of the conjugate pi bonding leads to enhanced conductivity¹²³. This is the reason that PAN was selected as an ideal binder in this work. To show this effect, we fabricated a cell using sodium salt of carboxy methyl cellulose (NaCMC) as a binder under the same conditions, although with elimination of the heat treatment step. This sample is labelled as c-SiNW-G-CMC, and its cycle performance shown in **Figure 4-4b** demonstrates that its performance gradually decreases in comparison to the sample with PAN.

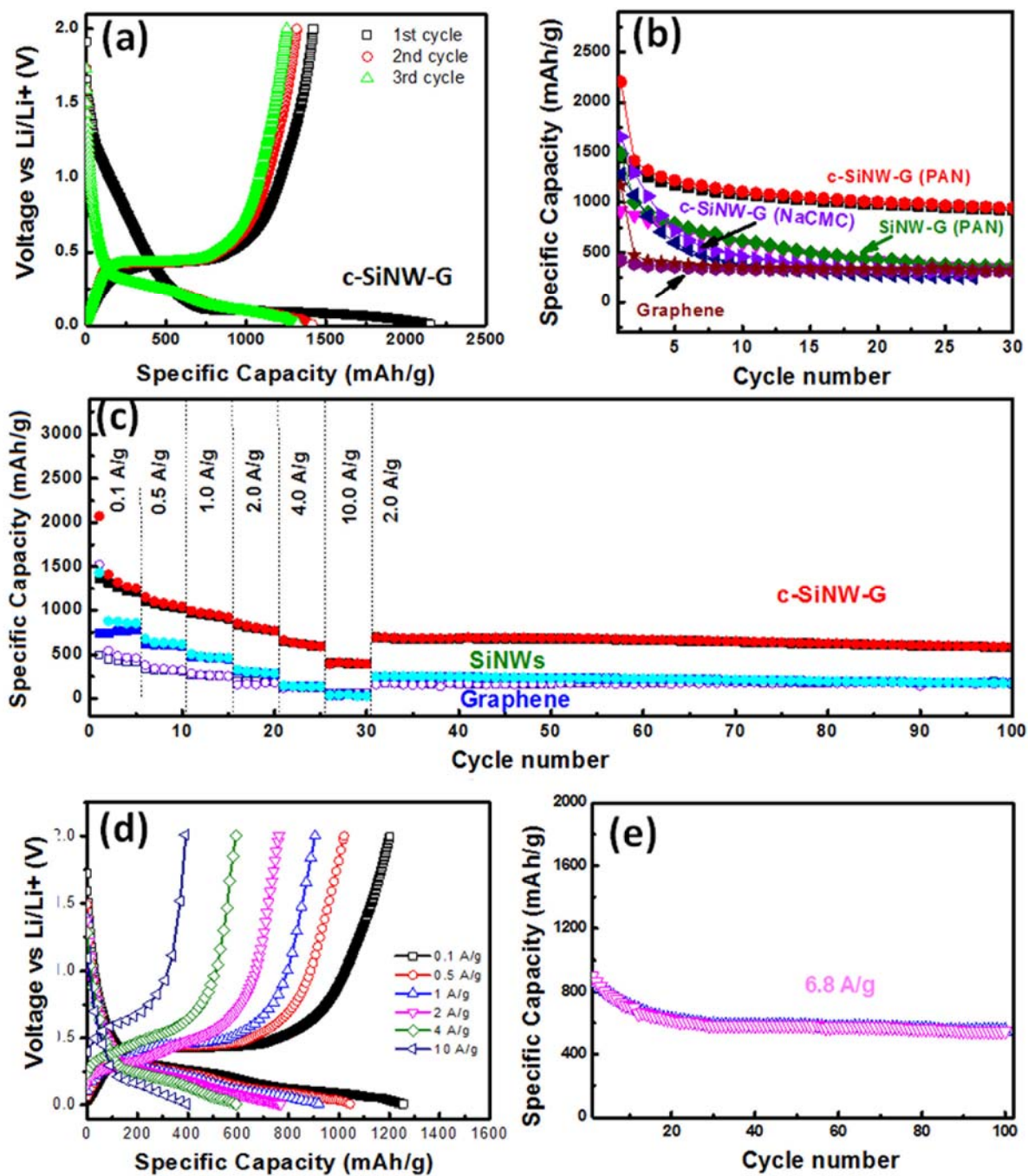


Figure 4-4. a) Voltage profile for a coin cell containing c-SiNW-G cycled at 0.1 A g⁻¹, b) comparison of the cycle capability of SiNW-G with and without carbon coating using PAN, and c-SiNW-G using NaCMC, to that of pure graphene at 0.1 A g⁻¹, c) is the rate capability of SiNW-G compared to the

non-supported SiNWs, and graphene, d) is a comparison of the voltage profile of SiNW-G at various currents, and e) is the cycle capability of SiNW-G at 6.8 A/g. (N.B. All capacities are based on the mass of silicon and graphene).

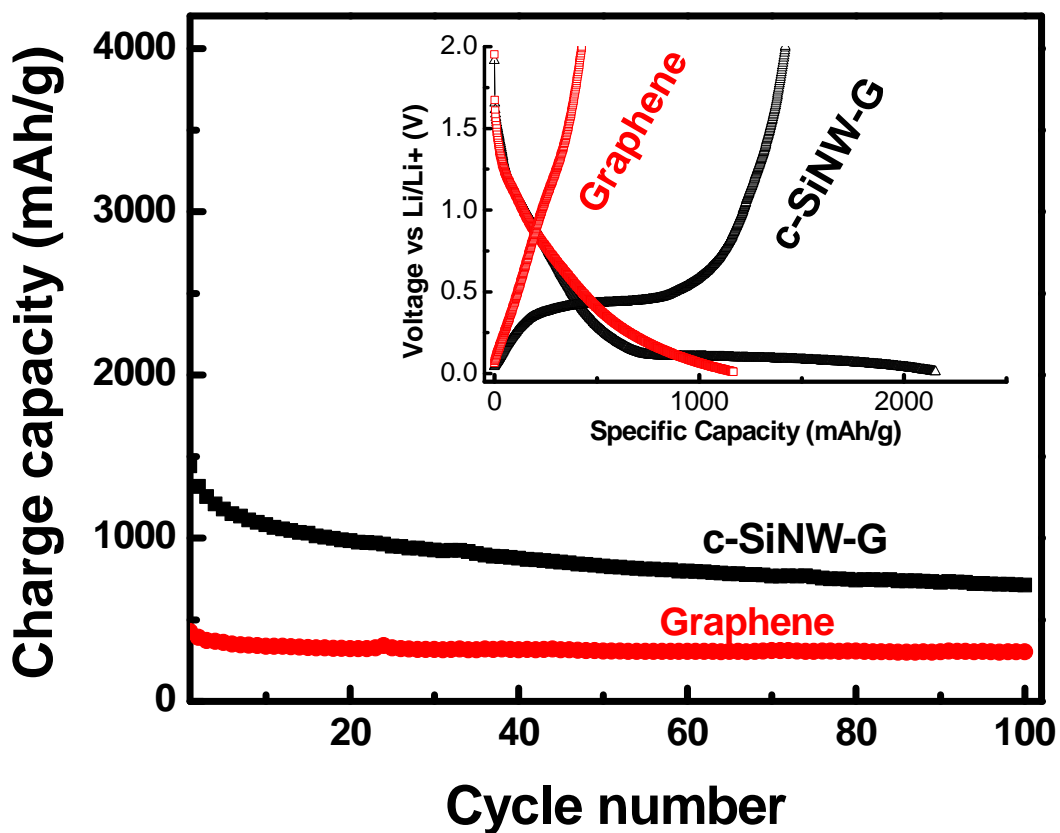


Figure 4-5. Cycle performance of c-SiNW-G in comparison with graphene, the inset is the corresponding voltage profile.

Electrochemical cycling of c-SiNW-G by CV in **Figure 4-6a** illustrates a first cycle peak starting at 0.15 V corresponding to the cathodic lithiation of crystalline Si to form Li_xSi . The anodic peaks at 0.32 V and 0.51 V correspond to the delithiation of Li_xSi back to Si. Subsequent cycles show an additional cathodic peak appearing at 0.20 V which becomes broader and stronger with each of the initial cycles. Together with the increasing strength of the anodic peaks at 0.32V and 0.51 V, these observations relate to a gradual activation of the SiNWs materials and a degradation of Si crystallinity with the alloying/de-alloying mechanism. The impedance spectra (**Figure 4-6b**) for the lithium-ion cells were modelled using the equivalent circuit provided in the **Figure 4-6b (inset)**. In this circuit, R1 represents the contact resistance (or the electrode series resistance), R2 and R3 are the charge transfer resistances, CPE1 and CPE2 are the capacitances, and W is the Warburg diffusion resistance. A table of these calculated values is provided in **Table 4**. The general trend is that the graphene based lithium ion cell has relatively lower contact resistance values, which likely arise due to the high conductivity of graphene. The carbon coated SiNWs on graphene showed a synergistic enhancement of the performance represented by the lowest charge transfer resistance. This may be attributed to the enhanced conductivity provided by the carbon coating throughout the entire 3D structure.

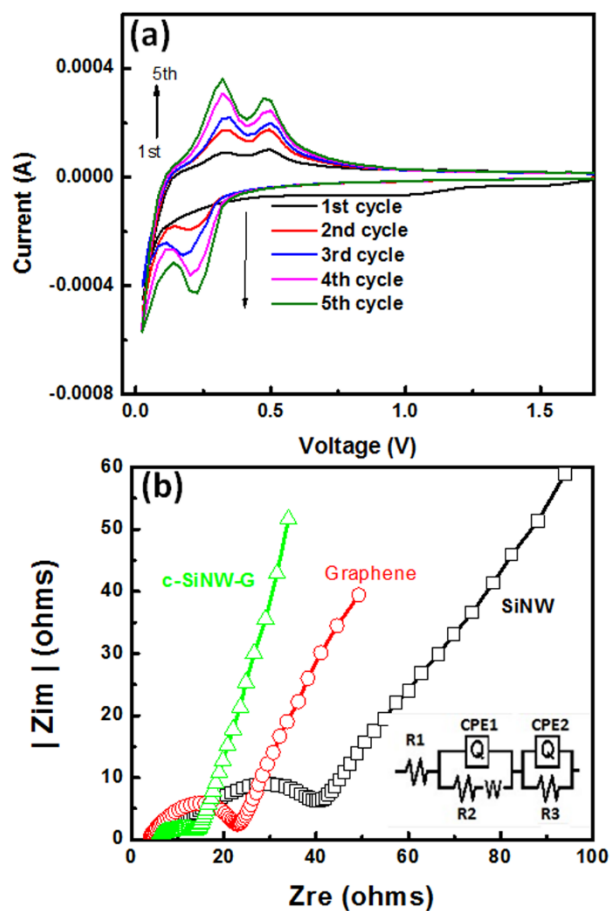


Figure 4-6. a) Cyclic voltammogram for a coin cell fabricated using c-SiNW-G, b) EIS for coin cells fabricated using c-SiNW-G, SiNWs, and graphene.

Table 4. List of the equivalent circuit parameters of the modelled EIS data for the lithium ion cells.

Parameter	c-SiNW-G	G	SiNW
R1 (ohms)	4.65	3.84	7.88
R2 (ohms)	4.83	4.00	16.06
R3 (ohms)	10.08	19.87	13.20

After cycling at high current density the SiNW-G anodes were extracted from their assembly and rinsed to remove the electrolyte. This was done to image the structural retention of SiNWs and to investigate amorphization of the (111) crystal plane after cycling. As previously mentioned, crystallinity along the axis of the wire would promote diffusion and would support the excellent capacity retention and cycle durability at high current density. A fundamental study which monitored in-situ lithiation/delithiation of SiNWs, noted stress occurs primarily at the Si-Si bond between the (111) planes during cycling, potentially leaving the crystal plane partial intact along the optimally oriented (111) nanowires.^{92, 113} As depicted by TEM microscopy in **Figures 4-7a and 4-7b**, there was a general retention of SiNWs morphology, despite significant fragmentation and swelling of the SiNWs. However, after the amorphization of Si and degradation during cycling, HRTEM imaging and the corresponding FFT of the SiNW-G composites in **Figure 4-7c** clearly shows no visible retention of crystallinity in the (111) plane. EDX mapping in **Figures 4-7d-f** confirms the entangled SiNWs within the body of the carbon composite. Further, the oxygen presence corresponds to the formation of SEI and residual electrolyte that was not removed after rinsing the electrodes.

In summary, we have developed a simple, one-pot synthesis methodology capable of growing bulk SiNWs on a low cost NiNPs catalyst. Furthermore, we illustrated the potential for these NiNPs to be simultaneously anchored to three dimensional support materials, enabling a large range of future application areas for this method of (111) SiNWs growth. After growing the carbon coated c-SiNW-G composite, we were able to show its excellent durability and retention of capacity at high current density (100th cycle: 550 mAh g⁻¹ @ 6.8 A g⁻¹) an anode in a LIB cell. Ultimately, this process creates an important building block for a new wave of low cost, high rate, silicon nanowire materials.

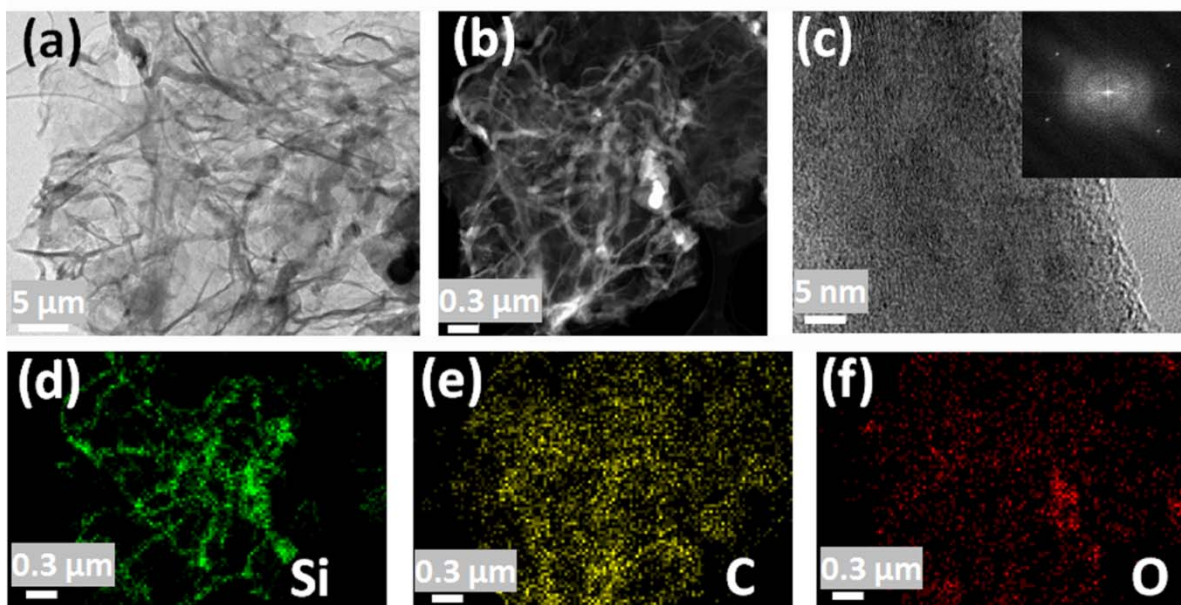


Figure 4-7. a) TEM image for SiNW-G electrode material after 100 cycles. b) HAADF-STEM, c) HRTEM, and d-f) EDX mapping for the elements silicon, carbon and oxygen, respectively, in SiNW-G after cycling.

Chapter 5 Engineered Si electrode nano-architecture

The following section is based on previously published work by Hassan, F. M. et al¹²⁴

Nano Letters, **14** (2014) 277.

“Engineered Si electrode nano-architecture: A scalable post-fabrication treatment for the production of next-generation Li-ion batteries”

Reproduced with permission.

Also these results were submitted as part of a patent application.

Z. Chen, F. M. Hassan , US provisional patent “A simple low cost treatment technology for high capacity silicon based lithium ion battery”, filed on July 30, 2012 , USPTO, #:61/741,868.

5.1 Introduction

The pursuit of high performance lithium-ion battery materials is critical for applications including electric vehicles, consumer electronics and the storage of renewable energy. This requires a new generation of electrode materials with higher energy density and long cycle life, without compromising low production costs, safety or the scalability necessary for commercial deployment^{64, 65, 67, 114, 125}. Silicon (Si) has emerged as a strong candidate to replace graphite as the anode material in commercial LIB design¹²⁶. Its appeal arises from a high theoretical storage capacity of $\sim 4200 \text{ mA h g}^{-1}$, natural abundance and low cost, and low working potential 0-0.4 V vs. Li/Li⁺^{70, 71}. However, the extreme volume change ($\sim 400\%$) experienced during lithiation/delithiation results in pulverization of the silicon and loss of the electrical connection, leading to rapid capacity loss^{72, 77, 79, 80}. In addition, the solid

electrolyte interphase (SEI) layer on the Si surface, which has to bear the same volume expansion and contraction, will also crack, fracture, or delaminate from the Si, leading to low Columbic efficiency¹²⁶.

To inhibit expansion and overcome this limitation, one of the most attractive strategies is to tailor the nanostructure and buffer the mechanical strain by preparing Si/C composites, dispersing silicon particles within or coating them with a porous carbon^{80, 127-130}. These techniques intend to improve cycle stability of Si, minimize direct exposure of Si to electrolyte to improve current efficiency, and enhance the electrical connection between Si and C. In a different strategy, Si-based electrodes can be directly prepared by the inclusion of commercial Si nanoparticles mixed into a functional polymer binding matrix¹³¹⁻¹³⁶. In addition, the covalent linkages between the binder and the SiO₂ surface layer on the Si particles can mitigate the mechanical damage caused by severe volume change, while providing an elastic network that extends throughout the entire electrode and maintains the electrodes integrity. However, these techniques are sensitive to: the dispersion quality of the active materials, a physically bonded Si-C interphase that becomes ineffective after cycling and the high inactive carbon/binder content required to achieve stable capacity¹³⁷⁻¹⁴⁰.

Progressively, higher performance and more durable configurations have been achieved by utilizing sophisticated methodologies to produce Si and Si@carbon core-shell nanowires^{73, 98, 99, 102, 141, 142}, as well as, porous composite structures coated with Si nanoparticles¹⁴³⁻¹⁴⁵. However, most of these reports utilize SiH₄, an expensive and extremely hazardous gas, and delicate multi-step treatments of synthesized nano-structured silicon. Controlled growth of SiO₂ coatings on these materials have also been shown to significantly decrease volume expansion, improving capacity retention during cycling when the coating was optimized to between 2-10 nm^{146, 147}. For comparison, a recent report by *Wang et al* reveals nanowire performance retaining 1100 mA h g⁻¹ after 1000 cycles⁹⁷. This is in agreement with

previous investigations concerning carbon coating of Si particles, prior to cell assembly. The studies suggest that the main advantage of PVDF is release of HF which cause localized etching of SiO₂ during carbonization, thereby controlling layer thickness¹⁴⁸⁻¹⁵⁰.

In this present work, we present a safe, economical and short duration strategy for post-treatment of Si electrodes made with commercially-available Si-nanopowder (NP), to achieve high-performance. The single-step flash heat treatment (FHT) process, which simultaneously engineered the electrode matrix and the surface architecture of Si, is compatible with continuous roll-to-roll electrode processing. To our knowledge, this is the first time that the direct engineering of the electrode structure by the rapid post-treatment of commercial Si particles has been reported to be successful. Specifically, the benefits of the FHT post-process include: (1) the creation of a SiO₂/C shell around the Si-NP which restricts volume expansion and stabilizes the SEI layer; (2) the carbonized binder generates a dense cellular network throughout the entire electrode, interconnecting the Si particles, boosting the electrical conductivity, and attributing to the enhanced electrode integrity and ; (3) manipulation of the copper current collector to catalyze graphene growth, resulting in a strong interfacial contact mechanically and electrically. In addition, all the binders were converted into graphitic carbon, which should give the electrode much better durability in the electrochemical environment. Also, the dispersion of Si powder in the binder before the FHT treatment would be much better since no conductive additive is needed. All of those synergetic functions contribute to the significantly improved performance in terms of cycle stability and rate capability (500 cycles, retaining capacity of 1150 mA h g⁻¹ at a high discharge rate of 1.2 A g⁻¹).

5.2 Experimental Methods

Electrodes for lithium ion battery testing were fabricated using commercially available silicon nanoparticles (Si-NP) with size range 50-70 nm was purchased from *Nanostructured & Amorphous Materials, Inc., Houston, USA*. For the working electrode, a slurry consisting of 60 % of active material (Si-NP) and 40 % polyvinylidene fluoride (PVdF) as a binder (with no conducting materials added) was prepared in N-methyl-2-pyrrolidone (NMP) and was coated on Cu foil. The average mass loading of silicon on the electrodes was 0.5 mg cm^{-2} . The electrode was dried in a convection oven at 353 K for 1 hr, followed by drying in the vacuum oven at 363 K for overnight. The electrodes were then subjected to the FHT process, see below. Coin type half cells were fabricated in an argon-filled glove box with the working electrode and a Li metal counter electrode. A polypropylene separator was employed to separate the two electrodes and the electrolyte composed of 1M LiPF_6 in 30 wt% ethylene carbonate (EC), 60 wt% dimethyl carbonate (DMC), and 10wt% fluorinated ethylene carbonate (FEC). Galvanostatic charge/discharge test was carried out at a cut off voltage range of 0.05 to 1.00 V with different current densities for rate capability testing. Cyclic voltammetry, at a scan rate of 0.05 mV s^{-1} between 1.0 and 0.05 V, and electrochemical impedance spectroscopy were conducted using a Princeton Applied Research VersaSTAT MC Potentiostat. For a reference coin cell, an electrode was prepared with the ratio of 60 wt% Si-NP, 20% Super-P as a conductive material and 20% polyvinylidene fluoride (PVdF) as a binder. These electrodes were used without FHT treatment.

Flash heat treatment (FHT): electrodes were placed into a long quartz tube of a horizontal tube furnace such that they are kept outside the furnace during heating up to 900 °C. Once the temperature reached 900 °C, the quartz tube was cautiously introduced into the furnace for rapid thermal shock of the electrodes, held for 20 minutes, then dragged back for rapid cooling. The treatment was performed under gas flow of 100 SCCM Ar/10%H₂.

Morphology of the electrode surfaces before and after treatment were characterized by scanning electron microscopy (SEM) (LEO FESEM 1530) and transmission electron microscopy (TEM) JEOL 2010F TEM/STEM field emission Transmission Electron Microscope, with a large solid angle for high X-ray throughput, scanning, scanning-transmission and a Gatan imaging filter (GIF) for energy filtered imaging and electron energy loss spectroscopy. Raman scattering spectra were recorded on a Bruker Sentterra system (532 nm laser).

5.3 Results and Discussions

5.3.1 FHT treatment and electrode structure

Figure 5-1 illustrates FHT of the as-prepared Si-NP/PVDF (60/40 wt%) electrode on copper foil, in addition to the impact on electrode structure. The FHT process is detailed within the experimental section and briefly involves moving the electrodes through a high temperature furnace purged with a mixture of $\text{Ar}_{(g)}$ and $\text{H}_{2(g)}$, at a constant rate. The high ramp results in carbonization of the polymer matrix starting at $\sim 450^\circ\text{C}$ (Thermal gravimetric Analysis (TGA), **Figure 5-2**), also determined by the visual change in color of the electrodes from a light brown to black. For practical manufacturing consideration, after FHT the Si content within the electrodes increased to 87.2 wt% and no deflagration of the electrode occurred. The electrode materials prepared by FHT result in an electrode structure with good adherence to the current collector and with excellent flexibility (not brittle). This is clearly demonstrated in Figure 6-3, whereby we subjected one of the FHT electrodes to bending. No rupture or microcrack formation arising from the tensile stress was observed. This flexibility was attributed to the polymer carbonization leading to an interconnected carbon network with a coherent, intact structure.

This is supported by a recent study by Chen et al¹⁵¹, whereby they obtained an elastic carbon foam through carbonization of a polymer for use as flexible electrodes. Raman was used to study the change in chemical structure before and after FHT (**Figure 5-1bc**). As expected, a strong peak centered at 520 cm^{-1} was observed for the non-treated electrode, corresponding to the lattice vibration of crystalline silicon. After FHT, this peak broadens and shifts to slightly lower wave numbers, this is attributed to formation of stresses created by a difference in the thermal expansion coefficient between Si and C¹⁵²⁻¹⁵⁵. This stress is determined to be consistent over a large area by mapping the FWHM of the Silicon peak before and after FHT (insets, **Figures 5-1bc**). In addition, two peaks arise at 283 and 927 cm^{-1} after FHT, which may correspond to the Si-O-Si bending and stretching vibrations of silica on the Si-NP surface, respectively^{156, 157}. Carbonization of the polymer binder is confirmed by the introduction of carbons characteristic D and G band peaks at 1335 cm^{-1} and 1600 cm^{-1} , with an Id/Ig ratio of 0.72. The shape and position of these peaks is explained by structural disorder and defects within the mostly amorphous carbon¹⁵⁸⁻¹⁶⁰. Further, several Raman peaks attributed to polyvinylidene fluoride (PVDF) before treatment are no longer present after FHT, as evidenced by the disappearance of the F peak in the Energy Dispersive X-ray chart of the treated electrode (EDX, **Figure 5-5**).

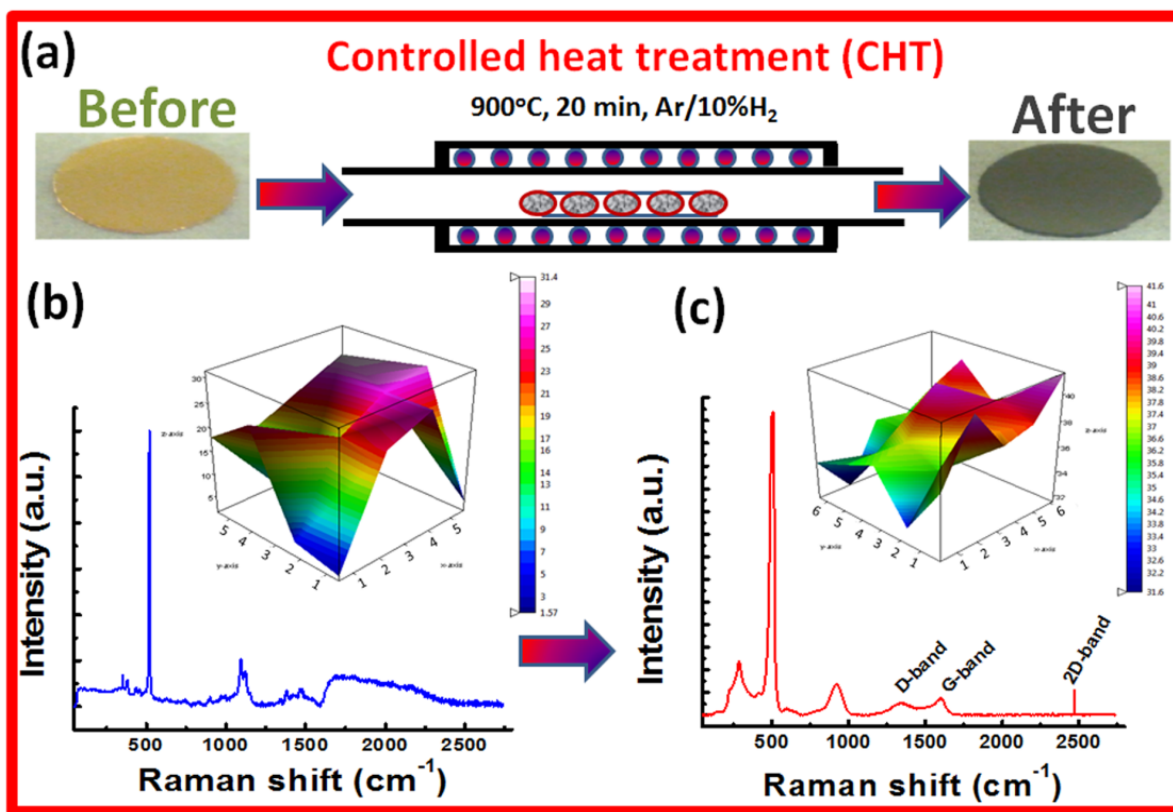


Figure 5-1. a) Schematic of the flash heat treatment process (FHT) showing optical micrographs for the electrode surface before and after FHT and the Raman spectrum for the electrode surface both, b) before FHT and c) after FHT. The insets in (b) and (c) correspond to Raman mapping of the FWHM of the Si peak.

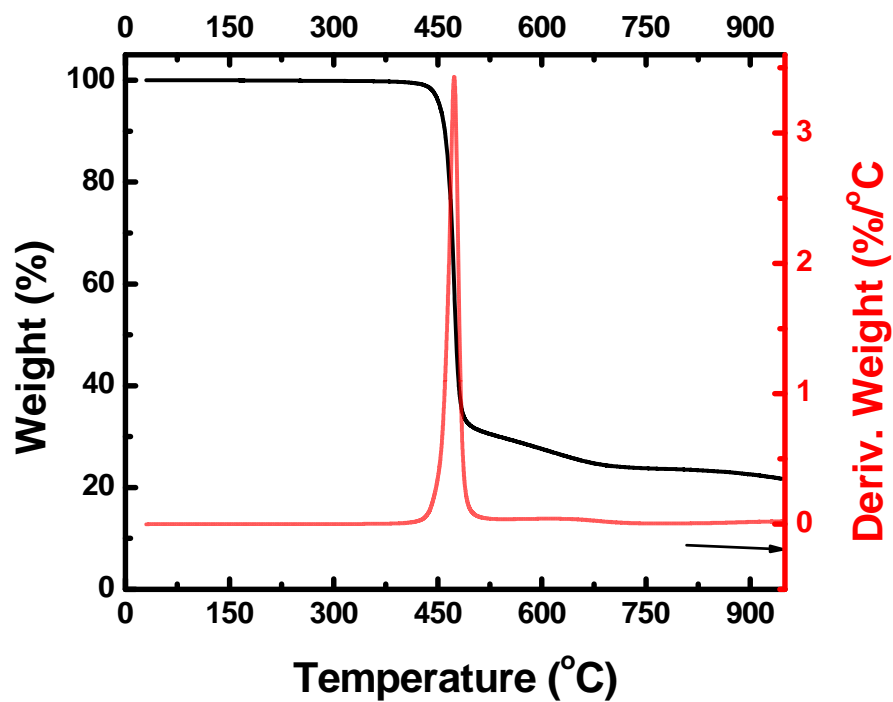


Figure 5-2. TGA for PVDF under nitrogen atmosphere.

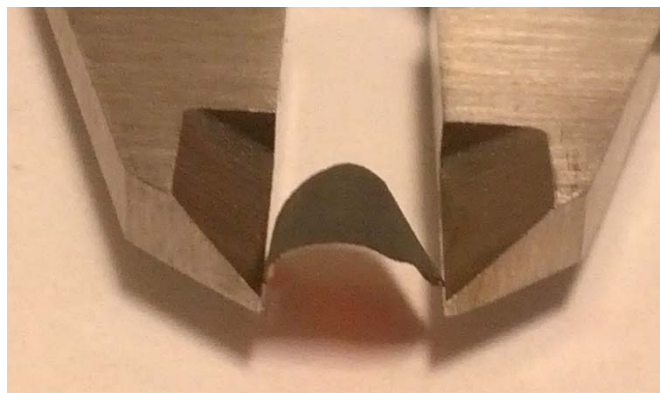


Figure 5-3. Optical micrograph showing the electrode after flash heat treatment (FHT), the electrode material sticks tightly to the copper surface such that bending does not cause exfoliation. This reveals sufficient mechanical stability to sustain handling during cell fabrication.

XRD patterns in **Figure 5-4** show the analysis for the electrode surface after FHT (**Figure 5-4a**) along with the reference peaks of silicon, copper, and copper silicide. The presence of copper silicide is not un-expected after heating both Si and Cu at 900°C¹⁶¹. However, shielding of the SiNP by carbon should minimize the formation of copper silicide, as judged by the very small peak at a d-spacing of 2.46 Å. We believe this only occurs at the current collector interface and that it also may contribute to the good adherence of the electrode coating. Experimentally we obtained a charge capacity equivalent to almost 84% of silicon's theoretical maximum (see later), indicating minimal consumption of Si in side reactions during the FHT process. Inspecting **Figures 5-2 a and b**, it is interesting to note the phase orientation of Si created by the FHT process. The (111) peak of Si becomes inhibited and other Si peaks such as (331) were enhanced. In a similar finding, this peak shift was found to be associated with HF etching of Si¹⁶². Schematic of the electrode cross section is shown in **Figure 5-5 a-b**. Topography of the electrode surface before and after FHT is shown by SEM imaging in Figure 5-5 c-e, and EDX shown in the inset reveal the disappearance of the fluorine peak. This is a sign for fully carbonization of PVDF.

Investigation of the Si-NP surface structure and morphology after FHT is represented by high resolution TEM and Electron Energy-Loss Spectroscopy (EELS) analysis in **Figure 5-6**. The dispersed particles remain interconnected by the carbonized PVDF matrix and reveal an amorphous ~10 nm carbon shell around Si, illustrated by **Figure 5-6a-c**. Electron diffraction of a large area (SAED, **Figure 5-6d**) confirms that Si remains crystalline after FHT. A native SiO₂ layer is expected on the as-received Si surface,^{129, 163} however there is no clear separation between the amorphous SiO₂ and carbon coatings. In order to accurately map the atomic contributions, EELS (**Figure 5-6f**), <1 nm spatial resolution¹⁶⁴, was performed across a particles diameter (**Figure 5-6e**, red line). Overlap of the O and C content within the coating suggests that the FHT process forms an entangled coating of SiO₂ and carbon. A similar confirmatory result is found from the EDX line scan available in **Figure 5-7**. This phenomenon

is likely described by the decomposition of the PVDF matrix, releasing traces of HF which are consumed locally due to the partial etching SiO_2 ¹⁴⁸⁻¹⁵⁰. It is suspected that this etching regulates the formation of porous SiO_2 ¹⁶⁵⁻¹⁶⁸ and allows carbon to deposit within the surface cavities created. Practically, the combined SiO_2 and C coating may have a synergistic effect, the higher surface area anchoring the carbon shell and increasing both electrical and ionic conductivity through the SiO_2 layer. In addition, upon cycling the SiO_2 should interact with Li^+ forming a stable $\text{Li}_2\text{Si}_2\text{O}_5$ phase, reported to effectively reduce Si volume expansion^{146, 147}.

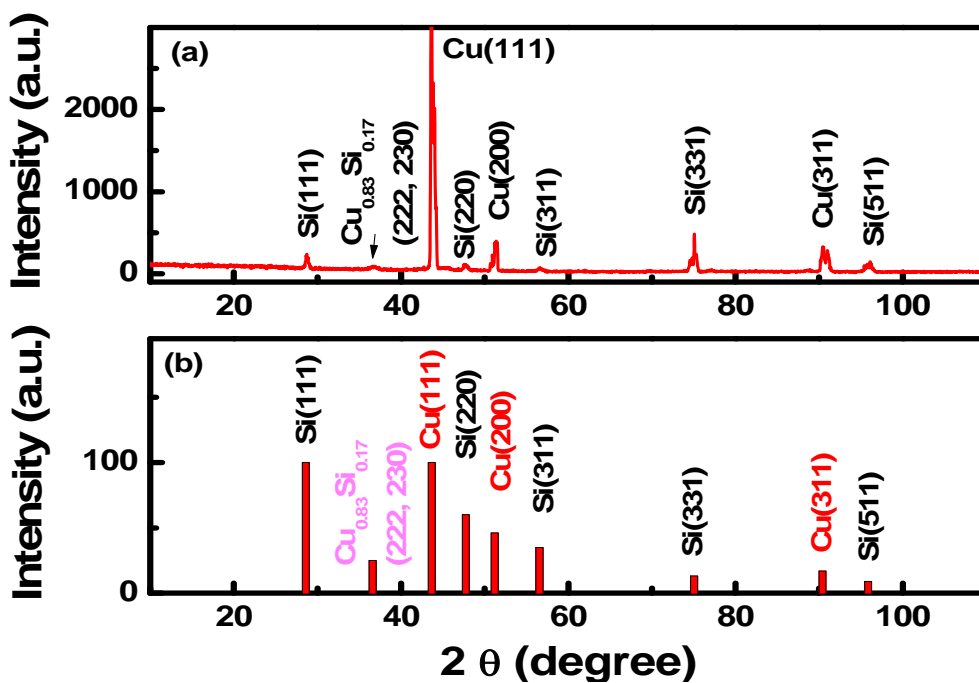


Figure 5-4. (a) XRD pattern for the electrode surface after FHT and (b) shows the reference peaks of silicon (JCPDS 5-0565), copper (JCPDS 4-0836), and copper silicide (JCPDS 23-0223).

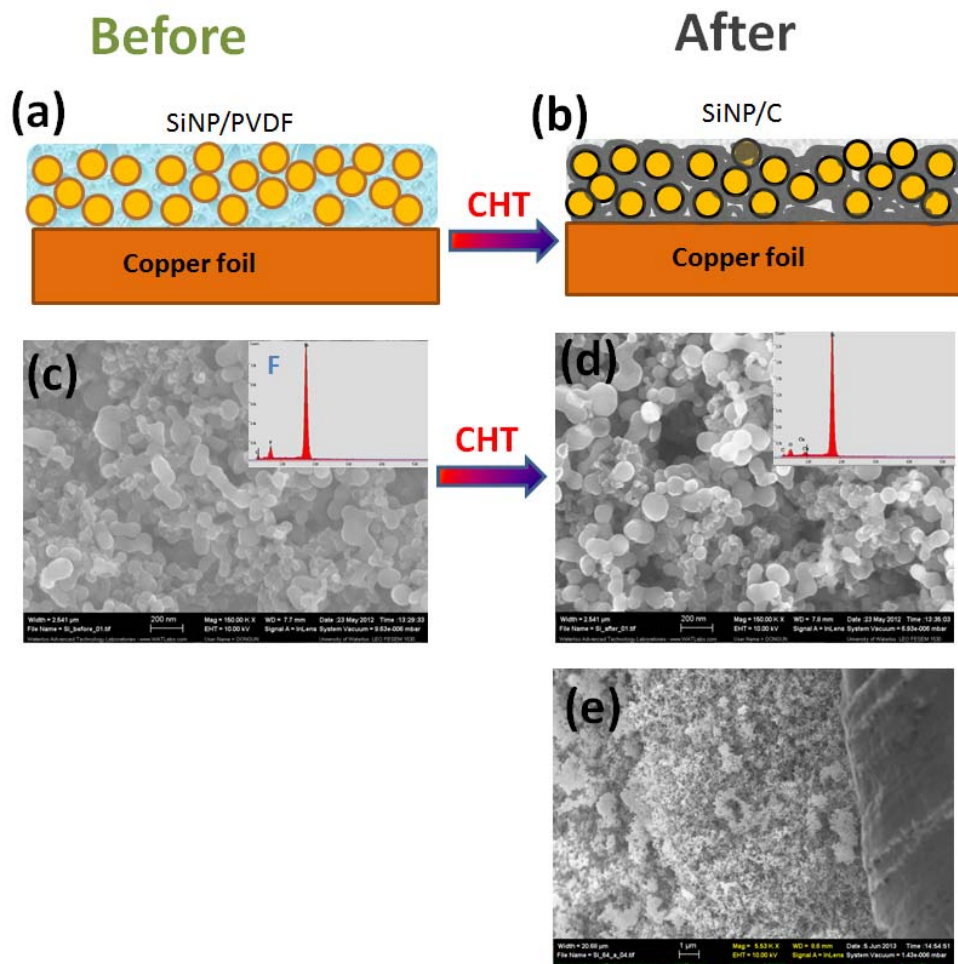


Figure 5-5. (a-b), Schematic of the electrode surface before and after FHT. (c-d), SEM micrographs for the electrode surface before and after FHT treatment, the insets of both figures show the EDS elemental analysis indicating carbonization by disappearance of fluoride peak, (e) is a SEM cross section of the electrode in (d).

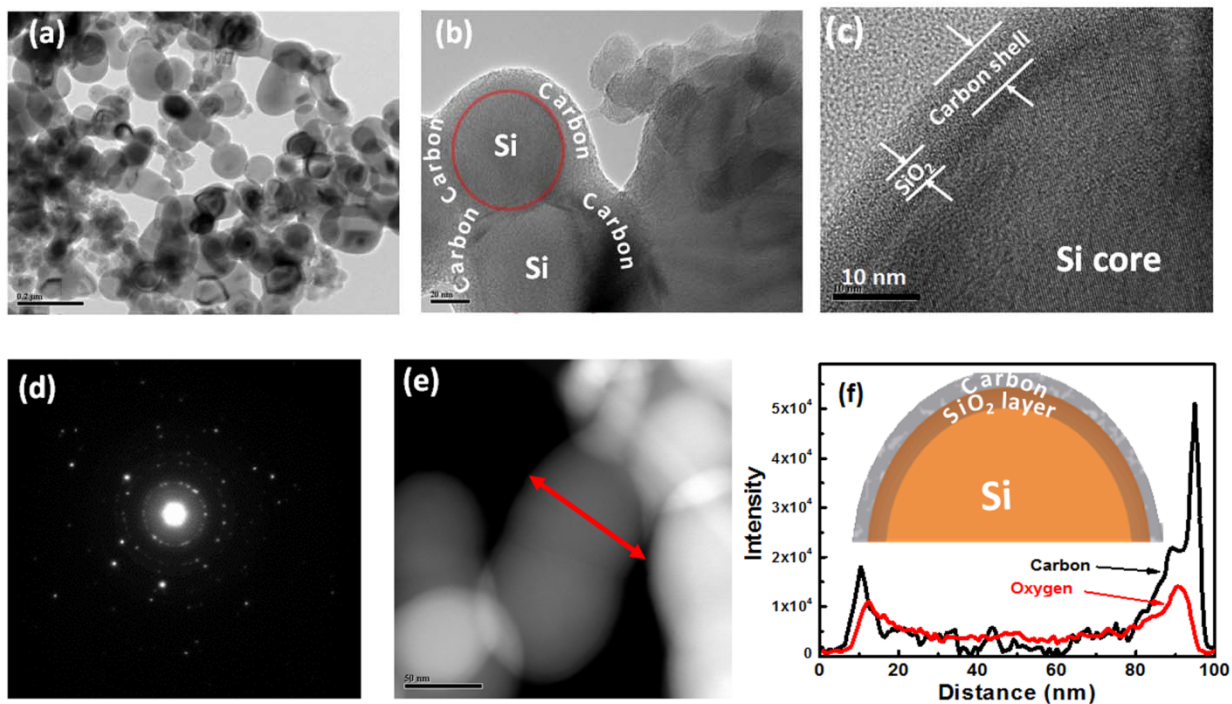


Figure 5-6. a) Low magnification TEM image of the electrode surface after FHT. b) Higher magnification TEM image zooming to a small area of (a), c) HRTEM image across the edge of one Si particle, d) Selected electron diffraction (SAED) taken from a large area of the electrode surface, e) a HAADF-STEM image of a few silicon particles on the electrode surface with carbon coating and f) Electron energy loss spectroscopy (EELS) profile analysis across the particle labeled in (e), the inset in (f) is a schematic depicting the core silicon and the shells of SiO₂ and carbon layer.

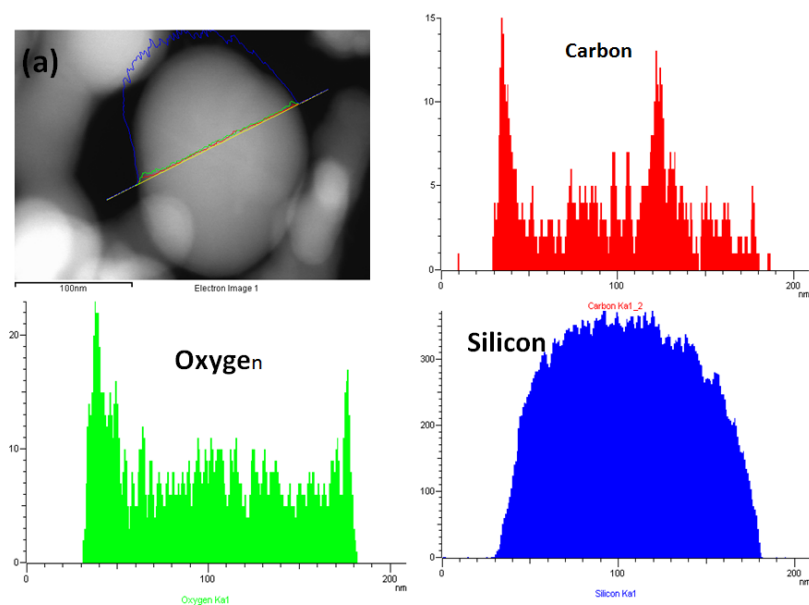


Figure 5-7. (a) HAADF-STEM across a Si-NP from the FHT-treated electrode and its associated EDS elemental line scan across the particle as marked in (a).

5.3.2 Electrochemical Performance

The electrochemical performance of the treated electrode at low current (0.1 A g^{-1}) and a voltage range of 1.5 to 0.005 V is shown in **Figure 5-8**. It reveals that the FHT treated Si electrode achieves a first cycle efficiency of $\sim 84\%$ and a maximum charge capacity of 3525 mA h g^{-1} which is almost 84% of the maximum theoretical capacity of silicon. **Figure 5-9** shows the electrochemical performance characterization of the FHT treated electrodes after assembling them into coin cells, using lithium metal as the counter electrode. Cells depicting the voltage profile and durability in **Figures 5-9a-b** were initially cycled at 0.12 A g^{-1} from 1 - 0.05 V for 5 cycles, before shifting to a moderately high rate of 1.2 A g^{-1} for long-term testing. First cycle charge and discharge capacities of the coin cells made using

the FHT process were 2505 and 1955 mA h g⁻¹ respectively, which corresponds to 78% columbic efficiency. The stability of the electrode structure led to reversible discharge capacity of 2240 mA h g⁻¹ (1806 mA h cm⁻³) after 5 cycles at 0.12 A g⁻¹ and stable capacity of 1350 mA h g⁻¹ after switching to 1.2 A g⁻¹. The effectiveness of the SiO₂/C shell and cellular carbon matrix holding the electrode together is made apparent by the retention of 1150 mA h g⁻¹ after 500 cycles, with 99.8% cyclic efficiency. Further, **Figures 5-9 d-e** illustrate the voltage profile of the FHT treated electrodes in response to varying discharge/charge rates, even at a high rate of 2.5 A g⁻¹ the cells began to stabilize after only 10 cycles. This is in sharp contrast to the untreated electrodes (60:20:20 wt%, Si:PVDF:Super-P), which degraded rapidly, retaining only 13.5% of its charge capacity after only 20 cycles at 0.1 A g⁻¹ (**Figure 5-10**). The improvements for the electrodes subjected to FHT are attributed to improved interfacial contact between the Si and carbon, along with good electronic conductivity throughout the electrode. To further elucidate lithiation/delithiation stability, cells made with treated electrodes were subjected to both Cyclic Voltammetry (CV, **Figure 5-9c**) and Electrochemical Impedance Spectroscopy (EIS, **Figure 5-9f**). Inspection of the first cycle CV for the treated Si electrode reveals that, in the cathodic branch the peak starting at ~ 0.15 V corresponds to the conversion of the Si to the Li_xSi phase. The two peaks at ~ 0.32 and 0.51 in the anodic branch corresponds to delithiation of the Li_xSi phase to Si. After further cycles, an additional broad peak at ~ 0.20 V appears during the cathodic scan and the anodic peaks at ~ 0.32 and 0.51 V become broader and stronger, which is a common characteristic for the transition from crystalline silicon to amorphous silicon due to lithiation/delithiation^{73, 169-171}. The increasing CV curve area is due to initial activation of the material, enabling more Li to react with Si, which is consistent with both the findings of others^{73, 172} and our results introduced in **Figure 5-9a,b**. Stability of the electrodes macrostructure is supported by results of the EIS spectrum taken from cells after discharge cycles 15, 30 and 100, respectively. Extrapolation of the curves semi-circular regime reveals that the real charge transfer resistance decreases from 65 Ω after only 15 cycles, to 37 Ω upon

completion of 100 cycles. The lower values of ESR reveal that the FHT process renders the electrodes with sufficient conductivity and further confirm the perceived stability of the electrode matrix and the SiO₂/C coating created by the FHT process during electrochemical cycling. The alloying reaction with Si is able to occur more quickly after long-term cell conditioning and the ESR improvement strongly suggests stability of the electron and ion pathways which could otherwise impede charge transfer.

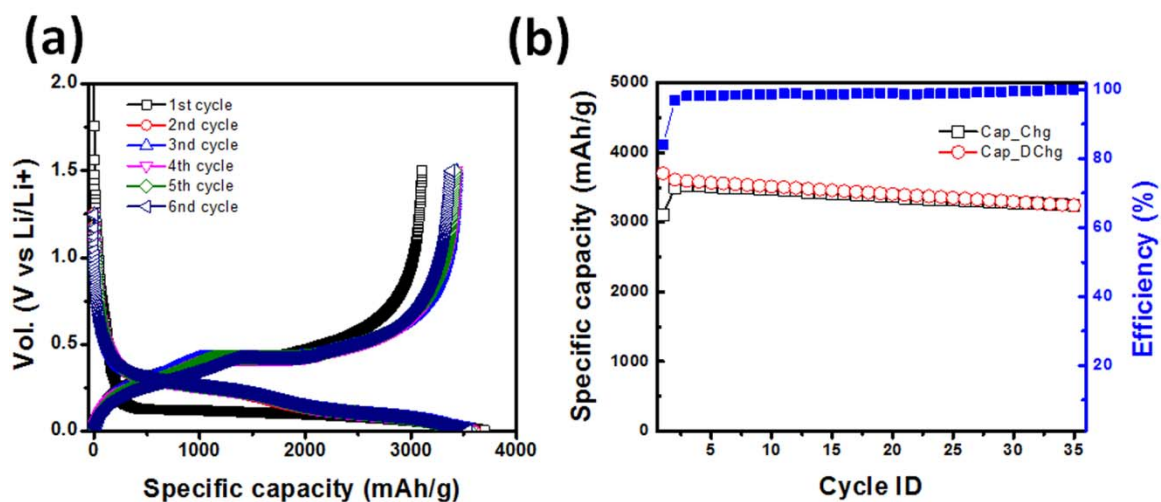


Figure 5-8. (a) Galvanostatic voltage profile at 0.1 A/g with cut off voltage of 1.5 to 0.005 V for a coin cell fabricated using an electrode subjected to FHT , (b) the corresponding cycle capability at 0.1 A/g. (the first cycle efficiency is ~84%).

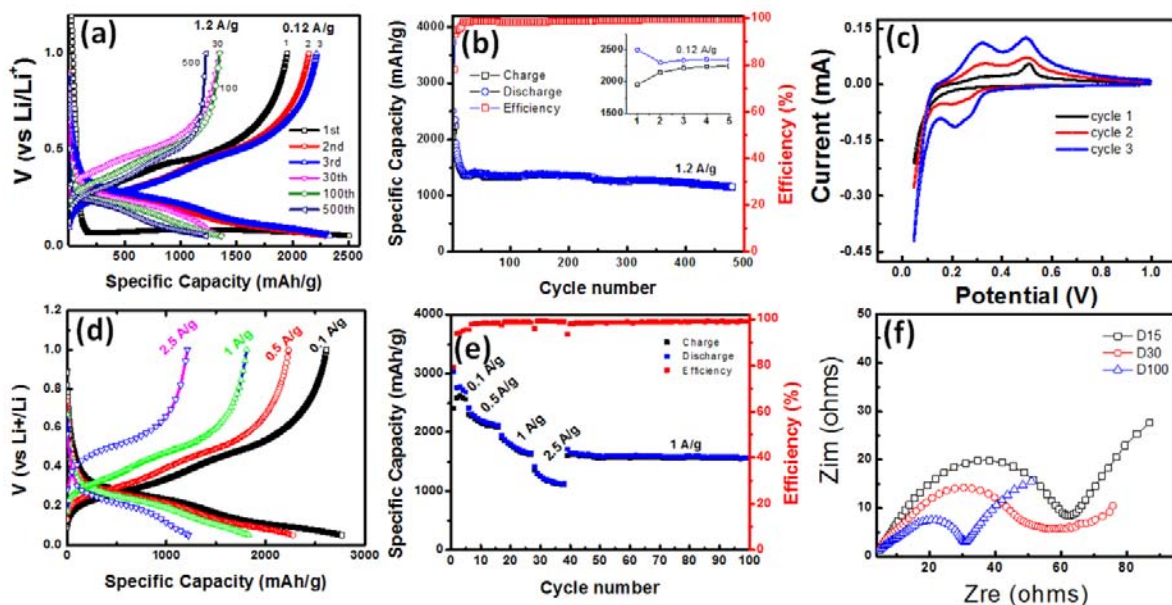


Figure 5-9. (a) Galvanostatic voltage profile showing cycle 1-3 at 0.12 A g^{-1} and cycles 30, 100 and 500 at 1.2 A g^{-1} , (b) Cycle capability for the cell shown in (a), (c) Cyclic voltammogram for a coin cell measured at scan rate of 0.05 mV s^{-1} between 1.0 and 0.05 V (vs Li^+/Li), (d) Galvanostatic voltage profile at different rates, (e) Cycle performance showing the rate capability, and (f) EIS for the coin cell after discharge of the cycles 15, 30 and 100.

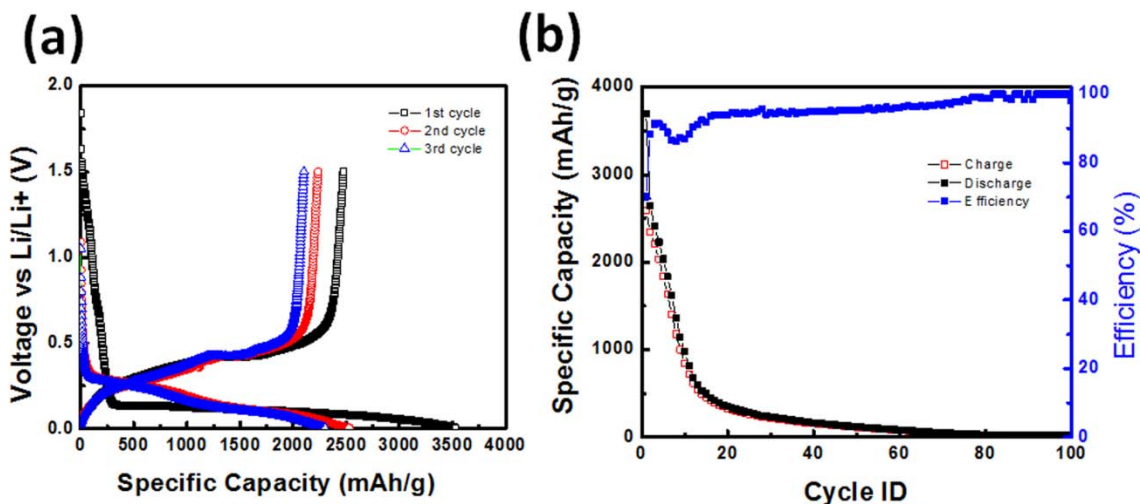


Figure 5-10. (a) Galvanostatic voltage profile at 0.1 A/g with cut off voltage of 1.5 to 0.005 V for a coin cell fabricated using electrode with 6:2:2 ratio of SiNP: Carbon : PVDF without subjecting the

electrode to FHT, (b) the corresponding cycle capability of the non-treated electrode cycled at 0.1 A/g. (the first cycle efficiency is ~70%).

After the completion of long term electrochemical cycling using the FHT processed electrodes, the coin cell was opened to facilitate further investigation of changes to the surface morphology using HAADF-STEM (**Figure 5-11a-e**). This figure shows that after 500 cycles the formed amorphous silicon is caged in a sponge-like carbon that persists against expansion and contraction during lithiation/delithiation even after this long cycling. A large area EDX scan reveals the positional mapping of the Si and C distribution (Figure 5c and d, respectively). High resolution of a single representative Si particle suggests the amorphous SiO₂/carbon coating remains in strong contact with the carbon shell. In addition to the stable particle coating, **Figure 5-11f** depicts by TEM the detection of graphene-like sheets taken from the electrodes after cycling. The existence of graphene within the treated electrode is supported by literature revealing carbon diffusion into copper can catalyze the formation of monolayer graphene adsorption at high temperatures¹⁷³⁻¹⁷⁸. This suggests that the graphene sheets are assumed to exist on the current collector surface. Further, TEM analysis depicted in **Figure 5-12** confirms graphene sheets are indeed forming during the FHT processing of a copper electrode coated with only PVDF. These results verify that the FHT process is also able to successfully alter the current collector/electrode interface, potentially enhancing electrode stability.

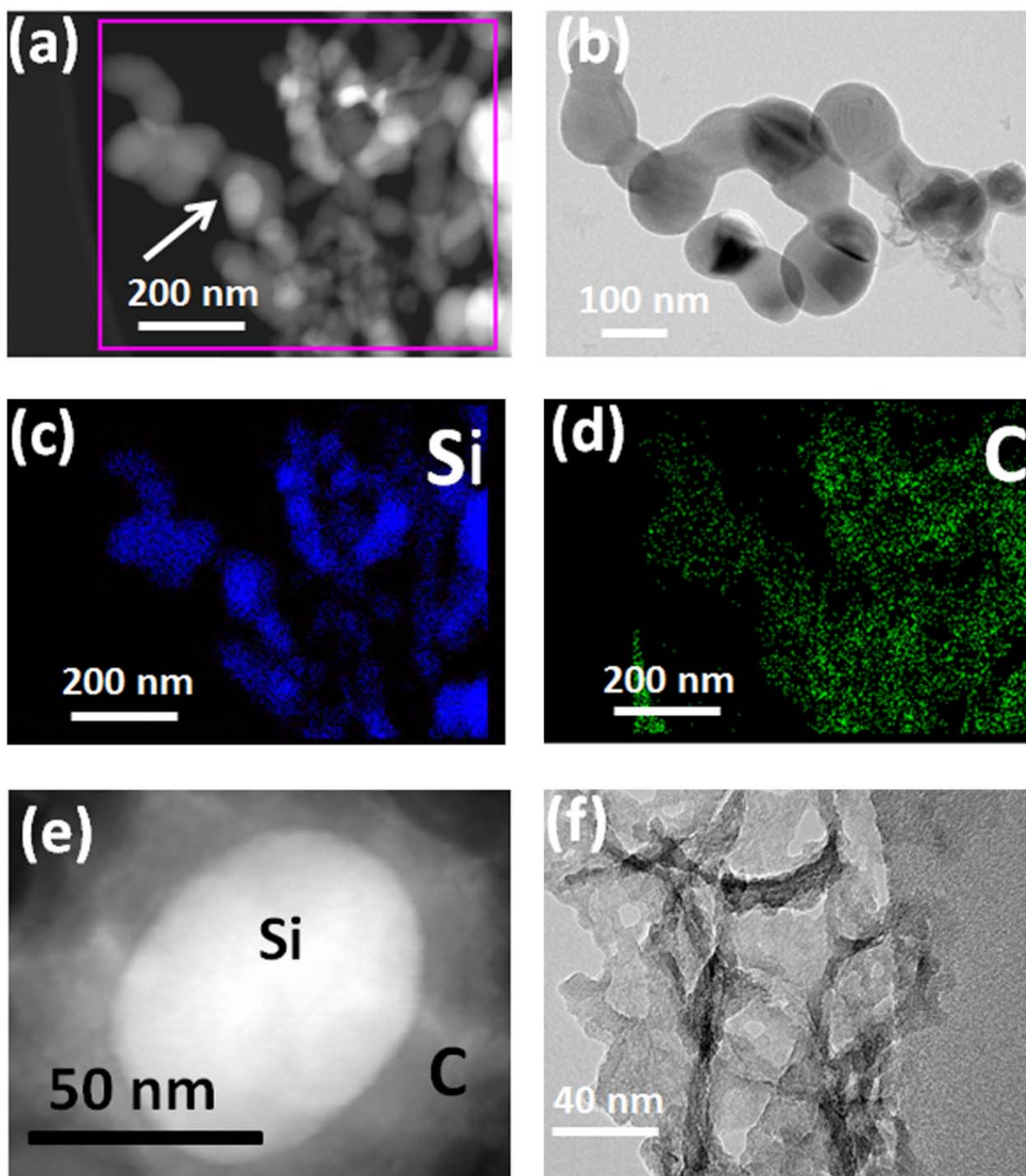


Figure 5-11. a) High-Angle Annular Dark field Scanning Transmission Electron micrograph (HAADF-STEM) of the electrode surface after being cycled for 500 cycles of charge/discharge, b) TEM image showing a few Si particles included in their carbon cage and interconnecting even after 500 cycles, c and d) EDS elemental mapping of Si, and C for the area selected in image a. e) HAADF-STEM zoomed in to a silicon particle as labeled in (a). (f) TEM micrograph for part of the electrode surface after cycling.

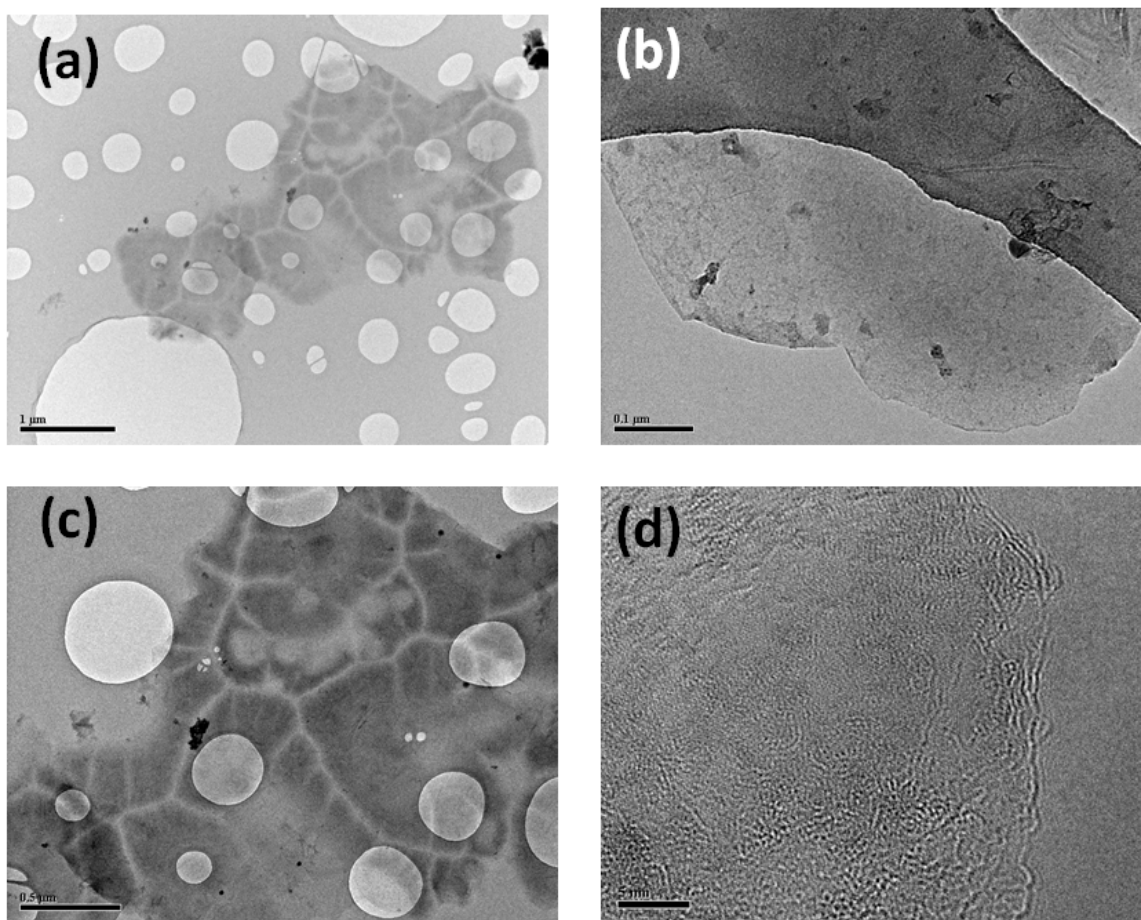


Figure 5-12. (a-b) TEM images for different areas for graphene nanosheets prepared by spreading a thin film of PVDF on copper foil followed by FHT treatment, (d) HRTEM for an edge of the graphene sheet.

Chapter 6 Covalent binding of Si to S-doped graphene

The following section is based on published manuscript prepared by Hassan, F. M. et al,

Fathy M Hassan, et al . “Covalent synergy of silicon-sulfur-graphene as peculiar material design for cutting-edge lithium-ion battery”, to be submitted to *Nature Materials*. Manuscript #NM14123597 , Submitted on December 9, 2014.

Also these results were submitted as part of a patent application:

F. M. Hassan, Z. Chen, Xingcheng Xiao, US provisional patent “A process of making nano-hybrid sulfur-doped graphene/silicon composites and using as electrodes for lithium batteries”, filed on October, 2014 by General Motors, US , P030743.

6.1 Introduction

The widespread market success of high performance portable electronics and hybrid (or electric) vehicles strongly depends on further technological progress of commercially available rechargeable batteries¹⁷⁹. Lithium ion batteries (LIBs) are considered the most likely energy storage configuration to satisfy these demands,^{180, 181} however require significant advances in terms of power density, energy density, cycle life, and safety, as well as lower production costs. Current LIB systems utilize graphite anodes, where energy is stored by intercalating lithium into the graphite layers. This arrangement, while commercially successful, can only deliver a maximum theoretical capacity of 370 mAh g⁻¹.¹⁸² Incorporating additional components offers the potential to dramatically improve this capacity, whereby silicon can provide up to 4,200 mAh g⁻¹ in theory. While Si-based composites offer immense promise as new generation anode materials, extreme changes in volume during lithiation and delithiation lead to structural degradation and debilitating performance loss over time that impedes their practical application.^{32, 75, 126, 182-190}

Significant efforts have been devoted to tackling these problems by engineering Si-based electrodes at the nanoscale.^{79, 145, 183, 191, 192} For example, silicon nanoparticles (SiNP) were embedded in a carbon matrix through a multistep process to create nanosized void spaces for accommodating volume changes during lithiation/delithiation.² Mesoporous silicon sponges have also been prepared by electrochemical etching of B-doped Si wafers, which were used to minimize the pulverization of silicon. With an additional carbon coating, these materials delivered a capacity of 500 mAh g⁻¹ for 1000 cycles (at a rate of 1 A g⁻¹, and an areal capacity of ca. 1.5 mAh cm⁻²).³ Another promising method involved *in-situ* polymerization of a conducting hydrogel to coat the SiNP, providing porous space for the large volume expansions.⁵ In order to further improve the performance at a high active material electrode loading, the same group proposed another novel electrode design concept, utilizing silicon nanostructures analogous to pomegranates to stabilize the solid electrolyte interphase and to provide stable cycling up to 1000 cycles.¹⁹³

Instead of designing fancy Si nanostructures, herein we introduce a new electrode design concept that capitalizes on the strong covalent interactions occurring between Si and sulfur. This involves wrapping SiNP with S-doped graphene (SG), and then shielding this composite arrangement with cyclized polyacrylonitrile (PAN). We first disperse SG in dimethylformamide (DMF) by ultra-sonication, and then mix it with commercially available SiNP. After that, we add a solution of PAN in DMF to the Si-SG mixture, and ultrasonicate them together to make a homogenous slurry. The obtained slurry is directly cast on a Cu current collector and then subjected to a sluggish heat treatment (SHT), which we use to refer to a 10 min heat treatment under inert gas at 450°C, using a heat up and cool down time of 2 hrs. Using this overall procedure, we avoid any sophisticated and tedious synthesis processes to prepare nanostructured silicon composites, while at the same time enabling a high electrode loading of the active material for practical applications.

6.2 Results and Discussions

6.2.1 Characterization of the electrode materials

Figure 6.1 a and **b** schematically illustrate the fabrication process and the structure of the composite at the nanoscale, along with optical images of the electrode before and after SHT, respectively. The high angle annular dark field (HAADF) scanning transmission electron microscope (STEM) image in **Figure 6.1 c** shows that SG wraps the SiNP, which are invariably dispersed within the nanosheets matrix. The TEM image in **Figure 6.1 d** (along with the high resolution TEM images in **Figure 6.1 e** and **f** of an individual SiNP) reveal that amorphous carbon (from PAN) forms a shell around the SiNP with a thickness of ca. 5 nm. The crystallinity of the SiNP can also be verified by the HRTEM image shown in **Figure 6.1 f** and the corresponding FFT pattern shown as the inset.

It is well established that sluggish heating can cyclize PAN, whereby cyclized PAN can provide stabilization of electrode structures.^{194, 195} The characteristic exothermic peak for PAN cyclization is shown by differential scanning calorimetry (DSC) in **Figure S1a (Appendix I)**, with the results consistent with previous reports.^{196, 197} Upon treatment, PAN loses about 20% of its mass as shown by TGA, with results provided in **Figure S1b (Appendix I)**. After cyclization, PAN has a π -conjugate structure that is believed to lower the electronic and charge transfer resistances of the electrode, as evidenced by the electrochemical impedance spectroscopy shown in **Figure S2 (Appendix I)**. The cyclized PAN (c-PAN) forms an effective shielding around the SiNP, which are already anchored on SG through covalent interactions as confirmed by DFT calculations discussed *vide infra*. In addition, c-PAN sticks between the SG nanosheets, providing a 3-D dimensional, interconnected structure that enables enhanced conductivity and material robustness, as shown schematically in **Figure 6.1b**. Inspecting the HRTEM images introduced in **Figure 6.1** and the EDX mapping in **Figure S3 (Appendix**

D), it can be proposed that every SiNP is caged in a carbon shell of c-PAN. It is also clearly observed that there is no agglomeration of SiNP.

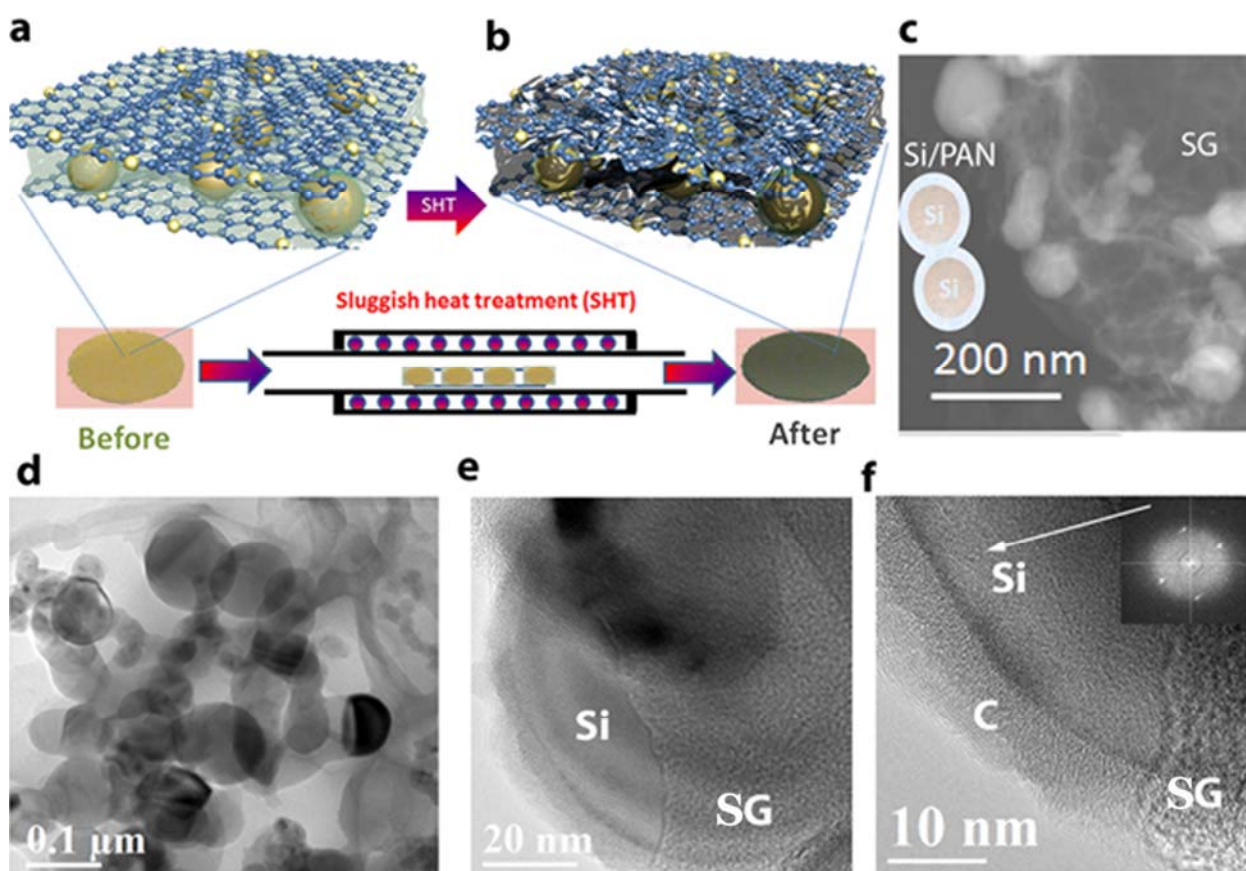


Figure 6-1. Schematic of sluggish heat treatment. a) an optical image of the as-fabricated electrode made of SiNP, SG and PAN, b) the electrode after SHT, c) HAADF-STEM image and d) TEM image of the SG-Si electrode, e, f) HRTEM images zooming in on a SiNP in the SG-Si electrode, and (f, inset) FFT pattern of the SiNP.

The elemental analysis after SHT determined by the XPS survey spectrum from the SG-Si electrode is shown in **Figure 6.2a**, confirming the existence of Si, S, C, N and O. **Figure 6.2b** shows the core-level

spectra of S in both pure SG and in the SG-Si electrode. In pure SG, the S_{2p} doublet corresponding to the sulfide (C-S-C) structure is observed at 164.0 and 165.2 eV and labeled (1) and (2). These peak locations are in good agreement with the reported $S_{2p_{3/2}}$ and $S_{2p_{1/2}}$ spin orbit couplet¹⁹⁸⁻²⁰⁰. The other minor peaks labeled as (3) in **Figure 6.2b** and located at higher binding energies are attributed to oxygen bound to sulfur (-SOx).²⁰¹ For SG-Si, the peak corresponding to S gets significantly broader and is shifted to a higher binding energy. We believe that this shift may be an indication of the covalent interaction formed between most of S and Si atoms. It should be noted that a higher binding energy of S (~ 168 eV) was observed when a sulfur-containing organic compound was adsorbed on silicon²⁰², and a similar phenomenon may exist within SG-Si electrode. The core-level spectra in **Figure 6.2 c** shows the typical elemental Si peak (1) located at 99.4 eV, with the minor peaks at higher binding energies (~103.4 eV) related to oxygenated silicon or silicon bonded to sulfur.²⁰³ While the spectra of C in **Figure 6.2 d** shows several common peaks, the first one (1) centered at 284 eV corresponds to sp^2 hybridized graphitic type carbon. Peak (2), centered at 284.6 eV, denotes the presence of sp^3 bonded carbon. Finally, peaks (3) and (4) are characteristic of oxygenated carbon and peak (5) is related to Plasmon loss features.²⁰⁴⁻²⁰⁶ **Figure 6.2 e** displays a high-angle annular dark field scanning transmission electron microscope (HAADF-STEM) image of the SG-Si electrode, while **Figure 6.2 f** displays the corresponding electron energy loss spectroscopy (EELS) image of the highlighted area in image **Figure 6.2 e**. The pixels in the EELS image correspond to 3.4 nm x 3.4 nm each. The yellow color is related to Si, while the red color is sulfur (mixed red and yellow give orange with different degrees relative to the concentration). It can be inferred that sulfur follows the circumference of the SiNP. The corresponding spectrum of the EELS based elemental mapping is shown in **Figure S4(Appendix I)**. It again confirms the presence of Si, S, N and C, whereby S comes from the SG and N from the cyclized PAN. Raman spectra of PAN films before and after SHT is shown in **Figure 6.2 g**. While no features appear before SHT, two characteristic peaks at $\sim 1346\text{cm}^{-1}$ and $\sim 1605\text{cm}^{-1}$ are observed after SHT.

These peaks correspond to the “D” and “G” bands from the structural defects and disorder from sp^3 -carbon atoms and the plane vibration of the sp^2 -carbon atoms in two-dimensional lattice of the cyclized PAN, respectively. The same features appeared with the electrode materials after subjecting them to SHT, **Figure 6.2 h**.

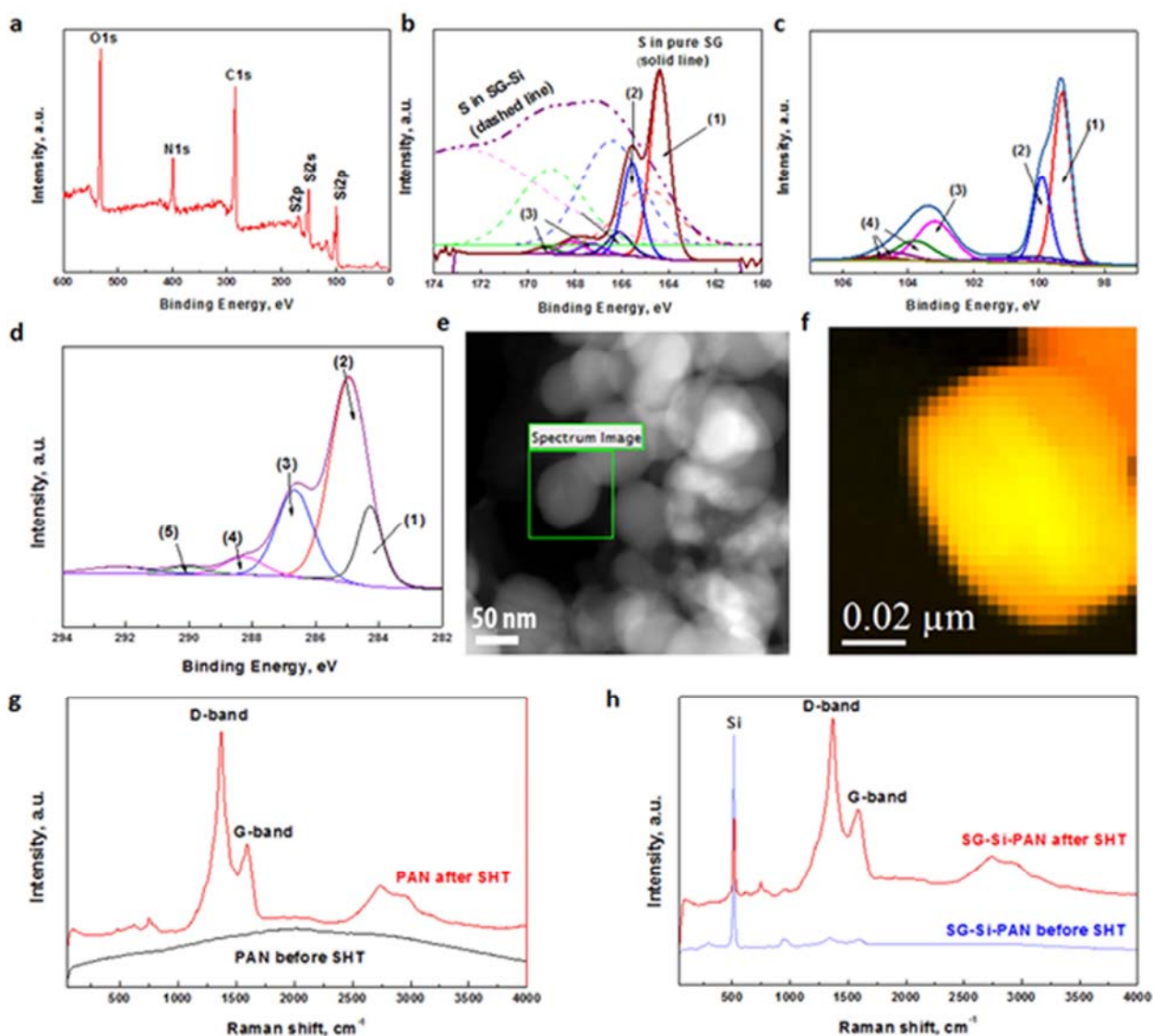


Figure 6-2. Electrode material characterization for SG-Si. a), XPS survey spectra confirming the elements Si, S, C, N and O, b) High-resolution XPS spectra of S in pure SG, and in SG-Si, c) High resolution XPS of Si 2p in SG-Si, d) High-resolution XPS spectra of C in SG-Si, e) HAADF-STEM

image of SG-Si, and f) EELS mapping of the elements Si (yellow) and S (red), with each pixel in Figs d-f representing 3.4 x 3.4 nm, g) Raman spectra for PAN film on copper before and after SHT, h) Raman spectra for SG-Si-PAN electrode surface before and after SHT.

6.2.2 Electrochemical performance

Figure 6.3a presents the typical galvanostatic charge/discharge profiles of the SG-Si based electrode tested at 0.1 A g⁻¹ between 1.5 and 0.05 V. The observed plateau in the first discharge curve represents alloying of crystalline silicon with lithium.^{145, 207} The SG-Si delivers an initial discharge capacity of 2865 mAh g⁻¹, based on all masses of SG, c-PAN and Si, with a high first cycle Coulombic efficiency of 86.2%. If not mentioned, all reported capacities are based on the total mass of SG, c-PAN and Si. The voltage profiles of the subsequent cycles show slightly different behaviour, which is common for the lithiation process of amorphous Si formed during the first cycle. It is noteworthy that the areal charge capacity is about 3.5 mAh cm⁻², which is close to the performance targets for next generation highly energy dense lithium ion batteries.¹⁹¹ **Figure 6.3 b** shows the cycling stability of the SG-Si at 0.1 A g⁻¹. A stable cyclability up to 100 cycles can be obtained, with an average capacity of 3360 mAh g⁻¹ (~ 3.5 mAh cm⁻²), measured relative to the total mass (Si-SG-PAN). These results compare very favourably to a recently published report¹⁹¹. The charge storage behavior was also characterized by cyclic voltammetry (CV). **Figure 6.3 c** shows the first 5 cycles of the SG-Si electrode in a coin cell at a scan rate of 0.05 mV s⁻¹. In the cathodic scan, there are two distinctive peaks appearing at 0.27 and 0.22 V vs Li/Li⁺, indicating the formation of Li₁₂Si₇ and Li₁₅Si₄ phases, respectively.^{208, 209} In the anodic direction, the corresponding two peaks are located at 0.31 and 0.49 V, representing the dealloying of Li_xSi to Si. All anodic and cathodic peaks become broader and stronger as a result of cycling, which is a common feature attributed to the conversion of Si into an amorphous phase during

lithiation/delithiation. The rate capability of the SG-Si electrode is shown in **Figure 6.3 d**, revealing the excellent kinetics of the SG-Si electrode at different currents up to 4 Ag^{-1} . Moreover, the robust structure enables a very stable cycling, where a capacity of ca. 1033 mAh g^{-1} can be maintained for more than 2200 cycles at a rate of 2 Ag^{-1} . On the other hand, a similar electrode structure prepared by replacing SG with non-doped graphene gives an inferior rate capability and cycling stability, as shown in **Figure 6.3 e**. The high capacity of the G-Si persists only for 65 cycles, then fades gradually, reaching $\sim 200 \text{ mAh g}^{-1}$ after 800 cycles. Such a capacity fading is attributed to the degradation of the Si structure leading to the loss of conductivity and instability in the solid electrolyte interphase (SEI) structure. The significantly different electrochemical performances put a spotlight on the important role of sulfur in binding the SiNP to the surface of SG, which encouraged us to further investigate it using density functional theory (DFT) calculations discussed below. A coin cell made of a SiNP/PAN electrode, fabricated using SiNP and PAN subjected to a SHT, shows poor rate performance. In addition, its cycle stability persist for only 65 cycles and then degrades rapidly to almost zero capacity (**Figure 6.3 f**). These results emphasize the important role of the covalent binding between Si and SG to enable the impressive performance seen in **Figure 6.3 d**.

In order to test the behavior of SG-Si in a realistic full cell setup, a coin cell consisting of a SG-Si anode and a commercial LiCoO_2 cathode was assembled. The cell was first charged from OCV to 4.3 V and then cycled between 2.5 to 4.3 V (**Figure S6 (Appendix I)**). The first cycle efficiency is ca. 84% and the cell was able to give an areal capacity of ca. 3 mAh cm^{-2} at a rate of 0.1 Ag^{-1} with respect to the SG-Si/PAN mass. When the rate increased 10 times to 1 Ag^{-1} , the capacity is decreased to 0.9 mA cm^{-2} or $\sim 800 \text{ mAh g}^{-1}$ (SG-Si), and remains relatively stable with minimum capacity loss for up to 100 cycles. After cycling the coin cell for 2200 cycles (**Figure 6.3 d**), the cell was disassembled and the SG-Si electrode was subjected to further characterization. **Figure 6.4 a** shows a HAADF-STEM image of the

electrode structure and **Figure 6.4 b-d** provide the corresponding colored EELS mapping for the elements S, C, and Si, respectively (each pixel is 3.4 x 3.4 nm). This characterization emphasises the conversion of the electrode materials to a wire-like morphology after cycling. The location of the SiNP is associated with regions of high sulfur and carbon.

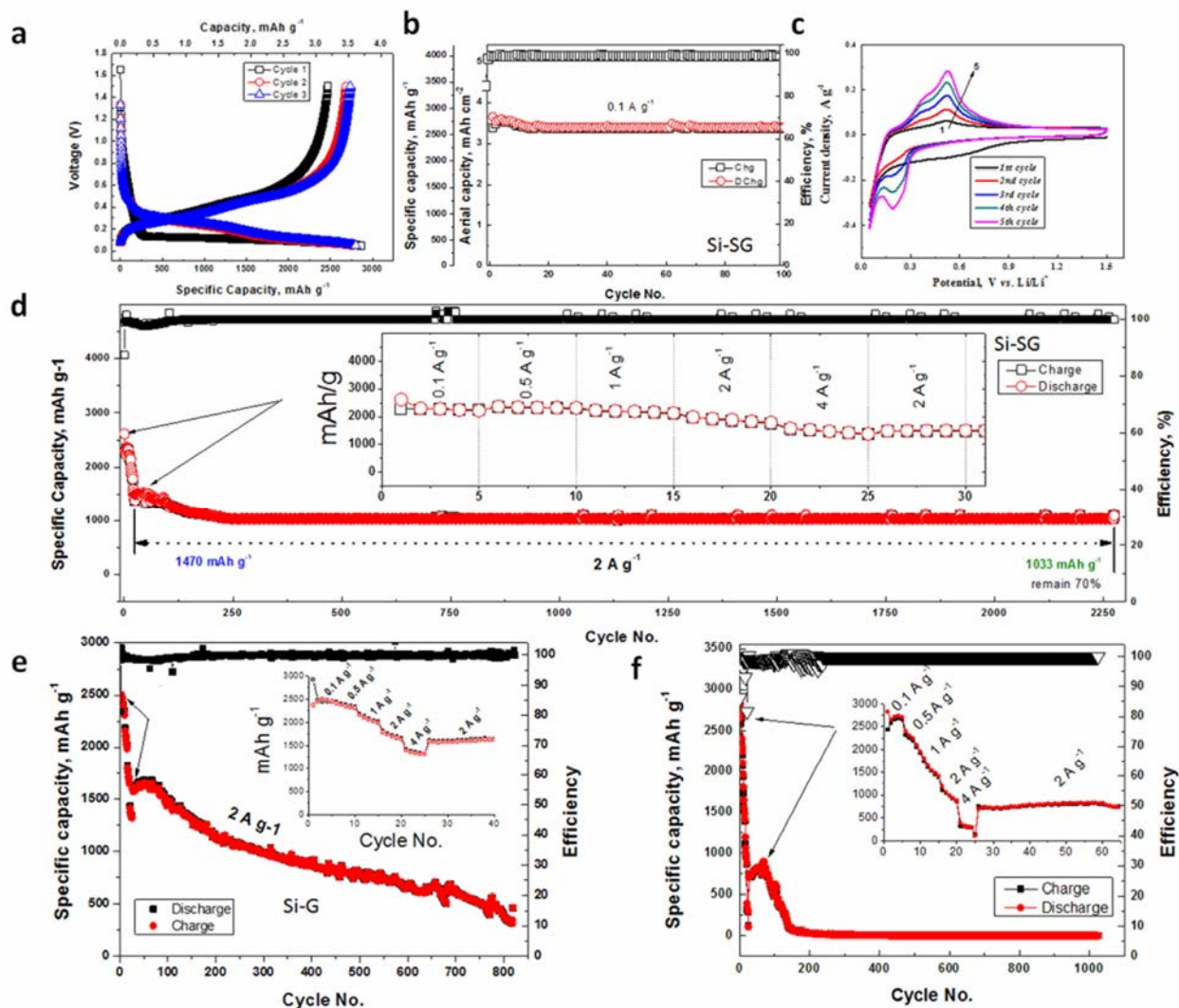


Figure 6-3. Electrochemical performance of SG-Si. a) Voltage profile of SG-Si anode at 0.1 A g⁻¹, b) the corresponding cycle stability, c) cyclic voltammogram curves of the SG-Si coin cell, d) rate capability of SG-Si anode followed by cycle stability at 2 A g⁻¹, e) rate capability of G-Si anode followed by cycle stability, f) rate capability of Si-PAN anode followed by cycle stability.

It can be noted that the SiNP, after 2200 repetitive expansion and contraction cycles, fractured and pulverized into smaller particles. However, those fractured Si particles are still confined within the continuous channels of the c-PAN shell, which is overlaid on SG and maintains the electrical connection between Si and graphene. Furthermore, the graphene layer prevents the direct contact of the electrolyte to Si. As a result, the fractured Si will not induce new SEI formation. Most of the SEI layer forms only on the outer surface of graphene, which shows very minimal volume expansion and contraction. The synergy of the interactions among Si/SG/c-PAN leads to very excellent cycle efficiency and capacity retention, as shown in **Figure 6.3 d**.

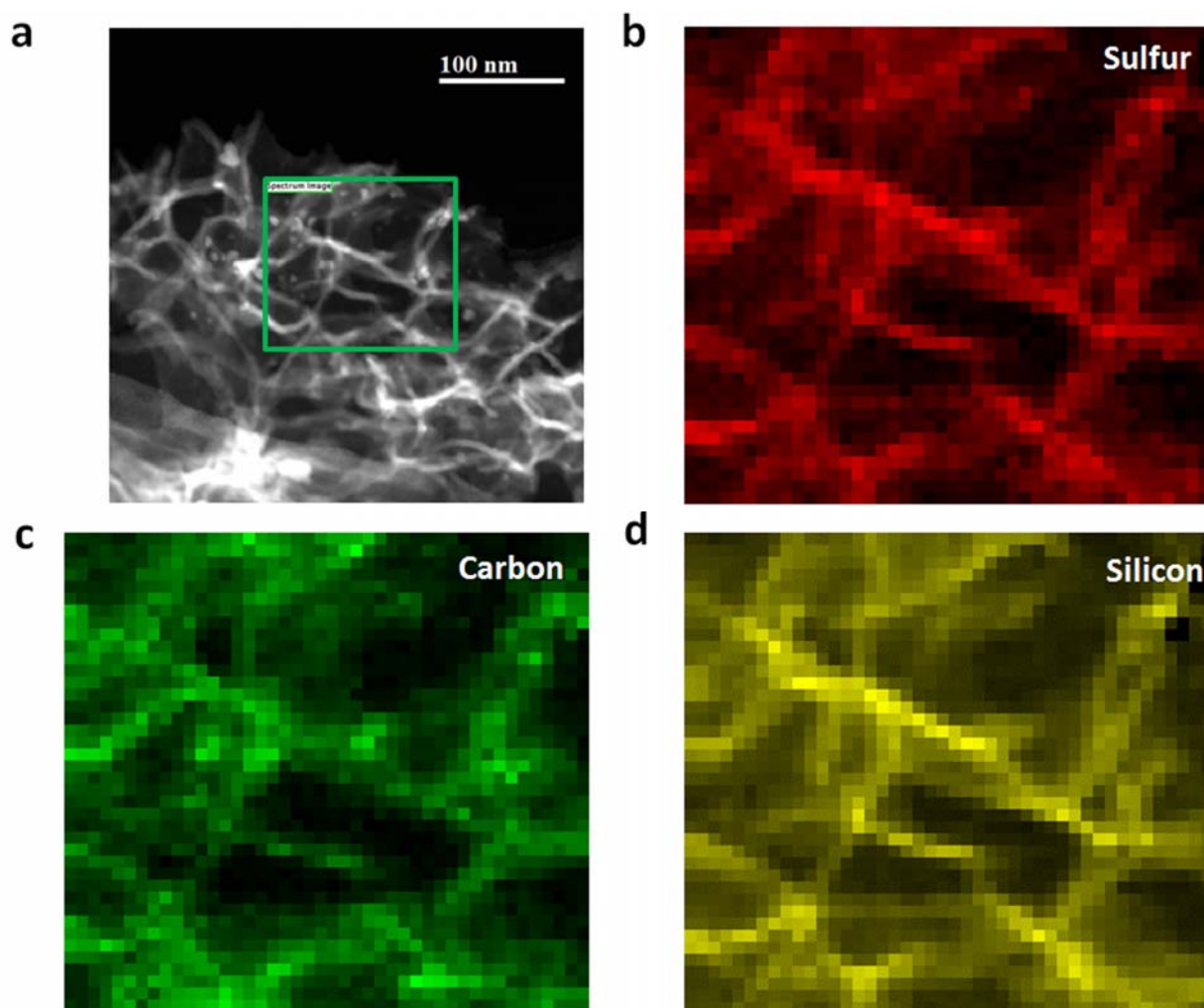


Figure 6-4. Characterization of SG-Si electrode material after cycling for 2400 cycles. a) HAADF-STEM image of the SG-Si electrode after cycling, c-e) the elements mapping by EELS for the area marked in image. N.B. Each pixel in Figs d-f represents 3.4 x 3.4 nm.

6.2.3 Quantum mechanics calculations

In the present study, the graphene surface was modeled using a hydrogenated graphene cluster ($C_{54}H_{18}$), which is also referred as H passivated graphene (see **Figure S8 (Appendix I)**). The optimized bonding distances of C–C (1.42 Å) and C–H (1.09 Å) in this model are in good agreement with that for bulk graphite.²¹⁰ Based on this H passivated $C_{54}H_{18}$ cluster, a structure of sulfur-doped graphene (SG) is proposed. The optimized SG structure with some key structural parameters is shown in **Figure S9 (Appendix I)**. It can be seen that the SG has a distorted configuration. In all the calculations, all the atoms in the cluster were allowed to relax.

In order to describe the interactions between the Si and graphene, the bonding energies (BE) of Si were defined by equation (1):

$$BE = E_{Si-graphene} - E_{graphene} - E_{Si} \quad (6.1)$$

where $E_{Si-graphene}$, E_{Si} , and $E_{graphene}$ represent the energies of the Si-bound to the graphene structure, the Si atom, and the graphene structure, respectively.

Si adsorption on different sites of the SG was studied. The results are compared with those obtained on undoped graphene. **Figure 6.5 a (i)** presents the configuration of the stable Si adsorption on graphene (G-Si), with Si sitting at the bridge site with adsorption energy of 0.45eV. Two stable configurations for Si adsorption on sulfur doped graphene were observed. The first is represented as SG-Si(A), which reveal the bonding of Si to location (A), **Figure 6.5 a (ii)**. The second represents binding to location

(B) and represented as SG-Si(B), **Figure 6.5 a** (iii). In SG-Si(A), Si was found to bind to S and two “saturated” C atoms (C_7 and C_8), with the corresponding binding energy of -2.02 eV. On the other hand, at the second position, SG-Si(B), Si binds to S and two C’s at the defect sites (C_2 and C_3) forming two Si-C and one Si-S bonds, leading to a binding energy of -3.70eV. The higher binding energy in the latter case indicates Si would be more energetically favorable to bind to the defect C_2 and C_3 atoms. Most importantly, the results show that Si attached on SG structure has a much higher binding energy than that on graphene (G-Si). This result introduces a strong explanation for the much longer cycle stability in SG-Si than in G-Si. **Figure 6.5 b** introduces the highest occupied molecular orbital (HOMO) and the lowest unoccupied molecular orbitals (LUMO) for the G, SG, SG-Si(A) and SG-Si(B). The difference between the LUMO and HOMO contribute to band gap of the substance. The respective band gap values are 1.91, 1.14, 0.61 and 0.29 eV for the G, SG, SG-Si(A) and SG-Si(B). This indicates that introducing sulfur to graphene increases its intrinsic conductivity as evidenced by the lower in the band gap. The adsorption of Si to the SG surface further improves the intrinsic conductivity of the support structure indicating a covalent synergy of Si with SG with enhancement of the electron density in the SG matrix.

Hirshfeld charge analysis was also conducted to evaluate the stability of Si on G and SG. The calculated charge distribution before and after the Si adsorption on G and SG are given in **Table S1 (Appendix D)**. The results show that Si has a positive charge after its adsorption on G and SG, which indicates that there are electrons flow from the Si atom to the graphene substrate upon Si adsorption. However, the electron flow is more significant for Si adsorption on SG than that on G, because Si deposited on SG has a larger positive charge than that on G. This may be a reason for the positive shift of binding energy of sulfur in SG-Si. Table S1 also shows that the C atoms that are bonded with the Si atom in SG-Si, such as C_7 and C_8 in SG-Si(A), C_2 and C_3 in SG-Si(B), have more negative charges than in G-Si (C_2 and

C₃). All these observations indicate that the bonding between Si and SG is stronger than that on G, providing further support for the stability of Si on SG.

To better understand the covalent synergy between Si and graphene substrates, the projected density of states (PDOS) of the Si atom over G and SG were calculated, based on the electron structure and bonding. As shown in **Figure 6.6 a**, there is a harmonic 2p-2p overlaps between the C₁-2p and C₂-2p states at the whole energy level (from 0 to -10eV) in SG, showing the strong interaction between the two C atoms. However, for Si and C, the harmonic overlap occurs only between Si₄-2p and C₂-2p at a narrow energy level (-2~-4eV), indicating a weak interaction between Si₄ and C₁ atom. For SG-Si (B), a large overlap between the C₆-2p and S₅-2p state was observed (see **Figure 6.6 b**), indicating a strong S-C bonding. **Figure 6.6 c** shows that, more Si₉-2p state is occupied in SG-Si (B) and well mixed with C₂-2p state at a much broader energy level (from -1 to -9eV) as compared with that in G-Si. Additionally, there is also a harmonic overlap between Si₄-2p and S₅-2p state (see **Figure 6.6 d**). The analysis of the PDOS revealed that the covalent synergy was mainly due to the mixing between the C-2p and Si-2p states and the C₂-Si₉ bond is much stronger than the C₂-Si₄ bonding in G-Si, which attributes to the significantly improved cycle stability.

The mobility of this adsorbed Li atom was also studied. **Figure S11 (Appendix I)** shows the transition state along the diffusion pathway. It was found that, for Li atom diffuses away from the aforementioned most stable sites in G-Si, it needs to overcome an energy barrier of 0.75eV, as shown in **Figure S11a (Appendix I)**. However, the study of Li surface diffusion on SG-Si(B) cluster shows that Li diffusion proceeds with a barrier of 0.53eV, **Figure S11b (Appendix I)**, which is slightly lower than that found on G-Si. This observation indicates that S-doped graphene could boost the mobility for Li atoms on Si-SG interphase, which facilitate the charge transfer.

It can be seen that Si bonds more strongly to SG than on G. One reason is the covalent interaction of Si atoms with the sulfur atom. The second reason is because the increased charge density on the defective

carbon adjacent to sulfur. This indicates a covalent synergy for the interaction between Si and SG leading to a superior material electrochemical performance. It is clearly shown that, even after 2200 cycles of charge/discharge, the amorphous SiNP re-organised into channels of the cyclized PAN and the sulfur pathway on graphene, as seen in **Figure 6.4**.

In summary, the novel design of a Si-based electrode through the covalent binding of commercial SiNP and SG along with cyclized PAN offers exceptional potential in the practical utilization of Si anodes for Li-ion battery technologies. This covalent synergy enables superior cycling stability along with a high areal capacity of the electrode which is close to that of commercial technologies. Such a rational design and scalable fabrication paves the way for the real application of Si anodes in high-performance lithium-ion batteries.

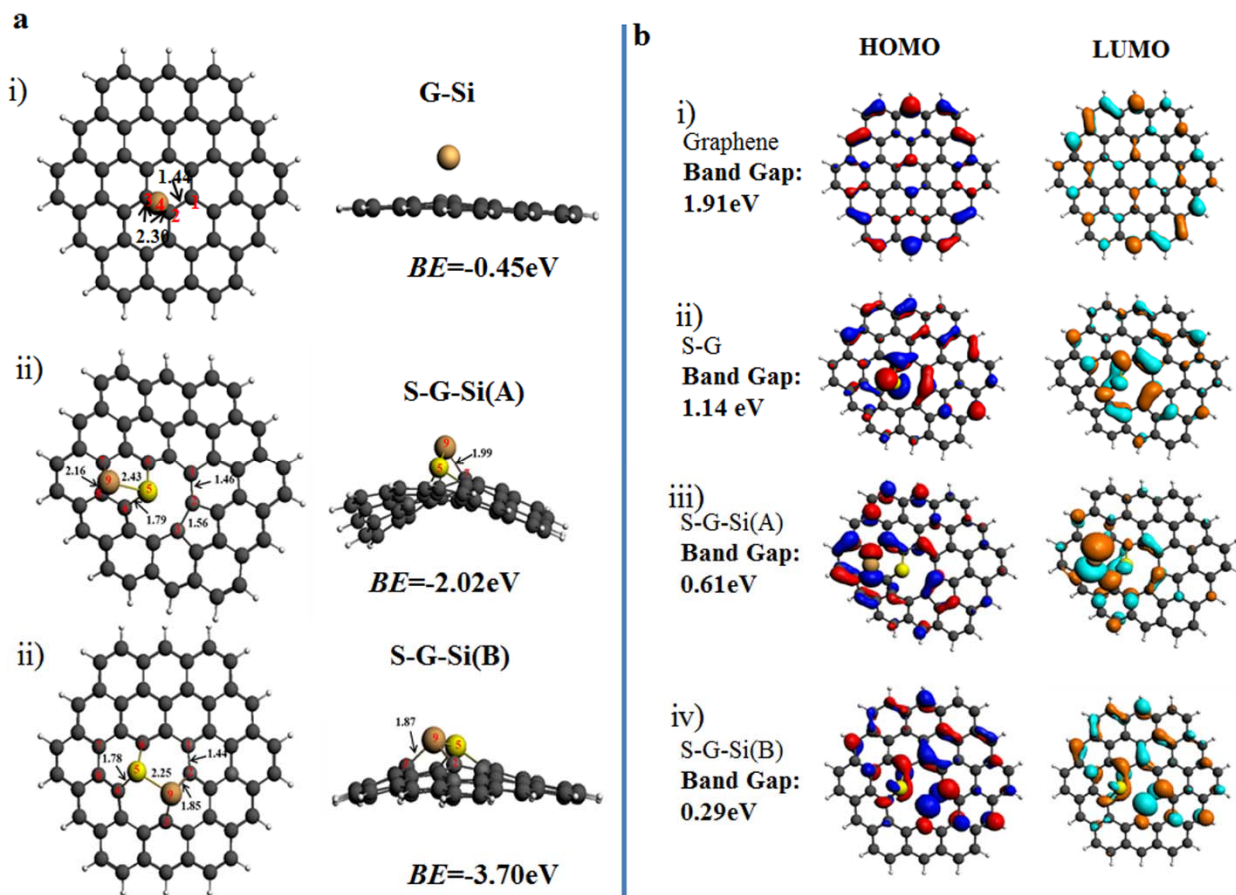


Figure 6-5. DFT quantum calculations for G-Si and SG-Si systems. a) Geometries and binding energy (BE) of the stable Si adsorption configurations on i): graphene, referred as G-Si; ii) and iii): on sulfur doped graphene, referred as S-G-Si(A) and S-G-Si(B), respectively, C atoms are colored grey, H atoms white, S atom yellow, Si atom brown. Some of the important atoms were labeled, and they correspond to the atoms in Table S1, and b) The DFT calculated band gap together with the highest occupied molecular orbital (HOMO) and lowest unoccupied molecular orbital (LUMO) for different graphene substrates.

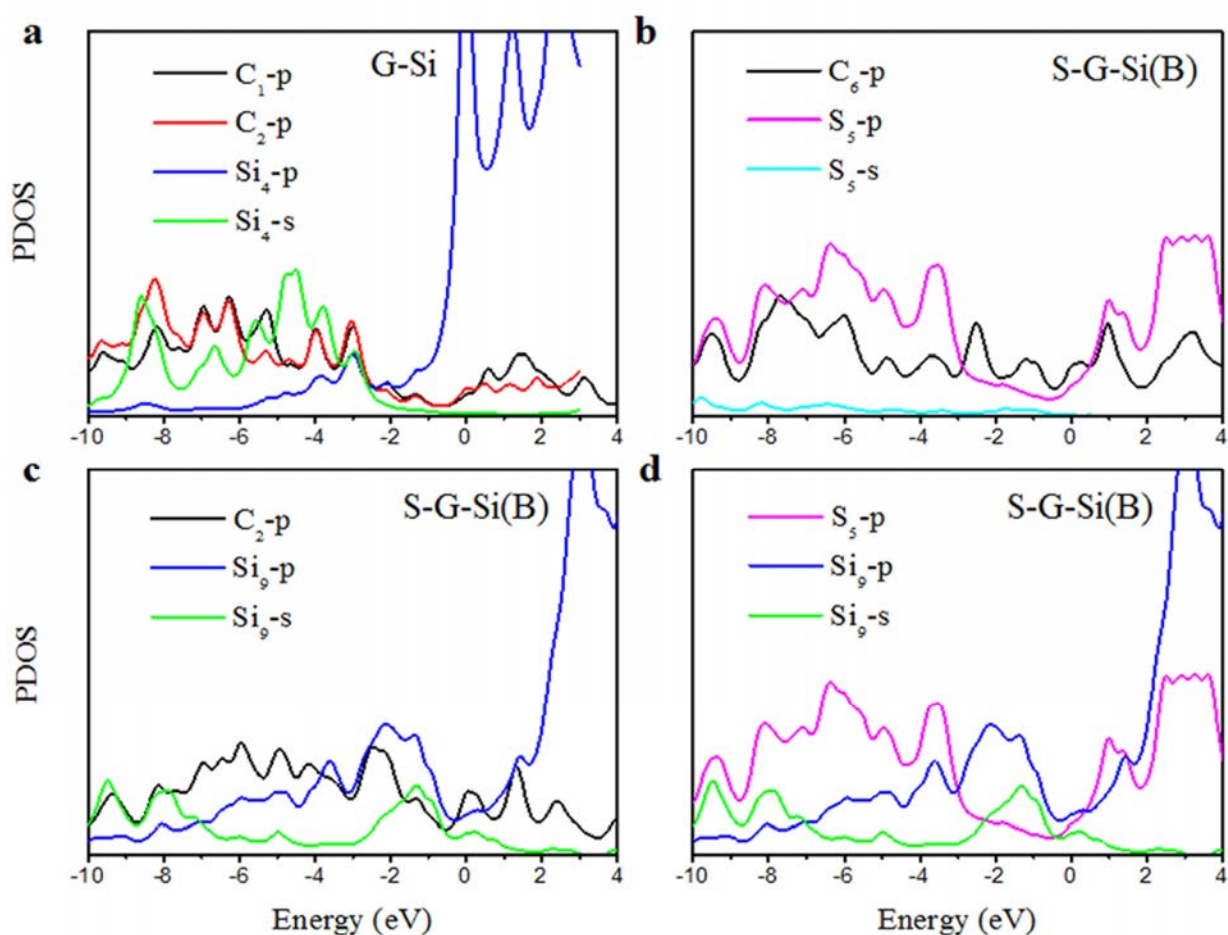


Figure 6-6. Projected density of states (PDOS) for Si atom and the individual C atoms involved in (a) Si adsorption on graphene, G-Si, and (b-d) sulfur doped graphene, SG-Si(B).

6.3 Materials and Methods

6.3.1 Preparation of S doped graphene (SG)

100 mg of graphene oxide (GO) prepared by a modified Hummer's method^{199, 200, 211} was mixed with 100 mg of phenyl disulfide (PDS) by grinding. The materials were loaded into a tube furnace and kept outside the heating zone until the furnace temperature reached 1000°C. The sample was then slid into the heating zone where it remained for 30 minutes under argon protection, followed by cooling to room temperature. Graphene was prepared under identical conditions without PDS.

6.3.2 Electrode fabrication and testing

Electrodes were fabricated using commercially available (*Nanostructured & Amorphous Materials, Inc., Houston, USA*) silicon nanoparticles (SiNP) with a size range of 50-70 nm. A slurry consisting of 50 wt% SiNP, 30 wt% polyacrylonitrile (PAN), 19wt% sulfur-doped graphene and 1 wt% graphene oxide (GO) was prepared in dimethylformamide (DMF). The addition of GO was to induce cyclization of PAN by oxidation. The slurry is mixed under alternating magnetic stirring and ultrasonic radiation (1 hour each, for 3 times). The slurry was then coated on Cu foil, dried in a convection oven at 353 K for 1 h, and then in a vacuum oven at 363 K overnight. Circular working electrodes of 1 cm² were cut with the average mass loading of silicon on the electrodes ranging from 0.8-1.5 mg cm⁻². The electrodes were then subjected to the SHT process. They were placed into a quartz tube of a horizontal tube furnace. Then subjected to slow heating up to 450°C in 2 hours, then holding for 10 minutes then furnace cooling (almost in another 2 hours). The treatment was performed under Argon gas flow of 100 SCCM.

Coin type half cells were fabricated in an argon-filled glove box with the working electrode and a Li metal counter electrode. The electrolyte used was 1M LiPF₆ in 30 wt% ethylene carbonate (EC), 60

wt% dimethyl carbonate (DMC), and 10wt% fluorinated ethylene carbonate (FEC). Galvanostatic charge/discharge testing was carried out at a cut off voltage range of 0.05 to 1.5 V with different current densities for rate capability testing. Cyclic voltammetry, at a scan rate of 0.05 mV s⁻¹ between 1.5 and 0.05 V, was conducted using a Princeton Applied Research VersaSTAT MC Potentiostat. One reference coin cell electrode was prepared with the same composition as above except for the SG was replaced with graphene. Another reference electrode was fabricated using the ratio of 70 wt% Si-NP, 30% polyacrylonitrile as a binder. These electrodes were subjected to SHT treatment.

6.3.3 Material Characterization

The morphologies of the electrode material were imaged using a transmission electron microscopic (TEM, JEOL 2010F TEM/STEM field emission microscope) equipped with a large solid angle for high-X-ray throughput, and a Gatan imaging filter (GIF) for energy filtered imaging. Thermal Gravimetric Analysis (TGA) and Differential Scanning Calorimetry (DSC) were measured using TA instrument Q500. The TGA testing was performed in air with a temperature range of 25 °C to 850 °C and a ramp rate of 10 °C min⁻¹. Raman spectroscopy were recorded using Bruker Senterra device, applying laser with wavelength of 532 nm.

6.3.4 Computational Method

The DFT calculations were carried out using the Amsterdam Density Functional “ADF”^{212, 213}. The electron wave functions were developed on a basis set of numerical atomic orbitals (NAOs) and of Slater type orbitals (STOs). In addition the triple polarization (TZP) basis of Slater-type orbitals was utilized. We used PBE-D3 to perform the calculations²¹⁴ where the generalized gradient approximation (GGA) for the exchange and correlation energy terms is used. This explicitly takes into

account the dispersion correction. This is a widely used function for catalysis applications and can produce reliable energetics on graphene systems.^{215,216}

Chapter 7 Conclusions and suggestions for future work

7.1 Conclusions and Summary

In conclusion, SnO₂ embedded in CMK-3 was prepared to investigate the electrochemical performances as anodes in a Li ion battery. Initially, Sn ion precursors were incorporated into CMK-3 and then annealed at different temperature under variable environmental conditions to obtain SnO₂/Sn/CMK-3 and Sn/CMK3. In terms of initial capacity, cycle stability and rate capability, SnO₂/Sn/CMK-3 demonstrated the best performances which are superior to the conventionally used graphite. It is proposed that metallic Sn contributes to the higher initial specific charge capacity of 799 mAhg⁻¹ compared to other previously reported Sn-based composites.^{47, 217} Meanwhile, the promising cycle stability and rate capability is attributed to the 3-D structure of the mesoporous carbon, CMK-3. The specific capacity of 350 mAhg⁻¹ was achieved at the current density of 800 mA g⁻¹ and the retention capacity of 670.9 mAhg⁻¹ was obtained at 50 cycles. With the remarkable rate capability and cycle stability, the SnO₂/Sn/CMK-3 composite is considered as highly promising negative electrode materials for next generation Li ion batteries.

After that, we have developed a simple, one-pot synthesis methodology capable of growing bulk SiNWs on low cost NiNP catalysts. Furthermore, we illustrated the potential for these NiNPs to be simultaneously anchored to three dimensional support materials, enabling a large range of future application areas for this method of (111) SiNWs growth. After growing the carbon coated c-SiNW-G composite, we were able to show its excellent durability and retention of capacity at high current density (100th cycle: 550 mAh g⁻¹ @ 6.8 A g⁻¹) as an anode in a LIB cell. Ultimately, this process creates an important building block for a new wave of low cost, high rate, silicon nanowire materials.

Additionally, the success of developing a simple strategy to treat the Si-based electrode to dramatically improve the performance reveals an elegant approach to solving an old problem, providing a scalable methodology for treating commercial Si particles. The flash heat treatment provides an effective approach to engineer, in a single step: the interfacial contact with copper, the binding matrix and the creation of a synergistic SiO₂/C coating. The treated electrodes possess built-in void space for rapid ion transport and successfully retain strong contact between the SiO₂/C shell and the Si-NP, promoting efficient electron transport even after long-term cycling. As a result the enhanced electrodes allow for the controlled expansion of Si and achieve high reversible capacity (2240 mA h g⁻¹ @ 120 mA g⁻¹), as well as, good rate capability and durability (1150 mA h g⁻¹ @ 1200 mA g⁻¹ over 500 cycles). Further, elimination of binder facilitates high temperature operation in industrial applications which limit the current electrode design standard. The emphasis of a simplified process represents a promising avenue for the production of industrially viable high-performance Si-based electrodes, which could be extended for roll-to-roll manufacturing of next-generation lithium-ion batteries.

Finally, the novel design of Si-based electrode through covalent binding commercial Si nanosized particles and sulfur-doped graphene along with cyclized PAN offers exceptional potential in the practical utilization of Si anodes and other energy storage applications. This covalent synergy enables the electrode with superior cycling stability along with a high areal capacity which is close to that of commercial electrodes. Such a rational design and scalable fabrication paves the way for real application of Si anodes in high-performance lithium-ion batteries.

7.2 Suggestions for Future Work

As a suggestion for future work it is likely to propose the following prospective:

- 1- Regarding Sn-based materials, it is important to propose a nanostructure based on Sn chalcogenides. In this regard, the sulfur might be able to contribute to reversible capacity, unlike oxygen in SnO₂. If this happens, it will increase the Coulombic efficiency of the first cycle, in addition to increasing the overall capacity of the anode material.
- 2- Because the degradation of Sn based electrodes may be minimized by controlling the particle size down to a critical size that compensate mechanical instability, the synthesis of Sn nanoparticles with sizes down to 10 nm is proposed. This nanostructure can be supported by SG and shielded with cyclized PAN. This may introduce a robust new design with high volumetric capacity and long cycle stability.
- 3- As this goes with cyclized PAN, I suggest a more in depth study that elucidates structural changes in PAN as a function of temperature. These elucidated concepts can then be applied to other electrode materials, including cathode material.

References

1. Lee J-S, Tai Kim S, Cao R, Choi N-S, Liu M, Lee KT, Cho J. Metal–Air Batteries with High Energy Density: Li–Air versus Zn–Air. *Advanced Energy Materials* 2011, **1**(1): 34-50.
2. Magasinski A, Dixon P, Hertzberg B, Kvit A, Ayala J, Yushin G. High-performance lithium-ion anodes using a hierarchical bottom-up approach. *Nature Materials* 2010, **9**(4): 353-358.
3. Li X, Gu M, Hu S, Kennard R, Yan P, Chen X, Wang C, Sailor MJ, Zhang J-G, Liu J. Mesoporous silicon sponge as an anti-pulverization structure for high-performance lithium-ion battery anodes. *Nat Commun* 2014, **5**.
4. Wang C, Wu H, Chen Z, McDowell MT, Cui Y, Bao Z. Self-healing chemistry enables the stable operation of silicon microparticle anodes for high-energy lithium-ion batteries. *Nat Chem* 2013, **5**(12): 1042-1048.
5. Wu H, Yu G, Pan L, Liu N, McDowell MT, Bao Z, Cui Y. Stable Li-ion battery anodes by in-situ polymerization of conducting hydrogel to conformally coat silicon nanoparticles. *Nat Commun* 2013, **4**.
6. Tarascon JM, Armand M. Issues and challenges facing rechargeable lithium batteries. *Nature* 2001, **414**(6861): 359-367.
7. Landi BJ, Ganter MJ, Cress CD, DiLeo RA, Raffaele RP. Carbon nanotubes for lithium ion batteries. *Energy & Environmental Science* 2009, **2**(6): 638-654.
8. Winter M, Brodd RJ. What Are Batteries, Fuel Cells, and Supercapacitors? *Chemical Reviews* 2004, **104**(10): 4245-4270.
9. Whittingham MS. Lithium Batteries and Cathode Materials. *Chemical Reviews* 2004, **104**(10): 4271-4302.
10. Amatucci GG, Tarascon JM, Klein LC. CoO₂, The End Member of the Li_xCoO₂ Solid Solution. *Journal of the Electrochemical Society* 1996, **143**(3): 1114-1123.
11. Thackeray MM, David WIF, Bruce PG, Goodenough JB. Lithium insertion into manganese spinels. *Materials Research Bulletin* 1983, **18**(4): 461-472.

12. Tarascon JM, Guyomard D. New electrolyte compositions stable over the 0 to 5 V voltage range and compatible with the $\text{Li}_{1+x}\text{Mn}_2\text{O}_4$ /carbon Li-ion cells. *Solid State Ionics* 1994, **69**(3–4): 293-305.
13. Tarascon JM, McKinnon WR, Coowar F, Bowmer TN, Amatucci G, Guyomard D. Synthesis Conditions and Oxygen Stoichiometry Effects on Li Insertion into the Spinel LiMn_2O_4 . *Journal of the Electrochemical Society* 1994, **141**(6): 1421-1431.
14. Thackeray MM. Manganese oxides for lithium batteries. *Progress in Solid State Chemistry* 1997, **25**(1–2): 1-71.
15. Yonemura M, Yamada A, Kobayashi H, Tabuchi M, Kamiyama T, Kawamoto Y, Kanno R. Synthesis, structure, and phase relationship in lithium manganese oxide spinel. *Journal of Materials Chemistry* 2004, **14**(13): 1948-1958.
16. Du Pasquier A, Blyr A, Courjal P, Larcher D, Amatucci G, Gérard B, Tarascon JM. Mechanism for Limited 55°C Storage Performance of $\text{Li}_{1.05}\text{Mn}_{1.95}\text{O}_4$ Electrodes. *Journal of the Electrochemical Society* 1999, **146**(2): 428-436.
17. Ohzuku T, Takeda S, Iwanaga M. Solid-state redox potentials for $\text{Li}[\text{Me}_{1/2}\text{Mn}_{3/2}]\text{O}_4$ (Me: 3d-transition metal) having spinel-framework structures: a series of 5 volt materials for advanced lithium-ion batteries. *Journal of Power Sources* 1999, **81–82**(0): 90-94.
18. Sigala C, Guyomard D, Verbaere A, Piffard Y, Tournoux M. Positive electrode materials with high operating voltage for lithium batteries: $\text{LiCr}_y\text{Mn}_{2-y}\text{O}_4$ ($0 \leq y \leq 1$). *Solid State Ionics* 1995, **81**(3–4): 167-170.
19. Arillo MA, Cuello G, López ML, Martín P, Pico C, Veiga ML. Structural characterisation and physical properties of LiMMnO_4 (M=Cr, Ti) spinels. *Solid State Sciences* 2005, **7**(1): 25-32.
20. Fang H, Wang Z, Zhang B, Li X, Li G. High performance $\text{LiNi}_{0.5}\text{Mn}_{1.5}\text{O}_4$ cathode materials synthesized by a combinational annealing method. *Electrochemistry Communications* 2007, **9**(5): 1077-1082.
21. Wohlfahrt-Mehrens M. SECONDARY BATTERIES – LITHIUM RECHARGEABLE SYSTEMS – LITHIUM-ION | Positive Electrode: Manganese Spinel Oxides. In: Garche J (ed). *Encyclopedia of Electrochemical Power Sources*, <http://dx.doi.org/10.1016/B978-044452745-5.00198-2>. Elsevier: Amsterdam, 2009, pp 318-327.

22. Padhi AK, Nanjundaswamy KS, Goodenough JB. Phospho-olivines as Positive-Electrode Materials for Rechargeable Lithium Batteries. *Journal of the Electrochemical Society* 1997, **144**(4): 1188-1194.
23. Yang S, Zavalij PY, Stanley Whittingham M. Hydrothermal synthesis of lithium iron phosphate cathodes. *Electrochemistry Communications* 2001, **3**(9): 505-508.
24. Chung S-Y, Bloking JT, Chiang Y-M. Electronically conductive phospho-olivines as lithium storage electrodes. *Nature Materials* 2002, **1**(2): 123-128.
25. Malik R, Burch D, Bazant M, Ceder G. Particle Size Dependence of the Ionic Diffusivity. *Nano Letters* 2010, **10**(10): 4123-4127.
26. Brodd RJ. *Batteries for sustainability : selected entries from the Encyclopedia of sustainability science and technology*.
27. Yoshio M, Brodd RJ, Kozawa A. *Lithium-ion batteries : science and technologies*. Springer: New York, 2009.
28. Inaba M. SECONDARY BATTERIES – LITHIUM RECHARGEABLE SYSTEMS – LITHIUM-ION | Negative Electrodes: Graphite. In: Garche J (ed). *Encyclopedia of Electrochemical Power Sources*, <http://dx.doi.org/10.1016/B978-044452745-5.00189-1>. Elsevier: Amsterdam, 2009, pp 198-208.
29. Larcher D, Beattie S, Morcrette M, Edstrom K, Jumas J-C, Tarascon J-M. Recent findings and prospects in the field of pure metals as negative electrodes for Li-ion batteries. *Journal of Materials Chemistry* 2007, **17**(36): 3759-3772.
30. Winter M, Besenhard JO, Spahr ME, Novák P. Insertion Electrode Materials for Rechargeable Lithium Batteries. *Advanced Materials* 1998, **10**(10): 725-763.
31. Dey AN. Electrochemical Alloying of Lithium in Organic Electrolytes. *Journal of the Electrochemical Society* 1971, **118**(10): 1547-1549.
32. Huggins RA. Lithium alloy negative electrodes. *Journal of Power Sources* 1999, **81-82**(0): 13-19.
33. Goodenough JB, Kim Y. Challenges for Rechargeable Li Batteries†. *Chemistry of Materials* 2009, **22**(3): 587-603.

34. Xu K. Nonaqueous Liquid Electrolytes for Lithium-Based Rechargeable Batteries. *Chemical Reviews* 2004, **104**(10): 4303-4418.
35. Salomon M. ELECTROLYTES | Overview. In: Garche J (ed). *Encyclopedia of Electrochemical Power Sources*, <http://dx.doi.org/10.1016/B978-044452745-5.00009-5>. Elsevier: Amsterdam, 2009, pp 134-139.
36. Hassan FM, Chen Z, Yu A, Chen Z, Xiao X. Sn/SnO₂ embedded in mesoporous carbon nanocomposites as negative electrode for lithium ion batteries. *Electrochimica Acta* 2013, **87**(0): 844-852.
37. Winter M, Besenhard JO. Electrochemical lithiation of tin and tin-based intermetallics and composites. *Electrochimica Acta* 1999, **45**(1-2): 31-50.
38. Ng MF, Zheng JW, Wu P. Evaluation of Sn Nanowire Encapsulated Carbon Nanotube for a Li-Ion Battery Anode by DFT Calculations. *Journal of Physical Chemistry C* 2010, **114**(18): 8542-8545.
39. Park CM, Kim JH, Kim H, Sohn HJ. Li-alloy based anode materials for Li secondary batteries. *Chemical Society Reviews* 2010, **39**(8): 3115-3141.
40. Han WQ, Zettl A. Coating single-walled carbon nanotubes with tin oxide. *Nano Letters* 2003, **3**(5): 681-683.
41. Chen YJ, Zhu CL, Xue XY, Shi XL, Cao MS. High capacity and excellent cycling stability of single-walled carbon nanotube/SnO(2) core-shell structures as Li-insertion materials. *Applied Physics Letters* 2008, **92**(22).
42. Ahn D, Xiao X, Li Y, Sachdev AK, Park HW, Yu A, Chen Z. Applying functionalized carbon nanotubes to enhance electrochemical performances of tin oxide composite electrodes for Li-ion battery. *Journal of Power Sources* 2012, **212**(0): 66-72.
43. Hsu RS, Higgins D, Chen ZW. Tin-oxide-coated single-walled carbon nanotube bundles supporting platinum electrocatalysts for direct ethanol fuel cells. *Nanotechnology* 2010, **21**(16).
44. Noerochim L, Wang J-Z, Chou S-L, Li H-J, Liu H-K. SnO₂-coated multiwall carbon nanotube composite anode materials for rechargeable lithium-ion batteries. *Electrochimica Acta* 2010, **56**(1): 314-320.

45. Paek SM, Yoo E, Honma I. Enhanced Cyclic Performance and Lithium Storage Capacity of SnO(2)/Graphene Nanoporous Electrodes with Three-Dimensionally Delaminated Flexible Structure. *Nano Letters* 2009, **9**(1): 72-75.
46. Zhang LS, Jiang LY, Yan HJ, Wang WD, Wang W, Song WG, Guo YG, Wan LJ. Mono dispersed SnO(2) nanoparticles on both sides of single layer graphene sheets as anode materials in Li-ion batteries. *Journal of Materials Chemistry* 2010, **20**(26): 5462-5467.
47. Zhong C, Wang JZ, Chen ZX, Liu HK. SnO(2)-Graphene Composite Synthesized via an Ultrafast and Environmentally Friendly Microwave Autoclave Method and Its Use as a Superior Anode for Lithium-Ion Batteries. *Journal of Physical Chemistry C* 2011, **115**(50): 25115-25120.
48. Xu C, Sun J, Gao L. Direct growth of monodisperse SnO₂ nanorods on graphene as high capacity anode materials for lithium ion batteries. *Journal of Materials Chemistry* 2012, **22**: 975-979.
49. Wen Z, Cui S, Kim H, Mao S, Yu K, Lu G, Pu H, Ou Mao O, Chen J. Binding Sn-based nanoparticles on graphene as the anode of rechargeable lithium-ion batteries. *Journal of Materials Chemistry* 2012, **22**: 3300-3306.
50. Yu ZY, Zhu SM, Li Y, Liu QL, Feng CL, Zhang D. Synthesis of SnO(2) nanoparticles inside mesoporous carbon via a sonochemical method for highly reversible lithium batteries. *Materials Letters* 2011, **65**(19-20): 3072-3075.
51. Wang XQ, Liu R, Waje MM, Chen ZW, Yan YS, Bozhilov KN, Feng PY. Sulfonated ordered mesoporous carbon as a stable and highly active protonic acid catalyst. *Chemistry of Materials* 2007, **19**(10): 2395-2397.
52. Zhao D, Feng J, Huo Q, Melosh N, Fredrickson GH, Chemlka BF, Stucky GD. *Science* 1998, **279**: 548.
53. Jun S, Joo SH, Ryoo R, Kruk M, Jaroniec M, Liu Z, Ohsuna T, Terasiki O. Synthesis of New, Nanoporous Carbon with Hexagonally Ordered Mesostructure. *Journal of the American Chemical Society* 2000, **122**: 10712-10713.
54. Kim Y, Yoon Y, Shin D. Fabrication of Sn/SnO(2) composite powder for anode of lithium ion battery by aerosol flame deposition. *Journal of Analytical and Applied Pyrolysis* 2009, **85**(1-2): 557-560.

55. Meduri P, Pendyala C, Kumar V, Sumanasekera GU, Sunkara MK. Hybrid Tin Oxide Nanowires as Stable and High Capacity Anodes for Li-Ion Batteries. *Nano Letters* 2009, **9**(2): 612-616.
56. Wang CM, Xu W, Liu J, Zhang JG, Saraf LV, Arey BW, Choi DW, Yang ZG, Xiao J, Thevuthasan S, Baer DR. In Situ Transmission Electron Microscopy Observation of Microstructure and Phase Evolution in a SnO(2) Nanowire during Lithium Intercalation. *Nano Letters* 2011, **11**(5): 1874-1880.
57. Sivashanmugam A, Kumar TP, Renganathan NG, Gopukumar S, Wohlfahrt-Mehrens M, Garche J. Electrochemical behavior of Sn/SnO₂ mixtures for use as anode in lithium rechargeable batteries. *Journal of Power Sources* 2005, **144**(1): 197-203.
58. Teki R, Datta MK, Krishnan R, Parker TC, Lu T-M, Kumta PN, Koratkar N. Nanostructured Silicon Anodes for Lithium Ion Rechargeable Batteries. *Small* 2009, **5**(20): 2236–2242.
59. Li H, Wang Z, Chen L, Huang X. Research on Advanced Materials for Li-ion Batteries. *Advanced Materials* 2009, **21**: 4593–4607.
60. Yang Y, McDowell MT, Jackson A, Cha JJ, Hong SS, Cui Y. New Nanostructured Li₂S/Silicon Rechargeable Battery with High Specific Energy. *Nano Letters* 2010, **10**: 1486–1491.
61. Courtel FM, Niketic S, Duguay D, Abu-Lebdeh Y, Davidson IJ. Water-soluble binders for MCMB carbon anodes for lithium-ion batteries. *Journal of Power Sources* 2011, **196**(4): 2128-2134.
62. Zhou H, Zhu S, Hibino M, Honma I, Ichihara M. Lithium Storage in Ordered Mesoporous Carbon (CMK-3) with High Reversible Specific Energy Capacity and Good Cycling Performance. *Advanced Materials* 2003, **15**(24): 2107-2111.
63. Hassan FM, Elsayed AR, Chabot V, Batmaz R, Xiao X, Chen Z. Subeutectic Growth of Single-Crystal Silicon Nanowires Grown on and Wrapped with Graphene Nanosheets: High-Performance Anode Material for Lithium-Ion Battery. *ACS Applied Materials & Interfaces* 2014, **6**(16): 13757-13764.
64. Hassan F, Chen Z, Yu A, Xao X. Sn/SnO₂ Embedded in Mesoporous Carbon Nanocomposites as Negative Electrode for Lithium Ion Batteries. *Electrochimica Acta* 2012, **87**(1): 844-852.

65. Liao J-Y, Higgins D, Liu G, Chabot V, Xiao X, Chen Z. Multifunctional TiO₂-C/MnO₂ Core-Double-Shell Nanowire Arrays as High-Performance 3D Electrodes for Lithium Ion Batteries. *Nano Letters* 2013, **13**(11): 5467-5473.
66. Yu A, Park HW, Davies A, Higgins D, Chen Z, Xiaio X. Free-Standing Layer-by-Layer Hybrid Thin Film of Graphene-MnO₂ Nanotube as Anode for Lithium Ion Batteries. *J Phys Chem Lett* 2011, **2**(15): 1855-1860.
67. Tarascon J-M, Armand M. Issues and Challenges facing rechargeable lithium batteries. *Nature* 2001, **414**: 359-367.
68. Armand M, Tarascon J-M. Building Better Batteries. *Nature* 2008, **451**: 652-657.
69. Yu Y, Gu L, Zhu C, Tsukimoto S, Aken PA, Maier J. Reversible Storage of Lithium in Silver-Coated Three-Dimensional Macroporous Silicon. *Advanced Materials* 2010, **22**(20): 2247-2250.
70. Kim H, Seo M, Park M-H, Cho J. A Critical Size of Silicon Nano-Anodes for Lithium Rechargeable Batteries. *Angewandte Chemie International Edition* 2010, **49**: 2146-2149.
71. Sharma RA, Seefurth RN. Thermodynamic Properties of the Lithium-Silicon System. *Journal of the Electrochemical Society* 1976, **123**(12): 1763-1768.
72. Wu H, Cui Y. Designing nanostructured Si anodes for high energy lithium ion batteries. *Nanotoday* 2012, **7**(5): 414-429.
73. Chan CK, Peng H, Liu G, McIlwraith K, Zhang XF, Huggins RA, Cui Y. High-performance lithium battery anodes using silicon nanowires. *Nature Nanotechnology* 2008, **3**: 31-35.
74. Kim H, Han B, Choo J, Cho J. Three-Dimensional Porous Silicon Particles for Use in High-Performance Lithium Secondary Batteries. *Angewandte Chemie International Edition* 2008, **47**(52): 10151-10154.
75. Besenhard JO, Yang J, Winter M. Will advanced lithium-alloy anodes have a chance in lithium-ion batteries? *Journal of Power Sources* 1997, **68**(1): 87-90.

76. Raimann PR, Hochgatterer NS, Korepp C, Möller KC, Winter M, Schröttner H, Hofer F, Besenhard JO. Monitoring dynamics of electrode reactions in Li-ion batteries by in-situ ESEM. *Ionics* 2006, **12**(4-5): 253-255.
77. Beaulieu LY, Eberman KW, Turner RL, Krause LJ, Dahn JR. Colossal Reversible Volume Changes in Lithium Alloys. *Electrochemical and Solid-State Letters* 2001, **4**(9): A137-140.
78. Holzapfel M, Buga H, Scheifele W, Novak P, Petrat F-M. A new type of nano-sized silicon/carbon composite electrode for reversible lithium insertion. *Chemical Communications* 2005, **12**(12): 1566-1568.
79. Wu H, Chan G, Choi JW, Ryu I, Yao Y, McDowell MT, Lee SE, Jackson A, Yang Y, Hu L, Cui Y. Stable cycling of double-walled silicon nanotube battery anodes through solid-electrolyte interphase control. *Nature Nanotechnology* 2012, **7**: 310-315.
80. Kasavajjula U, Wang C, Appleby AJ. Nano- and bulk-silicon-based insertion anodes for lithium-ion secondary cells. *Journal of Power Sources* 2007, **163**: 1003-1039.
81. Ji L, Zhang X. Evaluation of Si/carbon composite nanofiber-based insertion anodes for new-generation rechargeable lithium-ion batteries. *Energy Environ Sci* 2010, **3**: 124-129.
82. Gómez Cámer JL, Morales J, Sánchez L, Ruch P, Ng SH, Kötz R, Novák P. Nanosized Si/cellulose fiber/carbon composites as high capacity anodes for lithium-ion batteries: A galvanostatic and dilatometric study. *Electrochimica Acta* 2009, **54**(26): 6713-6717.
83. Liu N, Wu H, McDowell MT, Yao Y, Wang C, Cui Y. A yolk-shell design for stabilized and scalable li-ion battery alloy anodes. *Nano Letters* 2012, **12**(6): 3315-3321.
84. Luo J, Zhao X, Wu J, Jang HD, Kung HH, Huang J. Crumpled Graphene-Encapsulated Si Nanoparticles for Lithium Ion Battery Anodes. *J Phys Chem Lett* 2012, **3**(13): 1824-1829.
85. Zhou X, Yin YX, Wan LJ, Guo YG. Facile synthesis of silicon nanoparticles inserted into graphene sheets as improved anode materials for lithium-ion batteries. *Chemical Communications* 2012, **48**(16): 2198-2200.
86. Jang S-M, Miyawaki J, Tsuji M, Mochida I, Yoon S-H. The preparation of a novel Si-CNF composite as an effective anodic material for lithium-ion batteries. *Carbon* 2009, **47**(15): 3383-3391.

87. Zhao X, Hayner CM, Kung MC, Kung HH. In-Plane Vacancy-Enabled High-Power Si-Graphene Composite Electrode for Lithium-Ion Batteries. *Adv Energy Mater* 2011, **1**(6): 1079-1084.
88. Lee JK, Smith KB, Hayner CM, Kung HH. Silicon nanoparticles-graphene paper composites for Li ion battery anodes. *Chemical Communications* 2010, **46**: 2025-2027.
89. Tao H-C, Fan L-Z, Mei Y, Qu X. Self-supporting Si/Reduced Graphene Oxide nanocomposite films as anode for lithium ion batteries. *Electrochemistry Communications* 2011, **13**(12): 1332-1335.
90. Xin X, Zhou X, Wang F, Yao X, Xu X, Zhu Y, Liu Z. A 3D porous architecture of Si/graphene nanocomposite as high-performance anode materials for Li-ion batteries. *Journal of Materials Chemistry* 2012, **22**: 7724-7730.
91. Cui L-F, Ruffo R, Chan CK, Peng H, Cui Y. Crystalline-Amorphous Core-Shell Silicon Nanowires for High Capacity and High Current Battery Electrodes. *Nano Letters* 2009, **9**(1): 491-495.
92. Zhang Q, Cui Y, Wang E. Anisotropic Lithium Insertion Behavior in Silicon Nanowires: Binding Energy, Diffusion Barrier, and Strain Effect. *J Phys Chem C* 2011, **115**(19): 9376-9381.
93. Wang XL, Han WQ. Graphene enhances Li storage capacity of porous single-crystalline silicon nanowires. *ACS Applied Materials & Interfaces* 2010, **2**(12): 3709-3713.
94. Zhang C, Gu L, Kaskhedikar N, Cui G, Maier J. Preparation of silicon@silicon oxide core-shell nanowires from a silica precursor toward a high energy density Li-ion battery anode. *ACS Applied Materials & Interfaces* 2013, **5**(23): 12340-12345.
95. Lee SE, Kim HJ, Kim H, Park JH, Choi DG. Highly robust silicon nanowire/graphene core-shell electrodes without polymeric binders. *Nanoscale* 2013, **5**(19): 8986-8991.
96. Ge M, Rong J, Fang X, Zhang A, Lu Y, Zhou C. Scalable preparation of porous silicon nanoparticles and their application for lithium-ion battery anodes. *Nano Research* 2013, **6**(3): 174-181.
97. Wang B, Li X, Zhang X, Luo B, Zhang Y, Zhi L. Contact-Engineered and Void-Involved Silicon/Carbon Nanohybrids as Lithium-Ion-Battery Anodes. *Advanced Materials* 2013, **25**(26): 3560-3565.

98. Wu Y, Cui Y, Huynh L, Barrelet CJ, Bell DC, Lieber CM. Controlled Growth and Structures of Molecular-Scale Silicon Nanowires. *Nano Letters* 2004, **4**(3): 433-436.
99. Park M-H, Kim MG, Joo J, Kim K, Kim J, Ahn S, Cui Y, Cho J. Silicon Nanotube Battery Anodes. *Nano Letters* 2009, **9**(11): 3844-3847.
100. Hassan F, Chabot V, Elsayed AR, Xiao X, Chen Z. Engineered Si electrode nano-architecture: A scalable treatment for the production of next-generation Li-ion batteries. *Nano Letters* 2014, **14**(1): 277-283.
101. Schmidt V, Wittemann JV, Senz S, Gösele U. Silicon Nanowires: A Review on Aspects of their Growth and their Electrical Properties. *Advanced Materials* 2009, **21**(25-26): 2681-2702.
102. Song T, Xia J, Lee J-H, Lee DH, Kwon M-S, Choi J-M, Wu J, Doo SK, Chang H, Park WI, Zang DS, Kim H, Huang Y, Hwang K-C, Rogers JA, Paik U. Arrays of Sealed Silicon Nanotubes as Anodes for Lithium Ion Batteries. *Nano Letters* 2010, **10**: 1710-1716.
103. Morales AM, Lieber CM. A Laser Ablation Method for the Synthesis of Crystalline Semiconductor Nanowires. *Science* 1998, **279**(5348): 208-211.
104. Givargizov EI. Fundamentals Aspects of VLS growth. *Journal of Crystal Growth* 1975, **31**: 20-30.
105. Wagner RS, Ellis WC. Vapor-Liquid-Solid Mechanism of Single Crystal Growth. *Applied Physics Letters* 1964, **4**(5): 89.
106. Chabot V, Feng K, Park HW, Hassan F, Elsayed AR, Yu A, Xiao X, Chen Z. Graphene wrapped silicon nanocomposites for enhanced electrochemical performance in lithium ion batteries. *Electrochimica Acta* 2014, **130**: 127-134.
107. Zhang Y, Zhang Q, Wang N, Yan Y, Huihua Z, Zhu J. Synthesis of thin Si whiskers (nanowires) using SiCl₄. *Journal of Crystal Growth* 2001, **226**: 185-191.
108. Ren JG, Wang C, Wu QH, Liu X, Yang Y, He L, Zhang W. A silicon nanowire-reduced graphene oxide composite as a high-performance lithium ion battery anode material. *Nanoscale* 2014, **6**(6): 3353-3360.

109. Léonard F, Talin AA. Electrical contacts to one- and two-dimensional nanomaterials. *Nature Nanotechnology* 2011, **6**: 773-783.
110. Dellas NS, Liu BZ, Eichfield SM, Mayer TS, Mohny SE. Orientation dependence of Nickel Silicide Formation in Contacts to Silicon Nanowires. *Journal of Applied Physics* 2009, **105**: 094309.
111. Nash P, Nash A. The Ni-Si (Nickel-Silicon) System. *Bulletin of Alloy Phase Diagrams* 1987, **9**(1): 6-14.
112. Hummers WS, Offeman RE. Preparation of Graphitic Oxide. *Journal of the American Chemical Society* 1958, **80**(6): 1339-1339.
113. Lee SW, McDowell MT, Choi JW, Cui Y. Anomalous shape changes of silicon nanopillars by electrochemical lithiation. *Nano Letters* 2011, **11**(7): 3034-3039.
114. Machado BF, Serf P. Graphene-based materials for catalysis. *Catal Sci Technol* 2012, **2**(1): 54-75.
115. Chabot V, Higgins D, Yu A, Xiao X, Chen Z, Zhang J. A review of graphene and graphene oxide sponge: material synthesis and applications to energy and the environment. *Energy Environ Sci* 2014, **7**(5): 1564-1596.
116. Kingma KJ, Hemley RJ. Raman spectroscopic study of microcrystalline silica. *American Mineralogist* 1994, **79**: 269-273.
117. Karakassides MA, Gournis D, Petridis D. An Infrared Reflectance Study of Si-O Vibrations in Thermally Treated Alkali-Saturated Montmorillonites. *Clay Miner* 1999, **34**: 429-438.
118. Ferrari AC. Raman spectroscopy of graphene and graphite: Disorder, electron-phonon coupling, doping and nonadiabatic effects. *Solid State Communications* 2007, **143**(1-2): 47-57.
119. Ferrari AC, Meyer JC, Scardaci V, Casiraghi C, Lazzeri M, Mauri F, Piscanec S, Jiang D, Novoselov SR, Geim AK. Raman Spectrum of Graphene and Graphene Layers. *Physical Review Letters* 2006, **97**: 187401.
120. Zou YQ, Wang Y. NiO nanosheets grown on graphene nanosheets as superior anode materials for Li-ion batteries. *Nanoscale* 2011, **3**: 2615-2620.

121. Guo P, Song H, Chen X. Electrochemical performance of graphene nanosheets as anode material for lithium-ion batteries. *Electrochemistry Communications* 2009, **11**(6): 1320-1324.
122. Pan D, Wang S, Zhao B, Wu M, Zhang H, Wang Y, Jiao Z. Li Storage Properties of Disordered Graphene Nanosheets. *Chemistry of Materials* 2009, **21**(14): 3136-3142.
123. Rahaman MSA, Ismail AF, Mustafa A. A review of heat treatment on polyacrylonitrile fiber. *Polymer Degradation and Stability* 2007, **92**(8): 1421-1432.
124. Hassan FM, Chabot V, Elsayed AR, Xiao X, Chen Z. Engineered Si Electrode Nanoarchitecture: A Scalable Postfabrication Treatment for the Production of Next-Generation Li-Ion Batteries. *Nano Letters* 2013, **14**(1): 277-283.
125. Liao J-Y, Xiao X, Higgins D, Lee D, Hassan F, Chen Z. Hierarchical Li₄Ti₅O₁₂-TiO₂ composite microsphere consisting of nanocrystals for high power Li-ion batteries. *Electrochimica Acta* 2013, **108**(0): 104-111.
126. Wu H, Cui Y. Designing nanostructured Si anodes for high energy lithium ion batteries. *Nano Today* 2012, **7**(5): 414-429.
127. Wilson AM, Dahn JR. Lithium Insertion in Carbons Containing Nanodispersed Silicon. *Journal of the Electrochemical Society* 1995, **142**(2): 326-332.
128. Gao P, Fu J, Yang J, Lv R, Wang J, Nuli Y, Tang X. Microporous carbon coated silicon core/shell nanocomposite via in situ polymerization for advanced Li-ion battery anode material. *Physical Chemistry Chemical Physics* 2009, **11**(47): 11101-11105.
129. Demir Cakan R, Titirici M-M, Antonietti M, Cui G, Maier J, Hu Y-S. Hydrothermal carbon spheres containing silicon nanoparticles: synthesis and lithium storage performance. *Chemical Communications* 2008, 10.1039/b805671b(32): 3759-3761.
130. Ng S-H, Wang J, Wexler D, Konstantinov K, Guo Z-P, Liu H-K. Highly Reversible Lithium Storage in Spheroidal Carbon-Coated Silicon Nanocomposites as Anodes for Lithium-Ion Batteries. *Angewandte Chemie International Edition* 2006, **45**(41): 6896-6899.
131. Koo B, Kim H, Cho Y, Lee KT, Choi N-S, Cho J. A Highly Cross-Linked Polymeric Binder for High-Performance Silicon Negative Electrodes in Lithium Ion Batteries. *Angewandte Chemie International Edition* 2012, **51**(35): 8762-8767.

132. Kovalenko I, Zdyrko B, Magasinski A, Hertzberg B, Milicev Z, Burtovyy R, Luzinov I, Yushin G. A Major Constituent of Brown Algae for Use in High-Capacity Li-Ion Batteries. *Science* 2011, **334**(6052): 75-79.
133. Han Z-J, Yabuuchi N, Shimomura K, Murase M, Yui H, Komaba S. High-capacity Si-graphite composite electrodes with a self-formed porous structure by a partially neutralized polyacrylate for Li-ion batteries. *Energy & Environmental Science* 2012, **5**(10): 9014-9020.
134. Ryou M-H, Kim J, Lee I, Kim S, Jeong YK, Hong S, Ryu JH, Kim T-S, Park J-K, Lee H, Choi JW. Mussel-Inspired Adhesive Binders for High-Performance Silicon Nanoparticle Anodes in Lithium-Ion Batteries. *Advanced Materials* 2013, **25**(11): 1571-1576.
135. Martin C, Alias M, Christien F, Crosnier O, Bélanger D, Brousse T. Graphite-Grafted Silicon Nanocomposite as a Negative Electrode for Lithium-Ion Batteries. *Advanced Materials* 2009, **21**(46): 4735-4741.
136. Li J, Christensen L, Obrovac MN, Hewitt KC, Dahn JR. Effect of Heat Treatment on Si Electrodes Using Polyvinylidene Fluoride Binder. *Journal of the Electrochemical Society* 2008, **155**(3): A234-A238.
137. Hochgatterer NS, Schweiger MR, Koller S, Raimann PR, Wöhrle T, Wurm C, Winter M. Silicon/Graphite Composite Electrodes for High-Capacity Anodes: Influence of Binder Chemistry on Cycling Stability. *Electrochemical and Solid-State Letters* 2008, **11**(5): A76-A80.
138. Beattie SD, Larcher D, Morcrette M, Simon B, Tarascon J-M. Si Electrodes for Li-Ion Batteries—A New Way to Look at an Old Problem. *Journal of the Electrochemical Society* 2008, **155**(2): A158-A163.
139. Magasinski A, Zdyrko B, Kovalenko I, Hertzberg B, Burtovyy R, Huebner CF, Fuller TF, Luzinov I, Yushin G. Toward Efficient Binders for Li-Ion Battery Si-Based Anodes: Polyacrylic Acid. *ACS Applied Materials & Interfaces* 2010, **2**(11): 3004-3010.
140. Champion CL, Li W, Lucht BL. Thermal Decomposition of LiPF₆-Based Electrolytes for Lithium-Ion Batteries. *Journal of the Electrochemical Society* 2005, **152**(12): A2327-A2334.
141. Chan CK, Patel RN, O'Connell MJ, Korgel BA, Cui Y. Solution-Grown Silicon Nanowires for Lithium-Ion Battery Anodes. *ACS Nano* 2010, **4**(3): 1443-1450.

142. Cui L-F, Ruffo R, Chan CK, Peng H, Cui Y. Crystalline-Amorphous Core–Shell Silicon Nanowires for High Capacity and High Current Battery Electrodes. *Nano Letters* 2008, **9**(1): 491-495.
143. Ji J, Ji H, Zhang LL, Zhao X, Bai X, Fan X, Zhang F, Ruoff RS. Graphene-Encapsulated Si on Ultrathin-Graphite Foam as Anode for High Capacity Lithium-Ion Batteries. *Advanced Materials* 2013, **25**(33): 4673-4677.
144. Kim H, Cho J. Superior Lithium Electroactive Mesoporous Si@Carbon Core–Shell Nanowires for Lithium Battery Anode Material. *Nano Letters* 2008, **8**(11): 3688-3691.
145. Magasinski A, Dixon P, Hertzberg B, Kvit A, Ayala J, Yushin G. High-performance lithium-ion anodes using a hierarchical bottom-up approach. *Nat Mater* 2010, **9**(5): 461-461.
146. McDowell MT, Lee SW, Ryu I, Wu H, Nix WD, Choi JW, Cui Y. Novel Size and Surface Oxide Effects in Silicon Nanowires as Lithium Battery Anodes. *Nano Letters* 2011, **11**(9): 4018-4025.
147. Sim S, Oh P, Park S, Cho J. Critical Thickness of SiO₂ Coating Layer on Core@Shell Bulk@Nanowire Si Anode Materials for Li-Ion Batteries. *Advanced Materials* 2013, **25**(32): 4498-4503.
148. Xu Y, Yin G, Ma Y, Zuo P, Cheng X. Nanosized core/shell silicon@carbon anode material for lithium ion batteries with polyvinylidene fluoride as carbon source. *Journal of Materials Chemistry* 2010, **20**(16): 3216-3220.
149. Guo J, Chen X, Wang C. Carbon scaffold structured silicon anodes for lithium-ion batteries. *Journal of Materials Chemistry* 2010, **20**(24): 5035-5040.
150. Yun M-S, Jeong K-Y, Lee E-W, Jin B-S, Moon S-I, Doh C-H. A study on carbon coating to silicon and electrochemical characteristics of Si-C/Li cells. *Korean Journal of Chemical Engineering* 2006, **23**(2): 230-236.
151. Chen S, He G, Hu H, Jin S, Zhou Y, He Y, He S, Zhao F, Hou H. Elastic carbon foam via direct carbonization of polymer foam for flexible electrodes and organic chemical absorption. *Energy & Environmental Science* 2013, **6**(8): 2435-2439.
152. Khriachtchev L, Kilpelä O, Karirinne S, Keränen J, Lepistö T. Substrate-dependent crystallization and enhancement of visible photoluminescence in thermal annealing of Si/SiO₂ superlattices. *Applied Physics Letters* 2001, **78**(3): 323-325.

153. Khriachtchev L, Räsänen M, Novikov S, Pavesi L. Systematic correlation between Raman spectra, photoluminescence intensity, and absorption coefficient of silica layers containing Si nanocrystals. *Applied Physics Letters* 2004, **85**(9): 1511-1513.
154. Nesheva D, Raptis C, Perakis A, Bineva I, Aneva Z, Levi Z, Alexandrova S, Hofmeister H. Raman scattering and photoluminescence from Si nanoparticles in annealed SiO_x thin films. *Journal of Applied Physics* 2002, **92**(8): 4678-4683.
155. Zhang W, Zhang S, Liu Y, Chen T. Evolution of Si suboxides into Si nanocrystals during rapid thermal annealing as revealed by XPS and Raman studies. *Journal of Crystal Growth* 2009, **311**(5): 1296-1301.
156. Kingma KJ, Hemley RJ. Raman-Spectroscopic Study of Microcrystalline Silica. *American Mineralogist* 1994, **79**(3-4): 269-273.
157. Karakassides MA, Gournis D, Petridis D. An infrared reflectance study of Si-O vibrations in thermally treated alkali-saturated montmorillonites. *Clay Minerals* 1999, **34**(3): 429-438.
158. Ferrari AC, Meyer JC, Scardaci V, Casiraghi C, Lazzeri M, Mauri F, Piscanec S, Jiang D, Novoselov KS, Roth S, Geim AK. Raman Spectrum of Graphene and Graphene Layers. *Physical Review Letters* 2006, **97**(18): 187401.
159. Ferrari AC. Raman spectroscopy of graphene and graphite: Disorder, electron-phonon coupling, doping and nonadiabatic effects. *Solid State Communications* 2007, **143**(1-2): 47-57.
160. Huang Y, Young RJ. Effect of fibre microstructure upon the modulus of PAN- and pitch-based carbon fibres. *Carbon* 1995, **33**(2): 97-107.
161. Dogan F, Joyce C, Vaughey JT. Formation of Silicon Local Environments upon Annealing for Silicon Anodes: A ²⁹Si Solid State NMR Study. *Journal of the Electrochemical Society* 2013, **160**(2): A312-A319.
162. Ge MY, Rong JP, Fang X, Zhang AY, Lu YH, Zhou CW. Scalable preparation of porous silicon nanoparticles and their application for lithium-ion battery anodes. *Nano Research* 2013, **6**(3): 174-181.
163. Ma DDD, Lee CS, Au FCK, Tong SY, Lee ST. Small-Diameter Silicon Nanowire Surfaces. *Science* 2003, **299**(5614): 1874-1877.

164. Egerton RF. Electron energy-loss spectroscopy in the TEM. *Reports on Progress in Physics* 2009, **72**(1): 016502.
165. Secco d' Aragona F. Dislocation Etch for (100) Planes in Silicon. *Journal of the Electrochemical Society* 1972, **119**(7): 948-951.
166. Xia YN, Mrksich M, Kim E, Whitesides GM. Microcontact Printing of Octadecylsiloxane on the Surface of Silicon Dioxide and Its Application in Microfabrication. *Journal of the American Chemical Society* 1995, **117**(37): 9576-9577.
167. Knotter DM. Etching mechanism of vitreous silicon dioxide in HF-based solutions. *Journal of the American Chemical Society* 2000, **122**(18): 4345-4351.
168. Li W, Li H, Zhang YM. Preparation and investigation of PVDF/PMMA/TiO₂ composite film. *Journal of Materials Science* 2009, **44**(11): 2977-2984.
169. Ge MY, Rong JP, Fang X, Zhou CW. Porous Doped Silicon Nanowires for Lithium Ion Battery Anode with Long Cycle Life. *Nano Letters* 2012, **12**(5): 2318-2323.
170. Li J, Dahn JR. An in situ X-ray diffraction study of the reaction of Li with crystalline Si. *Journal of the Electrochemical Society* 2007, **154**(3): A156-A161.
171. Chen XL, Li XL, Ding F, Xu W, Xiao J, Cao YL, Meduri P, Liu J, Graff GL, Zhang JG. Conductive Rigid Skeleton Supported Silicon as High-Performance Li-Ion Battery Anodes. *Nano Letters* 2012, **12**(8): 4124-4130.
172. Green M, Fielder E, Scrosati B, Wachtler M, Serra Moreno J. Structured silicon anodes for lithium battery applications. *Electrochemical and Solid State Letters* 2003, **6**(5): A75-A79.
173. Allen MJ, Tung VC, Kaner RB. Honeycomb Carbon: A Review of Graphene. *Chemical Reviews* 2010, **110**(1): 132-145.
174. de Heer WA, Berger C, Wu XS, First PN, Conrad EH, Li XB, Li TB, Sprinkle M, Hass J, Sadowski ML, Potemski M, Martinez G. Epitaxial graphene. *Solid State Communications* 2007, **143**(1-2): 92-100.

175. Li XS, Cai WW, An JH, Kim S, Nah J, Yang DX, Piner R, Velamakanni A, Jung I, Tutuc E, Banerjee SK, Colombo L, Ruoff RS. Large-Area Synthesis of High-Quality and Uniform Graphene Films on Copper Foils. *Science* 2009, **324**(5932): 1312-1314.
176. Peng ZW, Yan Z, Sun ZZ, Tour JM. Direct Growth of Bilayer Graphene on SiO₂ Substrates by Carbon Diffusion through Nickel. *ACS Nano* 2011, **5**(10): 8241-8247.
177. Bae S, Kim H, Lee Y, Xu XF, Park JS, Zheng Y, Balakrishnan J, Lei T, Kim HR, Song YI, Kim YJ, Kim KS, Ozyilmaz B, Ahn JH, Hong BH, Iijima S. Roll-to-roll production of 30-inch graphene films for transparent electrodes. *Nature Nanotechnology* 2010, **5**(8): 574-578.
178. Kim KS, Zhao Y, Jang H, Lee SY, Kim JM, Kim KS, Ahn JH, Kim P, Choi JY, Hong BH. Large-scale pattern growth of graphene films for stretchable transparent electrodes. *Nature* 2009, **457**(7230): 706-710.
179. Martin C. Driving change in the battery industry. *Nat Nano* 2014, **9**(5): 327-328.
180. Armand M, Tarascon JM. Building better batteries. *Nature* 2008, **451**(7179): 652-657.
181. Choi N-S, Chen Z, Freunberger SA, Ji X, Sun Y-K, Amine K, Yushin G, Nazar LF, Cho J, Bruce PG. Challenges Facing Lithium Batteries and Electrical Double-Layer Capacitors. *Angewandte Chemie International Edition* 2012, **51**(40): 9994-10024.
182. Zhang W-J. A review of the electrochemical performance of alloy anodes for lithium-ion batteries. *Journal of Power Sources* 2011, **196**(1): 13-24.
183. Chan CK, Peng H, Liu G, McIlwrath K, Zhang XF, Huggins RA, Cui Y. High-performance lithium battery anodes using silicon nanowires. *Nat Nano* 2008, **3**(1): 31-35.
184. Su X, Wu Q, Li J, Xiao X, Lott A, Lu W, Sheldon BW, Wu J. Silicon-Based Nanomaterials for Lithium-Ion Batteries: A Review. *Advanced Energy Materials* 2014, **4**(1): n/a-n/a.
185. Aurbach D. Review of selected electrode–solution interactions which determine the performance of Li and Li ion batteries. *Journal of Power Sources* 2000, **89**(2): 206-218.
186. Chan CK, Ruffo R, Hong SS, Cui Y. Surface chemistry and morphology of the solid electrolyte interphase on silicon nanowire lithium-ion battery anodes. *Journal of Power Sources* 2009, **189**(2): 1132-1140.

187. Szczech JR, Jin S. Nanostructured silicon for high capacity lithium battery anodes. *Energy & Environmental Science* 2011, **4**(1): 56-72.
188. Beaulieu LY, Eberman KW, Turner RL, Krause LJ, Dahn JR. Colossal Reversible Volume Changes in Lithium Alloys. *Electrochemical and Solid-State Letters* 2001, **4**(9): A137-A140.
189. Park C-M, Kim J-H, Kim H, Sohn H-J. Li-alloy based anode materials for Li secondary batteries. *Chemical Society Reviews* 2010, **39**(8): 3115-3141.
190. Simon G, Goswami T. Improving Anodes for Lithium Ion Batteries. *Metallurgical and Materials Transactions A* 2011, **42**(1): 231-238.
191. Liu N, Lu ZD, Zhao J, McDowell MT, Lee HW, Zhao WT, Cui Y. A pomegranate-inspired nanoscale design for large-volume-change lithium battery anodes. *Nature Nanotechnology* 2014, **9**(3): 187-192.
192. Ko M, Chae S, Jeong S, Oh P, Cho J. Elastic a-Silicon Nanoparticle Backboned Graphene Hybrid as a Self-Compacting Anode for High-Rate Lithium Ion Batteries. *ACS Nano* 2014, **8**(8): 8591-8599.
193. Liu N, Lu Z, Zhao J, McDowell MT, Lee H-W, Zhao W, Cui Y. A pomegranate-inspired nanoscale design for large-volume-change lithium battery anodes. *Nat Nano* 2014, **9**(3): 187-192.
194. Arbab S, Mirbaha H, Zeinolebadi A, Nourpanah P. Indicators for evaluation of progress in thermal stabilization reactions of polyacrylonitrile fibers. *Journal of Applied Polymer Science* 2014, **131**(11): n/a-n/a.
195. Korobeinyk AV, Whitby RLD, Mikhalovsky SV. High temperature oxidative resistance of polyacrylonitrile-methylmethacrylate copolymer powder converting to a carbonized monolith. *European Polymer Journal* 2012, **48**(1): 97-104.
196. Wang Y-X, Wang C-G, Wu J-W, Jing M. High-temperature DSC study of polyacrylonitrile precursors during their conversion to carbon fibers. *Journal of Applied Polymer Science* 2007, **106**(3): 1787-1792.
197. Wangxi Z, Jie L. Comparative study on preparing carbon fibers based on PAN precursors with different comonomers. *Journal of Wuhan University of Technology-Mater Sci Ed* 2006, **21**(1): 26-28.

198. Yang S, Zhi L, Tang K, Feng X, Maier J, Müllen K. Efficient Synthesis of Heteroatom (N or S)-Doped Graphene Based on Ultrathin Graphene Oxide-Porous Silica Sheets for Oxygen Reduction Reactions. *Advanced Functional Materials* 2012, **22**(17): 3634-3640.
199. Higgins D, Hoque MA, Seo MH, Wang R, Hassan F, Choi J-Y, Pritzker M, Yu A, Zhang J, Chen Z. Development and Simulation of Sulfur-doped Graphene Supported Platinum with Exemplary Stability and Activity Towards Oxygen Reduction. *Advanced Functional Materials* 2014, **24**(27): 4325-4336.
200. Higgins DC, Hoque MA, Hassan F, Choi J-Y, Kim B, Chen Z. Oxygen Reduction on Graphene–Carbon Nanotube Composites Doped Sequentially with Nitrogen and Sulfur. *ACS Catalysis* 2014, **4**(8): 2734-2740.
201. Yang Z, Yao Z, Li G, Fang G, Nie H, Liu Z, Zhou X, Chen Xa, Huang S. Sulfur-Doped Graphene as an Efficient Metal-free Cathode Catalyst for Oxygen Reduction. *ACS Nano* 2011, **6**(1): 205-211.
202. Tillman N, Ulman A, Elman JF. A novel self-assembling monolayer film containing a sulfone-substituted aromatic group. *Langmuir* 1990, **6**(9): 1512-1518.
203. Morgan WE, Van Wazer JR. Binding energy shifts in the x-ray photoelectron spectra of a series of related Group IVa compounds. *The Journal of Physical Chemistry* 1973, **77**(7): 964-969.
204. Choi CH, Park SH, Woo SI. Heteroatom doped carbons prepared by the pyrolysis of bio-derived amino acids as highly active catalysts for oxygen electro-reduction reactions. *Green Chemistry* 2011, **13**(2): 406-412.
205. Wohlgemuth S-A, Vilela F, Titirici M-M, Antonietti M. A one-pot hydrothermal synthesis of tunable dual heteroatom-doped carbon microspheres. *Green Chemistry* 2012, **14**(3): 741-749.
206. Paraknowitsch JP, Thomas A, Schmidt J. Microporous sulfur-doped carbon from thienyl-based polymer network precursors. *Chemical Communications* 2011, **47**(29): 8283-8285.
207. Lee SW, McDowell MT, Berla LA, Nix WD, Cui Y. Fracture of crystalline silicon nanopillars during electrochemical lithium insertion. *Proceedings of the National Academy of Sciences* 2012, **109**(11): 4080-4085.

208. Liu B, Soares P, Checkles C, Zhao Y, Yu G. Three-Dimensional Hierarchical Ternary Nanostructures for High-Performance Li-Ion Battery Anodes. *Nano Letters* 2013, **13**(7): 3414-3419.
209. Key B, Morcrette M, Tarascon J-M, Grey CP. Pair Distribution Function Analysis and Solid State NMR Studies of Silicon Electrodes for Lithium Ion Batteries: Understanding the (De)lithiation Mechanisms. *Journal of the American Chemical Society* 2010, **133**(3): 503-512.
210. Rochefort A, Salahub DR, Avouris P. The effect of structural distortions on the electronic structure of carbon nanotubes. *Chemical Physics Letters* 1998, **297**(1-2): 45-50.
211. Hoque MA, Hassan FM, Higgins D, Choi J-Y, Pritzker M, Knights S, Ye S, Chen Z. Multigrain Platinum Nanowires Consisting of Oriented Nanoparticles Anchored on Sulfur-Doped Graphene as a Highly Active and Durable Oxygen Reduction Electrocatalyst. *Advanced Materials* 2014, 10.1002/adma.201404426: n/a-n/a.
212. te Velde G, Baerends EJ. Precise density-functional method for periodic structures. *Physical Review B* 1991, **44**(15): 7888-7903.
213. Wiesenekker G, Baerends EJ. Quadratic integration over the three-dimensional Brillouin zone. *Journal of Physics: Condensed Matter* 1991, **3**(35): 6721.
214. Grimme S, Antony J, Ehrlich S, Krieg H. A consistent and accurate ab initio parametrization of density functional dispersion correction (DFT-D) for the 94 elements H-Pu. *The Journal of Chemical Physics* 2010, **132**(15): -.
215. Li Y, Chen Z. XH/ π (X = C, Si) Interactions in Graphene and Silicene: Weak in Strength, Strong in Tuning Band Structures. *The Journal of Physical Chemistry Letters* 2012, **4**(2): 269-275.
216. Arabi AA, Becke AD. Assessment of the PW86+PBE+XDM density functional on van der Waals complexes at non-equilibrium geometries. *The Journal of Chemical Physics* 2012, **137**(1): -.
217. Kim JG, Nam SH, Lee SH, Choi SM, Kim WB. SnO₂ Nanorod-Planted Graphite: An Effective Nanostructure Configuration for Reversible Lithium Ion Storage. *ACS Applied Materials & Interfaces* 2011, **3**(3): 828-835.

Appendix I Supporting Figures for Covalent Binding of Si to S-doped Graphene (Chapter 6)

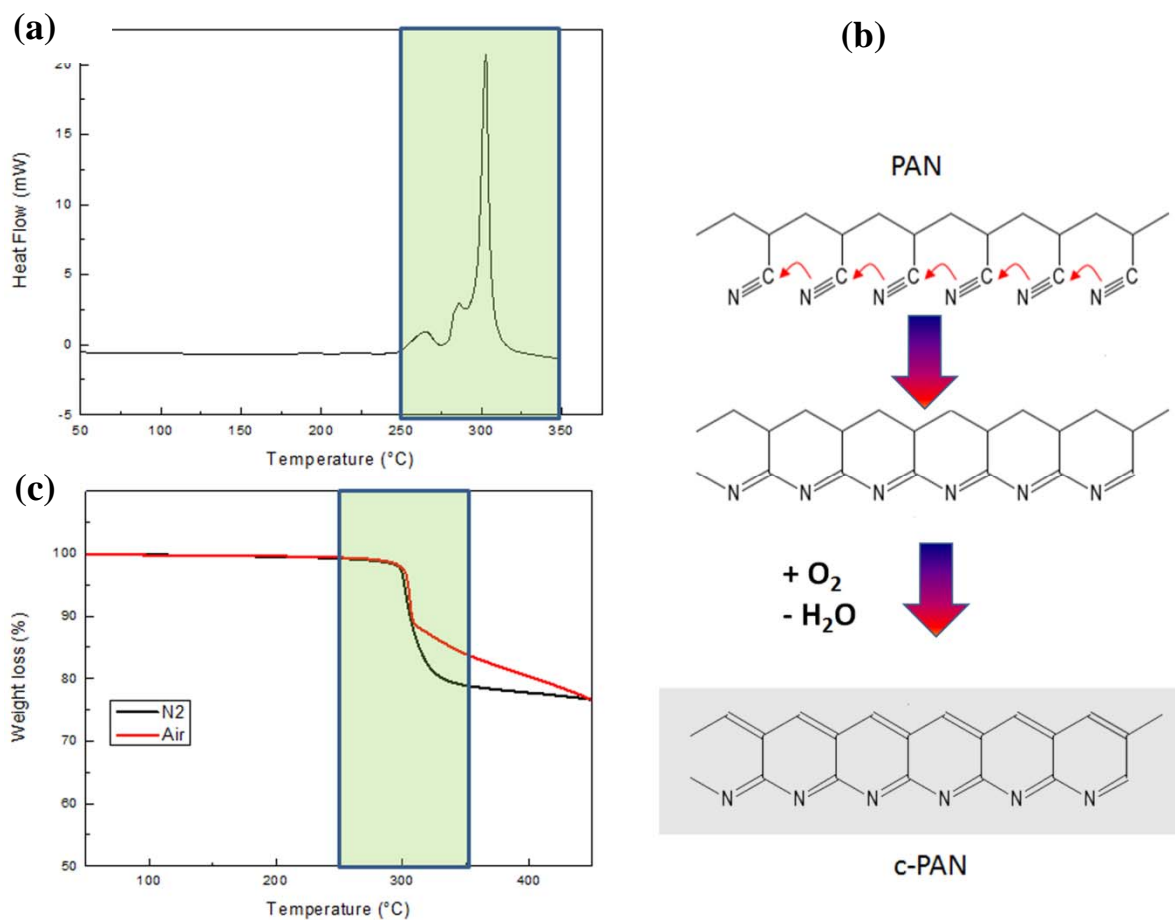


Figure S1. Differential scanning calorimetry (DSC) for polyacrylonitrile (PAN) in nitrogen showing a characteristic peak at $\sim 300^\circ\text{C}$, which corresponds to PAN cyclization as proposed in (b), c) thermogravimetric analysis for PAN in both air and in nitrogen. During cyclization in nitrogen there is more loss in mass which reveals it is more efficient than in air. By cyclization PAN loses $\sim 20\%$ of its mass.

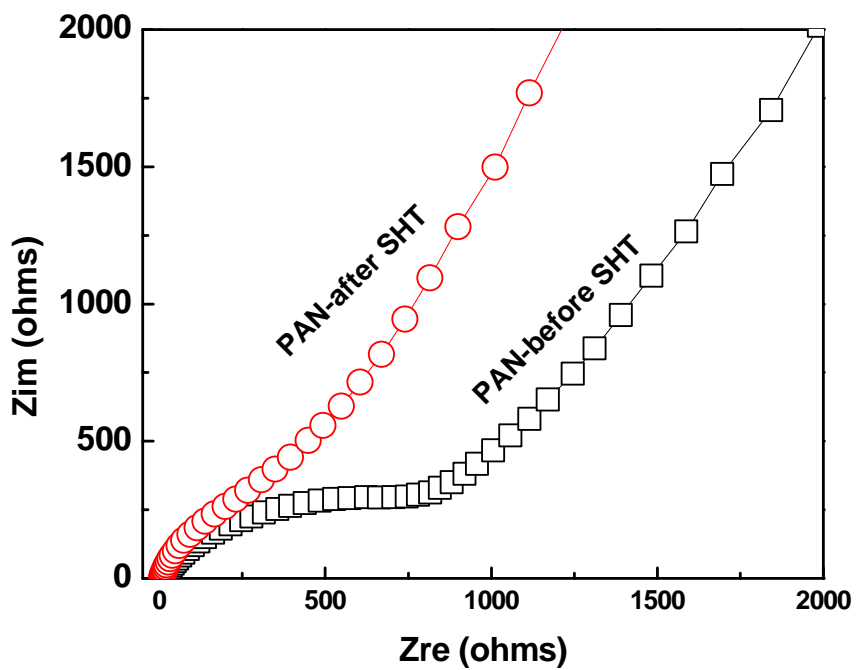


Figure S2. Electrochemical impedance for a coin cell fabricated using PAN-coated copper foil vs lithium, same method of cell testing as described in the experimental section. The figure reveals that both the electrode series resistance and the charge transfer resistance have been decreased after the sluggish heat treatment.

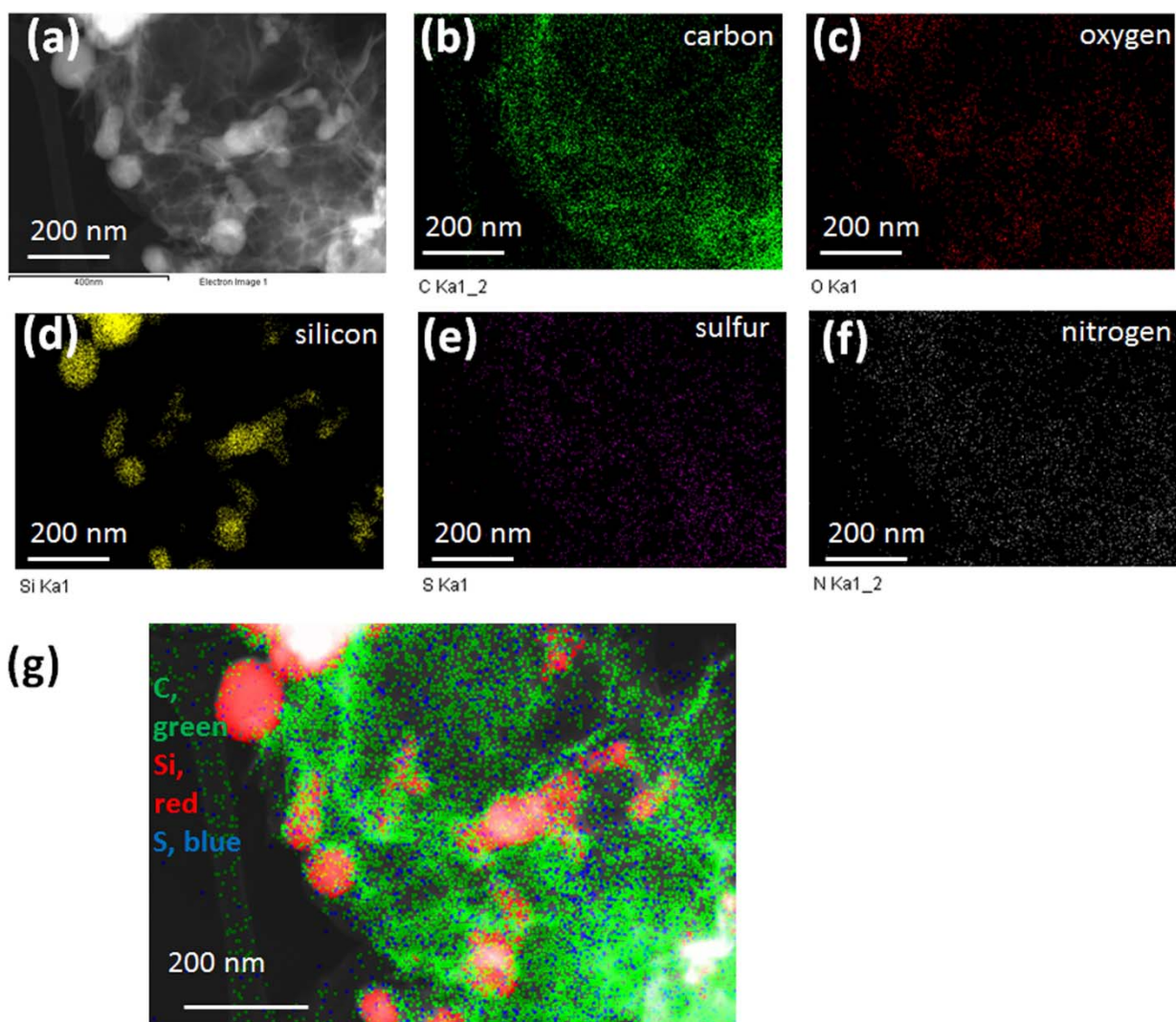


Figure S3. a) TEM image of SG-Si electrode material, b-f) the corresponding EDX mapping of the elements carbon, oxygen, silicon, sulfur, and nitrogen, respectively, and g) overlaid colour map of carbon (green), silicon (red), and sulfur (blue).

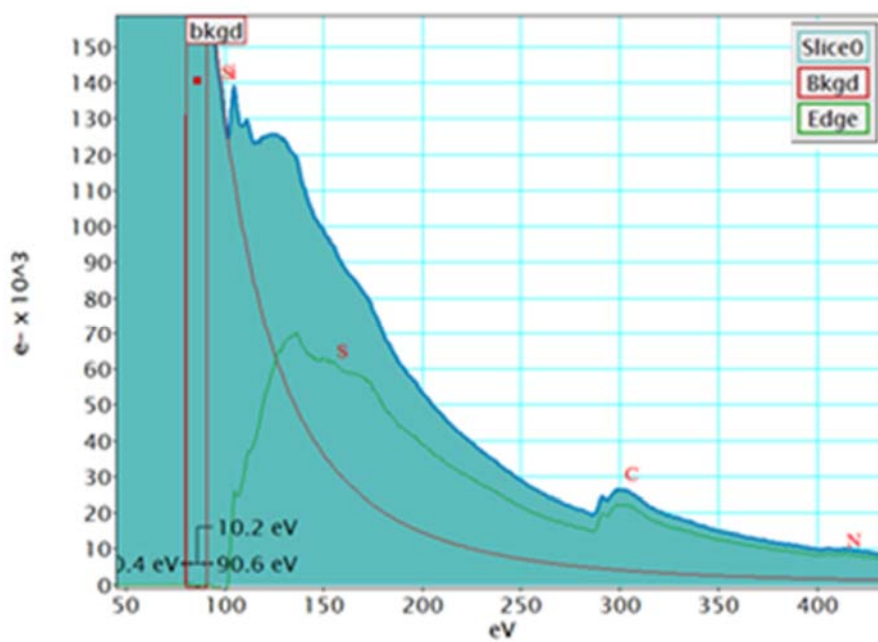


Figure S4. Electron energy loss spectrum for SG-Si electrode after sluggish heat treatment.

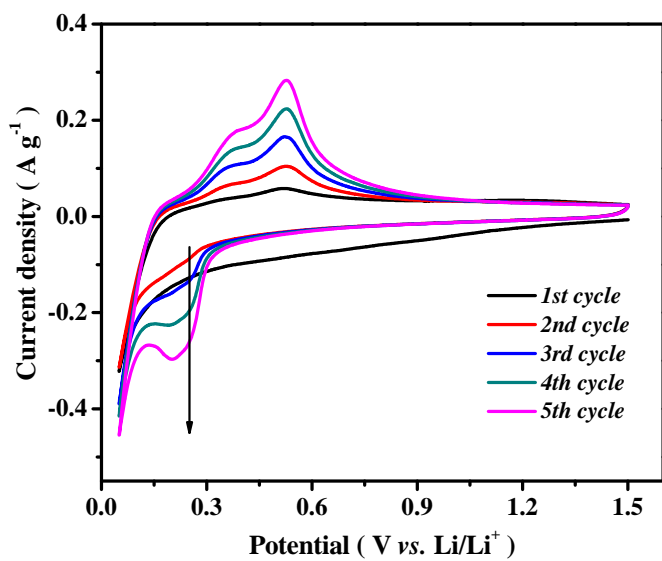


Figure S5. Cyclic voltammogram curves of G-Si anode material in coin cell.

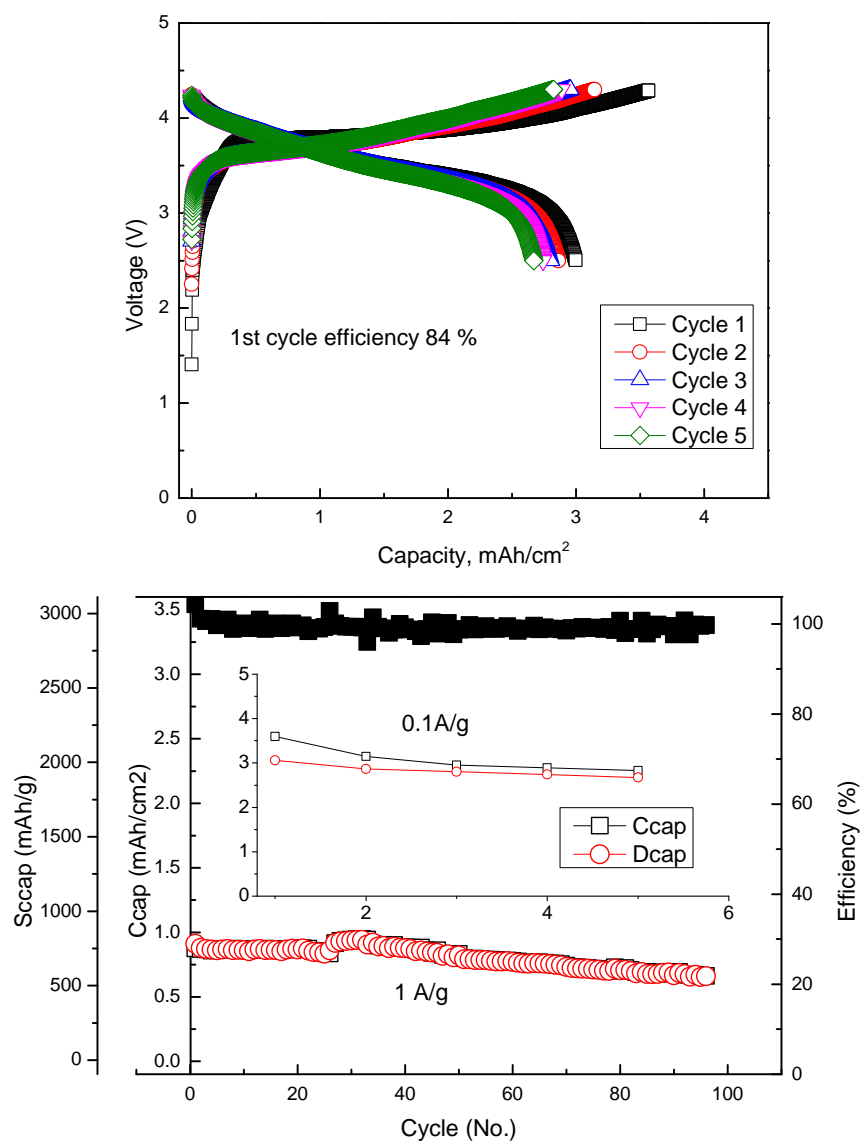


Figure S6. (top) Voltage profile for a full cell battery based on SG-Si anode and LiCoO₂ cathode, and (bottom), the corresponding cycle stability at 1 Ag⁻¹ with respect to SG-Si, the inset is the first 5 cycles at 0.1Ag⁻¹.

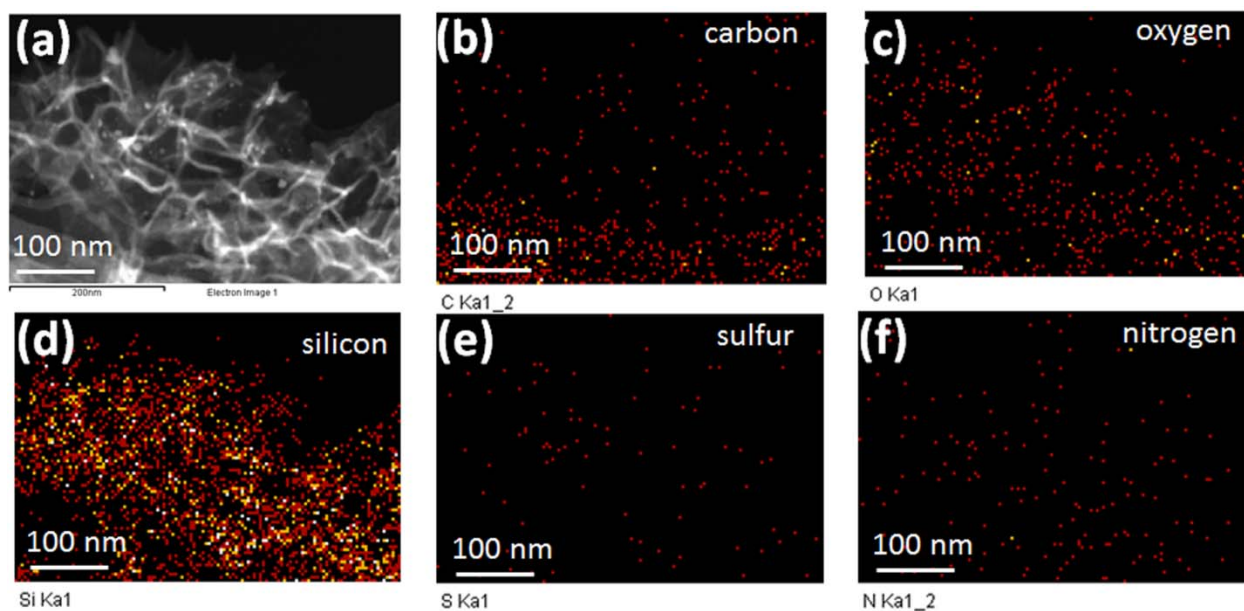


Figure S7. TEM image of SG-Si electrode material after being cycled for 2400 cycles of charge discharge, b-f) the corresponding EDX mapping of the elements carbon, oxygen, silicon, sulfur, and nitrogen, respectively.

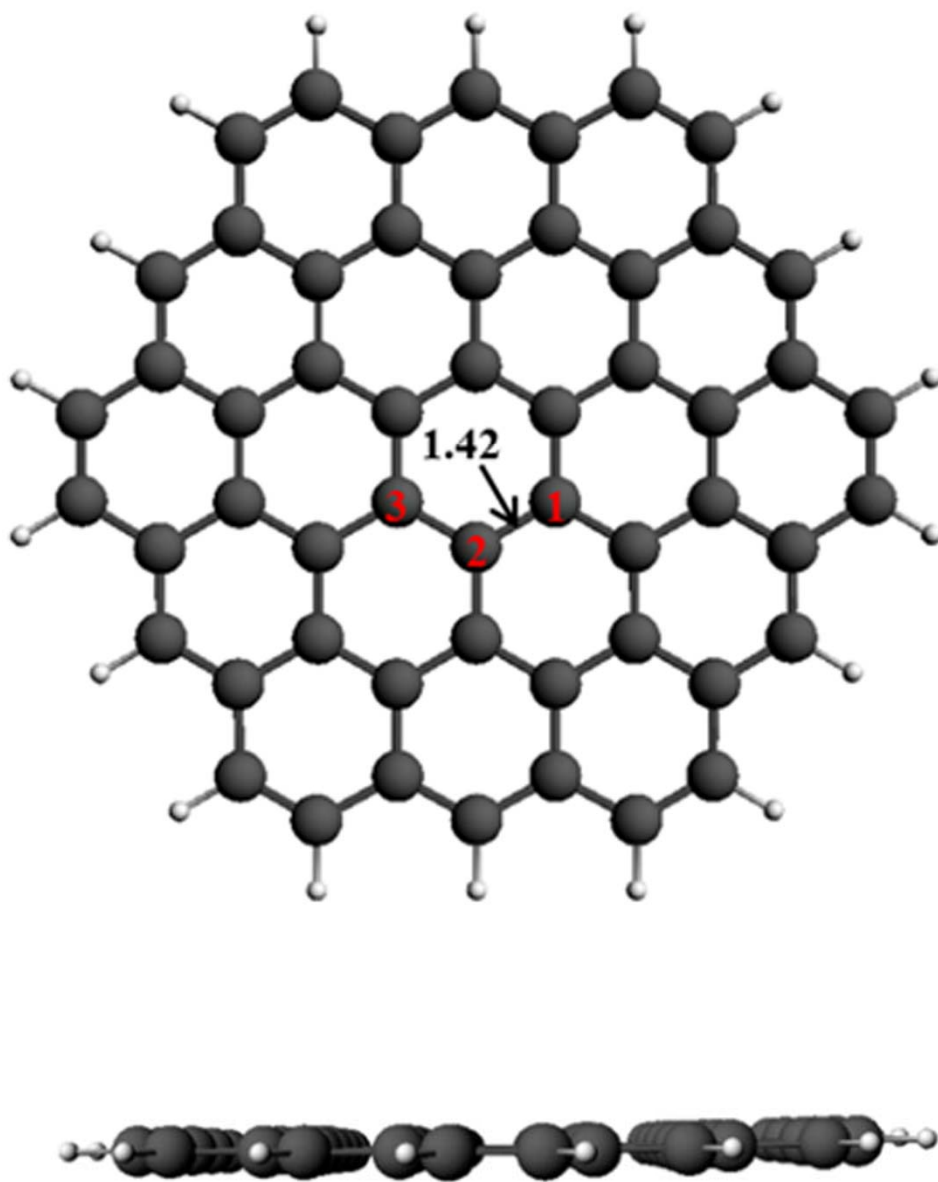


Figure S8. The optimized geometry of H passivated graphene (G): top view (top) and side view (bottom). C atoms are colored grey, H atoms white.

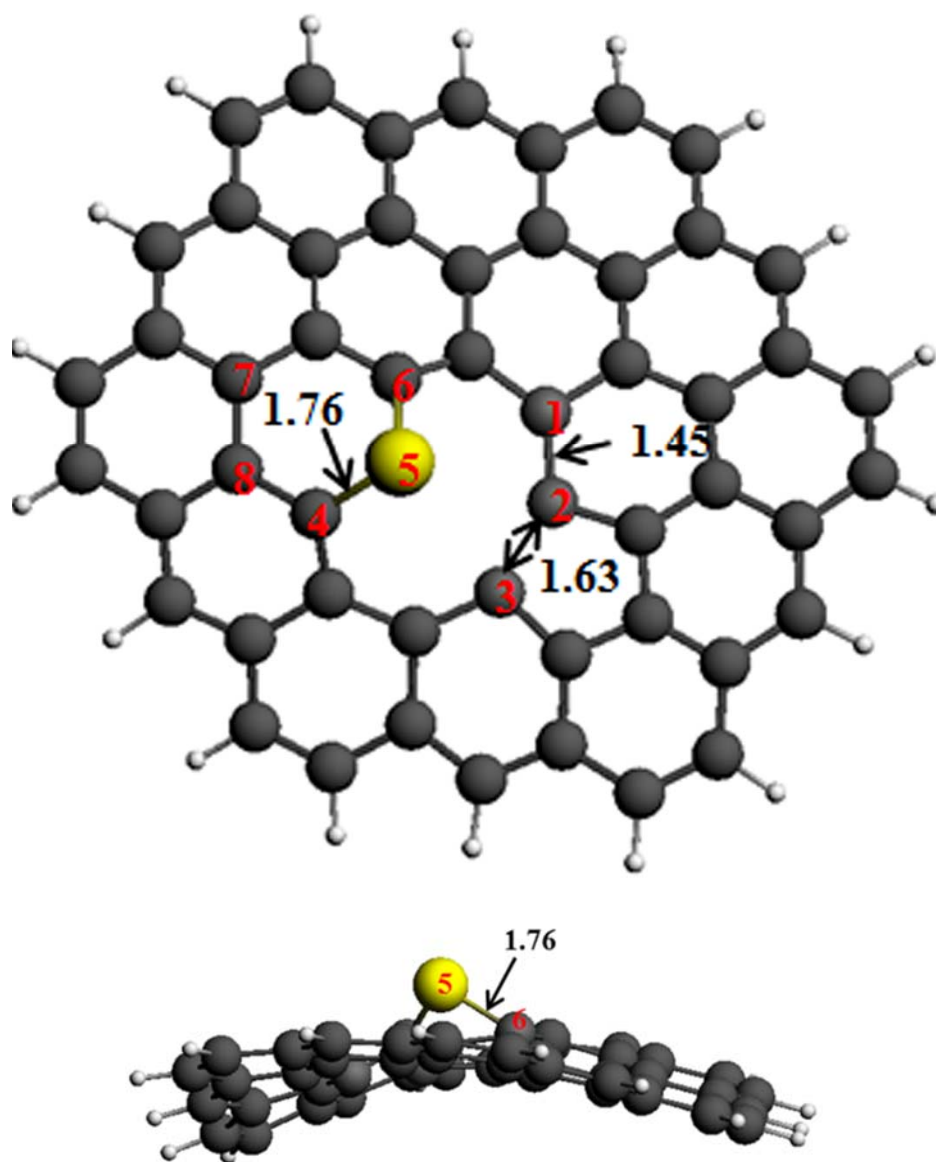


Figure S9. The optimized geometry of sulfur-doped graphene (S-G): top view (top) and side view (bottom). C atoms are colored grey, H atoms white, S atom yellow.

Table S1. Hirshfeld charges distribution before and after Si adsorption on the sulfur doped graphene (SG), atoms labeling are indicated in Figures S7 and S8.

Atoms	Si adsorption on G		Si adsorption on SG		
	G	G-Si	SG	SG-Si(A)	SG-Si(B)
C ₁	-0.001	-0.004	0.010	-0.006	-0.004
C ₂	-0.001	-0.028	0.003	-0.022	-0.113
C ₃	-0.001	-0.029	0.004	-0.013	-0.100
C ₄ (or Si ₄)		0.120	-0.016	-0.001	-0.019
S ₅			0.093	0.214	0.206
C ₆			-0.016	-0.035	-0.024
C ₇			-0.003	-0.070	-0.013
C ₈			-0.009	-0.028	-0.006
Si ₉				0.190	0.145

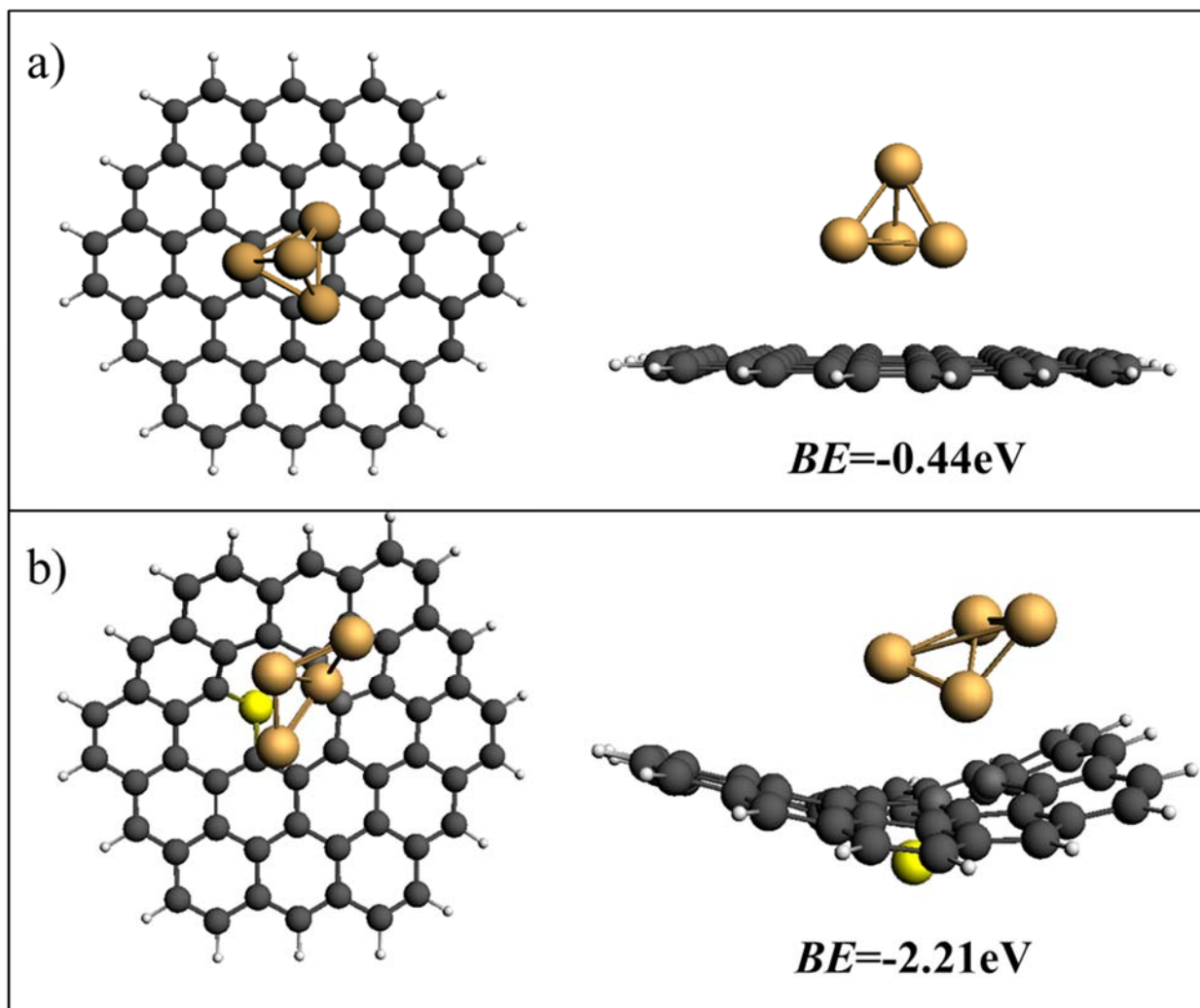


Figure S10. Geometries and bonding energy (BE) of the stable Si_4 cluster adsorption configurations on a): graphene; b): on sulfur doped graphene. C atoms are colored grey, H atoms white, S atom yellow, Si atom brown.

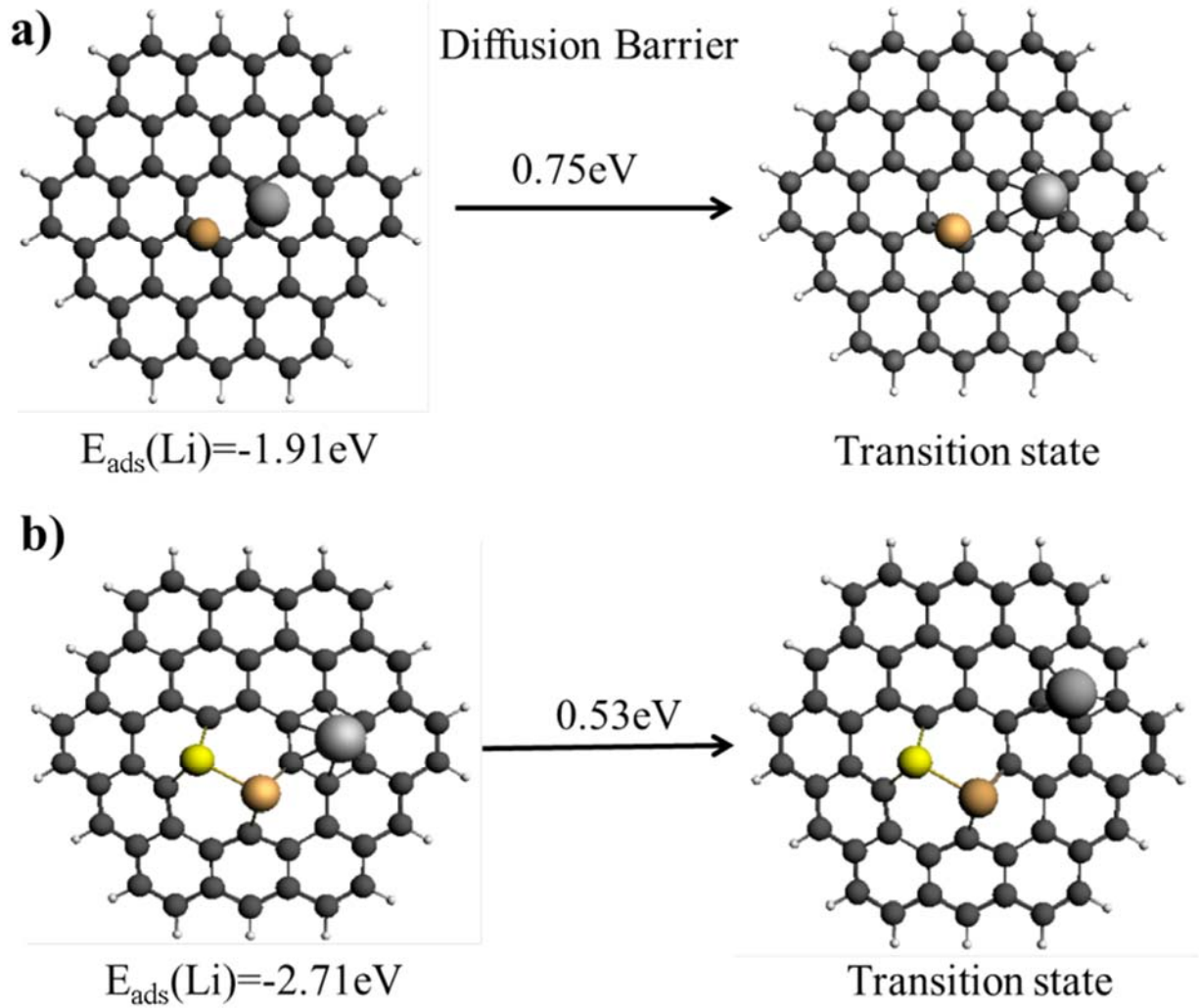


Figure S11. Li adsorption and transition state quantifying the diffusion barrier for a) G-Si and b) SG-Si

Appendix II Author's Contribution

This Appendix lists all of the author's contributions during his PhD study (2011-2014).

Submitted

1. Fathy M Hassan, et al . “Covalent synergy of silicon-sulfur-graphene as peculiar material design for cutting-edge lithium-ion battery”, to be submitted to *Nature Materials*. Manuscript #NM14123597 , Submitted on December 9, 2014.

Published

1. **F. M. Hassan**, A. R. Elsayed, V. Chabot, R. Batmaz, X.Xiao, Z. Chen Z. Subeutectic Growth of Single-Crystal Silicon Nanowires Grown on and Wrapped with Graphene Nanosheets: High-Performance Anode Material for Lithium-Ion Battery. *ACS Applied Materials & Interfaces* 2014, **6**(16): 13757-13764.
2. **F.M. Hassan**, V. Chabot, A.R. Elsayed, X. Xiao, Z. Chen, Engineered Si Electrode Nanoarchitecture: A Scalable Post-fabrication Treatment for the Production of Next-Generation Li-Ion Batteries, *Nano Letters*, **14** (2014) 277.
3. **F.M. Hassan**, Z.W. Chen, A.P. Yu, Z. Chen, X.C. Xiao, Sn/SnO₂ embedded in mesoporous carbon nanocomposites as negative electrode for lithium ion batteries, *Electrochim Acta*, **87** (2013) 844.
4. **F.M. Hassan**, V. Chabot, J.D. Li, B.K. Kim, L. Ricardez-Sandoval, A.P. Yu, Pyrrolic-structure enriched nitrogen doped graphene for highly efficient next generation supercapacitors, *J Mater Chem A*, **1** (2013) 2904.
5. Md Ariful Hoque, **Fathy M Hassan**, Drew Higgins, Ja-Yeon Choi, Mark Pritzker, Shanna Knights, Siyu Ye and Zhongwei Chen, “Multigrain platinum nanowires consisting of oriented nanoparticles anchored on sulfur-doped graphene as a highly active and durable oxygen reduction electrocatalyst”, *Advanced Materials*, online November 22, 2014, DOI: 10.1002/adma.201404426
6. D Higgins, MA Hoque, MH Seo, R Wang, **F Hassan**, JY Choi, M Pritzker, “Development and Simulation of Sulfur-doped Graphene Supported Platinum with Exemplary Stability and Activity Towards Oxygen Reduction”, *Advanced Functional Materials*, **24** (2014) 4325-4336.
7. M.A. Hoque, D.C. Higgins, **F.M. Hassan**, J.-Y. Choi, M.D. Pritzker, Z. Chen, Tin oxide - mesoporous carbon composites as platinum catalyst supports for ethanol oxidation and oxygen reduction, *Electrochim Acta*, **121** (2014) 421.
8. DC Higgins, MA Hoque, **F Hassan**, JY Choi, B Kim, Z Chen, Oxygen Reduction on Graphene–Carbon Nanotube Composites Doped Sequentially with Nitrogen and Sulfur, *ACS Catalysis* **4**, (2014) 2734-2740.

9. P Zamani, D Higgins, **F Hassan**, G Jiang, J Wu, S Abureden, Z Chen, Electrospun Iron–Polyaniline–Polyacrylonitrile Derived Nanofibers as Non–Precious Oxygen Reduction Reaction Catalysts for PEM Fuel Cell, *Electrochimica Acta*, **139**, (2014) 111-116
10. V. Chabot, K. Feng, H. W. Park, **F. M. Hassan**, A. R. Elsayed, A. Yu, X. Xiao, Z. Chen, “Graphene wrapped silicon nanocomposites for enhanced electrochemical performance in lithium ion batteries”, *Electrochim Acta*, **130** (2014)127 .
11. J.Y. Liao, X.C. Xiao, D. Higgins, D.G. Lee, **F. Hassan**, Z.W. Chen, Hierarchical Li₄Ti₅O₁₂-TiO₂ composite microsphere consisting of nanocrystals for high power Li-ion batteries, *Electrochim Acta*, **108** (2013) 104.
12. R. Wang, D.C. Higgins, M.A. Hoque, D. Lee, **F. Hassan**, Z. Chen, Controlled Growth of Platinum Nanowire Arrays on Sulfur Doped Graphene as High Performance Electrocatalyst, *Nature Sci. Rep.*, **3** (2013) 2431
13. V Chabot, **F.M. Hassan**, A. Yu, Nitrogen Doped Graphene as a High Efficient Electrode for Next Generation Supercapacitors, *ECS Transactions*, 50 (2013).
14. A. Davies, P. Audette, B. Farrow, **F. Hassan**, Z. W. Chen, J. Y. Choi, A. P. Yu, Graphene-Based Flexible Supercapacitors: Pulse-Electropolymerization of Polypyrrole on Free-Standing Graphene Films, *J Phys Chem C*, 115 (2011) 17612.

Patents

1. Z. Chen, **F.M. Hassan**, A. Yu, US provisional patent “Low cost synthesis of single material bifunctional nonprecious catalyst for electrochemical devices” filed on July 30/12, USPTO #: 61/741,869. International WO Patent WO2014019089 A1
2. Z. Chen, **F. M. Hassan**, US provisional patent “A simple low cost treatment technology for high capacity silicon based lithium ion battery”, filed on July 30, 2012 , USPTO, #:61/741,868.
3. Z. Chen, A. Yu, M. A. Hoque, **F. M. Hassan** , US provisional patent “Advanced graphene supports for platinum or platinum alloy nanowire catalysts and electrodes for high performance and durable fuel cell”, filed on June xx, 2014 , USPTO, US Patent App. 61/997,817.
4. **F. M. Hassan**, Z. Chen, Xingcheng Xiao, US provisional patent “A process of making nano-hybrid sulfur-doped graphene/silicon composites and using as electrodes for lithium batteries”, filed on October, 2014 by General Motors, US , P030743.

Coauthoring Book Chapters

1. Z. Chen, **F.M. Hassan**, A. Yu, Electrochemical Engineering Fundamentals, in: Electrochemical Technologies for Energy Storage and Conversion, Wiley-VCH Verlag GmbH

& Co. KGaA, 2011, pp. 45-68.

2. **Fathy M. Hassan**, Aiping Yu, Applications of Electrochemical Supercapacitors, in: Electrochemical Supercapacitors for Energy Storage and Delivery, Fundamentals and Applications, CRC Press, Taylor & Francis Group, 2011, pp. 317-348.

Conferences presentations

1. **F. M. Hassan**, Z. Chen, X. Xiao, "A scalable treatment improving interfacial structure of Si electrode; An advance to boost the performance of Li ion batteries", 64th Canadian Chemical Engineering Conference, Niagara Falls, ON, October 19-22, 2014. (Oral)
2. **F. M. Hassan**, X. Xiao, Z. Chen, "Engineered Si nano-architected electrodes for Li-ion batteries" Gordon conference, Batteries; Advances in Characterization, Analysis, Theory and Modeling of Basic Processes, March 9-14, 2014, Ventura, CA, USA. (Poster).
3. **F. M. Hassan**, Z. Chen, A. Davies, J-Y Choi, A. Yu. Pulse-Electropolymerization of Polypyrrole on Free-Standing Graphene Films for Efficient Flexible Supercapacitors, 222nd ECS Meeting Conference PRiME, October 7-12, 2012, Honolulu, Hawaii.
4. **F. M. Hassan**, A. Yu, H. W. Park, Z. Chen, X. Xiao, Z. Chen, High Capacity Li-Ion Batteries Based on Hetero- Nanostructured SnO₂-Sn/CMK-3 Materials. 222nd ECS Meeting Conference PRiME, October 7-12, 2012, Honolulu, Hawaii.